

博士論文

**Thermal conductance of thin films composed of
hetero nanotubes based on single-walled CNT**

(単層 CNT を元にしたヘテロナノチューブ薄膜の熱コンダクタンス)

王 彭穎愷

(WANG PENGYINGKAI)

Doctoral Dissertation

**Thermal conductance of thin films composed of
hetero nanotubes based on single-walled CNT**

by

Pengyingkai WANG

Presented to

GRADUATE SCHOOL OF ENGINEERING, THE UNIVERSITY OF TOKYO

in Partial Fulfillment of the Requirements for the Degree of

Doctoral of Philosophy

in the Field of Mechanical Engineering

©2020

ABSTRACT

Carbon nanotube has (CNT) been one of the centers of nanomaterials since discovered by Iijima. Due to the attractive mechanics, optics, electronics and thermotic properties, carbon nanotube and assembles have been extensively investigated for the massive potential applications. Inherited from graphene, carbon nanotube possesses significant thermal conductivity along the axial direction, thus its probable prospects for thermal interface material has drawn the attention of researchers and engineers. Besides, the possibility of synthesizing high-quality carbon nanotube and tailoring technique — designed structure, chemically doping, etc. — lead the development in carbon nanotube related researches one step further.

Carbon nanotube can be tailored in structure, forming films, mats, array with required length, thickness, and volume fraction. However, the limitation of carbon nanotube assemble application is obvious: in all carbon nanotube assemble, they tend to aggregate or forming bundles because of the van der Waals interaction. This contact is believed to suppress the high thermal conductivity individual carbon nanotube process, while the electrical properties has not been affected. Beside direct use, carbon nanotube could be filled into other materials like epoxy to as filling material to alter the thermal property. Yet to avoid aggregation, proper surface functionalization should be applied and which cause change to the perfect structure of carbon nanotube. Neither of the ways can take the full advantage of carbon nanotube.

Therefore, this thesis attempts to uncover the structure dependent thermal conductivity of carbon nanotube and propose a possible way to tailor carbon nanotube-based materials.

To study the structural dependent thermal transport property of carbon nanotube, a micro thermometer compatible with transmission electron microscope (TEM) has been fabricated. High quality single-walled carbon nanotube (SWCNT) can be transferred to micro thermometer with the detailed structure identified by scanning electron microscope (SEM) and TEM. The thermal conductivity of three carbon nanotube bundles with different sizes have been studied. The contact resistance between carbon nanotube and micro thermometer are ignored because of the large contact area. Geometry of the bundle samples are determined by SEM observation and calculation. The effective thermal conductivity of the three samples show a

typical temperature dependent, that is increase with temperature and reach maximum at around room temperature. By plotting the thermal conductivity against bundle size, the structure dependent has been clearly observed. Compared with isolated carbon nanotube, thermal conductivity of bundle decreases with the bundle size increases. The decrease rate is changing from slow to fast and become slow again. For small bundle size like two, thermal conductivity is quite high and comparable to that of isolated carbon nanotube. However, the larger the size of the bundles, the lower its effective thermal conductivity. The quantitative study that thermal conductivity decrease logarithmically with the bundle size is further expanded with consideration of the newly added three samples. The intertube interaction is experimentally proved to degenerate thermal conductivity of carbon nanotube.

Van der Waals heterostructure (vdWH) is attracting vase attention recently. Without lattice matching and chemical bond, heterostructure has made it possible to combine different material together. Therefore, the relative researches started from 2-dimensional (2D) nanomaterials and quickly spread to 1-dimentional (1D) and even integrated dimensional materials. Compared with the systematic study on 2D vdWH, 1D vdWH is barely studied up to now. Owing to the development in 1D vdWH synthesis, high quality 1D heterostructure based on SWCNT can be synthesized by normal chemical vapor deposition (CVD) method.

In this these, 1D hetero nanotube based film will be synthesized by CVD method and the thermal property will be investigated with a contact-free steady-state infrared (IR) thermography method. The templates used are SWCNT films prepared by the aerosol CVD synthesis method with variable transparency from 52 % to 92 %. With the SWCNT films as a template, the heterostructured films were prepared by CVD, which can produce conformal and highly-crystalline BNNTs. Then, a contact-free steady-state infrared (IR) thermography measurement was used to investigate the in-plane sheet thermal conductance of the as-synthesized SWCNT-BNNT films. The results indicate the sheet thermal conductance of SWCNT-BNNT heterostructure films are 18524.1140 ± 2718.7684 nW/K, 14713.5110 ± 1588.2233 nW/K, 9146.2500 ± 1265.3946 nW/K, 6410.2564 ± 1964.9838 nW/K, 5892.3395 ± 1727.4211 nW/K at room temperature synthesized on SWCNT film with transparency of 53%,

62%, 72%, 87% and 92%, respectively. Compared with annealed SWCNT film of the same transparency, the increase are 23%, 44%, 53%, 80% respectively. Besides the thermal property, electrical, mechanical and thermoelectrical properties have been discussed together. A concise model is put forward to explain the thermal transport mechanism in the hetero film. The findings in previous structural dependent thermal conductivity also shed some light on the discussion of phonon transport in heterostructure film. From the experiment result, the heterostructure film shows better mechanical strength originated from BNNT and satisfying electrical conductance inherited from SWCNT.

In nano-scale, micro thermometer is fabricated and the structure dependent thermal conductivity of SWCNT is investigated; in macro-scale, a quick and handy method is presented here to measure the sheet thermal conductance of 1D heterostructure nanotube based thin films. Therefore, the clear relationship of the thermal conductivity of carbon nanotube and its nanoscale structure can help to design the thermal conductance of carbon nanotube thin films. This study also fills the gap in the study of 1D vdW heterostructure material up to now and may cast new light on following works in tailoring vdW heterostructure with new properties. Quantitative analytical model have been proposed for both SWCNT bundle and SWCNT network. The models reveals the transport mechanism and are extendable to other materials with similar structure.

CONTENTS

ABSTRACT	I
CHAPTER 1	INTRODUCTION7
1.1	BACKGROUND8
1.2	PHYSICS OF CARBON NANOTUBES 11
1.2.1	geometrical structure 11
1.2.2	electrical property..... 14
1.2.3	phonon modes 17
1.3	THERMAL TRANSPORT IN CARBON NANOTUBE 18
1.3.1	thermal transport in carbon nanotubes and assembles 18
1.3.2	thermal conduction methodology of carbon nanotubes..... 19
1.4	VAN DER WAALS HETEROSTRUCTURE20
1.4.1	synthesis of van der waals heterostructure21
1.4.2	properties of van der waals heterostructure24
1.4.3	application of van der waals heterostructure.....28
CHAPTER 2	MOTIVATION, CHALLENGES AND ORGANIZATION OF THE THESIS.....32
2.1	MOTIVATION AND CHALLENGES.....33
2.2	ORGANIZATION OF THE THESIS.....34
CHAPTER 3	STRUCTURAL THERMAL TRANSPORT PROPERTY OF CARBON NANOTUBE
BUNDLES	37
3.1	BACKGROUND38
3.2	SAMPLE PREPARATION39
3.2.1	Micro Thermometer device fabrication.....40
3.2.2	horizontally SWCNT sample by CVD method41
3.2.3	Sample Characterization43

3.3	MEASUREMENT SETUP	44
3.3.1	Thermal Conductance Measurement	45
3.3.2	Uncertainty Analysis	46
3.3.3	Noise and Sensitivity.....	48
3.4	EXPERIMENTAL RESULTS AND DISCUSSIONS.....	51
3.4.1	Thermal Conductance of Suspended Beam	51
3.4.2	Sample Identification	52
3.4.3	Thermal Conductance of SWNTs	54
3.4.4	Effective Thermal Conductivity	55
3.4.5	Quantitative Study of Structural Dependent Thermal Conductivity of SWCNT Bundles.....	56
3.5	CONCLUSION	64
CHAPTER 4 MEASUREMENT OF SHEET THERMAL CONDUCTANCE OF THIN FILMS COMPOSED OF COAXIALLY COMBINED SINGLE-WALLED CARBON NANOTUBE AND BORON NITRIDE NANOTUBES.....		
		67
4.1	BACKGROUND	68
4.2	SAMPLE PREPARASION	70
4.2.1	One dimensional heterostructure synthesized by CVD	70
4.2.2	Characterization of samples	73
4.3	EXPERIMENT DESIGN.....	76
4.3.1	Experimental Setup	76
4.3.2	Temperature measurement.....	78
4.3.3	Uncertainty Analysis	79
4.3.4	Noises and Sensitivity	81
4.4	EXPERIMENTAL RESULTS AND DISCUSSIONS	82
4.4.1	Sheet Thermal Conductance of annealed SWCNT film	82
4.4.2	Sheet Thermal Conductance of SWCNT-BNNT film.....	84
4.4.3	Thermal transport model of SWCNT-BNNT film.....	86

4.4.4	Electrical conductance of SWCNT-BNNT film	89
4.4.5	Seebeck coefficient of SWCNT-BNNT film	90
4.5	MODELING STUDY OF FILM THERMAL PROPERTY	91
4.5.1	Random stick network of SWCNT film	92
4.5.2	Key parameters analysis	94
4.5.3	quantitative study of diameter and length dependent thermal conductivity of SWCNT film.....	95
4.5.4	Quantitative analysis of thermal transport property of film.....	100
4.6	CONCLUSIONS	106
CHAPTER 5	SUMMARY	109
REFERENCE	112
LIST OF FIGURES	122
LIST OF TABLES	128
NOMENCLATURE	129
PUBLICATION LIST	130
ACKNOWLEDGEMENTS	131
CURRICULUM VITAE	132

CHAPTER 1 INTRODUCTION

1.1 BACKGROUND

As one of the representatives of nanomaterials, carbon nanotubes (CNTs) have excellent mechanical, electrical, thermal, optical and reactive properties due to their unique one-dimensional structure, which has shown numerous application potential in energy storage and conversion, composite materials, heterogeneous catalysis, environmental protection, biomedicine and other fields. The history can be originated in 1879, Thomas A. Edison used it as a filament in electric heating bulbs. However due to the synthesis method, the quality of CNT remained a problem. The real breakthrough in the research of carbon nanotubes comes from the clear identification of the unique one-dimensional tubular structure of carbon nanotubes by Professor Iijima triggered giant upsurge in academic research on this sp^2 covalently bonded CNTs with high chemical stability [1]. After that, in 1993, he synthesized single-shell carbon nanotubes with a diameter of 1 nm[2]. Although graphene discovered in 2004 diverted a part of research attention from CNTs, it's still the most well-researched and widely-concerned innovative nanomaterials. Moreover, the research focus has transited from initial structural characterization to subsequent performance and application research.

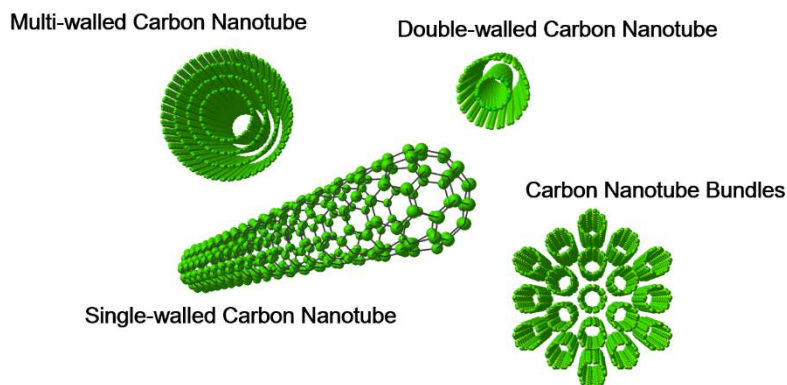


FIG. 1-1 Carbon nanotube related 1 D carbon materials that have been extensively studied during the recent years.

As shown in Figure 1-1, carbon nanotubes have a variety of morphological structures. Single-walled carbon nanotubes are a cylindrical tubular structure formed by curling a single layer of graphene; double or multi-walled carbon nanotubes are coaxial with multiple single-walled carbon nanotubes, forming a one-dimensional tubular structure like a tree trunk. Due to

the Sp^2 hybridization between different carbon atoms, the Young's modulus of carbon nanotubes is as high as 1.2 TPa, the rate of elongation at break is approximately 17%, and the fracture strength is 100 times higher than that of steel. The structure index (n, m) of the nanotube curl determines the diameter and chirality, which is directly related to the metallicity, semiconductor or small band gap semiconductor electron transport behavior. CNTs also have adjustable chemical surfaces, hollow internal chambers, and excellent biocompatibility. These novel properties brought up many practical applications, such as electrical conductivity, electromagnetic, microwave absorption, and high-strength composite materials; supercapacitors or battery electrodes; catalysts and carriers; field emission displays; transparent conductive films; scanning probes; drug delivery systems; electronics devices; sensors and actuators, and so on[3].

In the field of microelectronics, the development of microelectronics technology has made devices smaller and faster, and materials with excellent electrical and thermal properties are ideal choices. Among the many candidate materials, carbon nanotubes are a kind of material with bright prospective. With the features of stable, flexibility and harmless, CNT films are one of the potential candidates for solar cells [4]. Besides, the outstanding thermal properties of CNTs is also worthy of considering. Savas et al. revealed that at room temperature, an isolated (10, 10) carbon nanotube has a very high thermal conductivity, about $6600 \text{ Wm}^{-1}\text{K}^{-1}$ [5].

In the past few decades, predecessors have conducted extensive research on the heat transfer characteristics of CNTs through various theory and experimental methods. The results are summarized in Table 1-1[6-19]. However, due to different sample preparation methods in experiment and different potential function adopted in simulation, it is difficult to directly compare the results to make a correct conclusion. The main difficulty is determining the precise structure of SWCNTs. It can be seen in Table 1-1, according to the experiments, the thermal conductivity of CNTs ranges from tens to thousands, and the similar phenomena is also appeared in related simulation results. Even in the research works from the same group researchers, there is also a big difference in comparing the heat transfer capabilities of different samples. In addition, when 1D individual SWNTs form a more complicated multi-dimensional bundles or bulky mats or thin films, the thermal transport characteristics will change greatly, and even become good

insulators [20]. Above mentioned indicate that the structure of CNT has a great influence on the thermal transport properties, especially the change of dimension or structure morphology. Although a great deal of developments has been achieved for the individual CNTs (SWCNTs or MWCNTs), however it is not suitable for further commercialization due to the difficulty in placing individual CNTs in the designated location and the properties of CNTs are deeply depend on the structure. Compare with the individual CNTs, the CNT-based thin films and the derived composites may provide more opportunities to realize commercialization due to the extraordinary characteristic properties, along with the easy manufacture by traditional photolithography or printing technologies [21]. However, the intrinsic thermal transport properties and mechanisms of CNT-based films is rare and ignored, which needs further investigation.

Table 1-1 Reported thermal conductivities for SWNTs, MWNTs and CNT films or mats by experiments.

SWNTs			MWNTs			Films	
L (μm)	D (nm)	κ (Wm ⁻¹ K ⁻¹)	L (μm)	D (nm)	κ (Wm ⁻¹ K ⁻¹)	volume fraction	κ (Wm ⁻¹ K ⁻¹)
2	2	5000 [6]	2.5	14	3126 [9]	0.45	72.8 [12]
1.9	0.509	3787 [7]	3.7	9.89	2069 [10]	0.03	80 [13]
2.03/4.31	1.5/2.34	635/450 [8]	32	8.2	1400 [11]		
SWCNT bundle			MWCNT bundle			mat	
L (μm)	D (nm)	κ (Wm ⁻¹ K ⁻¹)	L (μm)	D (nm)	κ (Wm ⁻¹ K ⁻¹)	volume fraction	κ (Wm ⁻¹ K ⁻¹)
2.66/4.2	148/10	3.8/166 [14]	1200- 1800	5/11/24/273	610.6/420.3/3 08.6/302.4/	0.58	216.2 [17]
31/76.3/89	9.89/12.54/1 2.9	16/163/66 [15]		8/47/	246.5/211.3/2 07.2/161.7/13	0.68	10/60 [18]
2.5/4/5	8/5/13	150/1500/400 [6]		5/127/130	2.7/126.5/120. 3/ 114.1 [16]	0.5	43 [19]

In the following part of this Chapter, the physics of CNT will be introduced, including its structure, its electrical property which also pitch in heat transfer and its phonon modes, which is the main heat carriers. Then the thermal transport mechanism in CNT will be discussed. Lastly, the new possibility for CNT materials will be presented.

1.2 PHYSICS OF CABON NANOTUBES

1.2.1 GEOMETRICAL STRUCTURE

To understand the structure of CNTs, it is easy to think of rolling a piece of graphene into a seamless cylinder and adding two terminations to the ends. The terminations are fullerene hemisphere, which is very suitable for long cylindrical nanotubes. The method of rolling CNTs is characterized by a rolling vector or a chiral vector Ch , which divides the CNTs into three groups: zigzag, armchair, and chiral. As shown in Figure 1-2 [22]. The name of the structure comes from the shape of the cross-sectional ring, as shown by the edges of the carbon nanotubes in the figure. Zigzags and armchairs are symmetrical structures, chiral nanotubes are common and abundant, lacking this function.

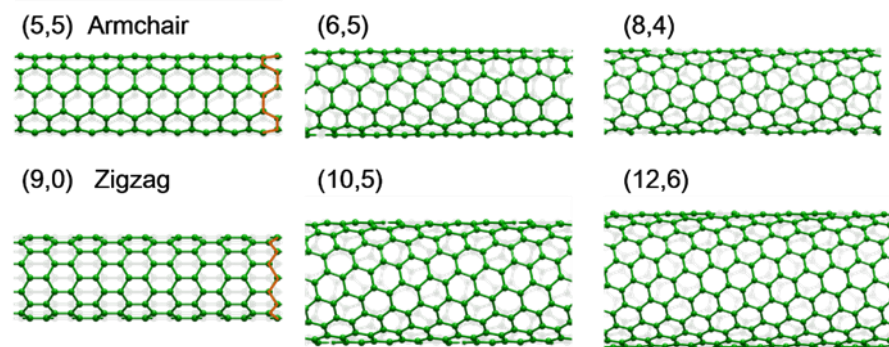


FIG. 1-2 Carbon nanotubes with different chirality. (5, 5) is featured by the red line shown at end of the tube.

(9, 0) is named by the zigzag structure at the tube end shown by read line. Other four chiral structures are popular carbon nanotube and being widely studied.

Chiral vector is the only one parameter to define a carbon nanotube, shown as vector OA in Figure 1-3, representing lattice structure. The distance between two carbon atoms is $a_0 =$

1.42 Å. OB is perpendicular to OA, which is the direction of the axial called translational vector T. Moving OB along OA until point O and point A coincide, define the position of B as B'. If we cut OABB' and roll it up to make O and A coincide and B and B' coincide, CNTs will be formed. Set unit vectors of the lattice to a_1 and a_2 , as shown in Figure 1-3. Then the a_1 and a_2 can be used to express C_h :

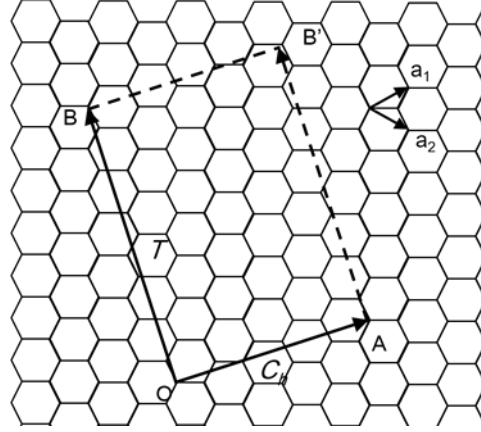


FIG. 1-3 Lattice structure of graphene. OA, OB denotes chiral vector and translational vector respectively.

$$C_h = na_1 + ma_2 \equiv (n, m), \quad (n, m \in \text{integer}, 0 \leq |m| \leq n) \quad (1-1)$$

$$a_1 = \left(\frac{\sqrt{3}}{2} a, \frac{1}{2} a\right), a_2 = \left(\frac{\sqrt{3}}{2} a, -\frac{1}{2} a\right) \quad (1-2)$$

It has been proved that many properties can be predicted from the chiral vector (n, m) . In the case of zigzag structure CNT, $m = 0$, or $C_h = (n, 0)$. As for armchair structure, $m = n$, and all other vectors correspond to chiral structure carbon nanotube. Diameter of the carbon nanotube d , is calculated through C_h :

$$d_t = \frac{L}{\pi}, L = |C_h| = \sqrt{C_h \cdot C_h} = a\sqrt{n^2 + m^2 + mn} \quad (1-3)$$

where a is the lattice constant, $|a| = |a_1| = |a_2| = a_0 \cdot \sqrt{3} = 1.42 \times \sqrt{3} = 2.46 \text{ \AA}$. For instance, chiral vector of OA is $(4, 1)$ in Figure 1-3, the corresponding diameter is $d_t = 3.59 \text{ \AA}$.

The chiral angle θ is defined as the cross angle of C_h and a_1 , defines the spiral symmetry of nanotube. Considering hexagonal symmetry of honeycomb lattice, the absolute value range of θ can be $0 \leq |\theta| \leq 30^\circ$. And it can be obtained through the following equation:

$$\theta = \arccos\left(\frac{C_h \cdot a_1}{|C_h| \cdot |a_1|}\right) = \arccos\left(\frac{2n+m}{2\sqrt{n^2+m^2+nm}}\right) \quad (1-4)$$

More specifically, several typical values are for different structure, $\theta = 0^\circ$ for the zigzag structure and $\theta = 30^\circ$ for armchair. Furthermore, the deduced chirality and nanotube diameter affect thermal property significantly.

The vector OB in Figure 1-3 is perpendicular to the chiral vector C_h and is defined as the translation vector. Translation vectors can be expressed by unit vectors a_1 and a_2 :

$$T = t_1 a_1 + t_2 a_2 \equiv (t_1, t_2), \quad (t_1, t_2 \in \text{integer}) \quad (1-5)$$

where

$$t_1 = \frac{2m+n}{d_R}, \quad t_2 = -\frac{2n+m}{d_R} \quad (1-6)$$

d_R is the greatest common divisor of $(2m+n)$ and $(2n+m)$. If we define d as the largest common divisor of n and m ,

$$d_R = \begin{cases} d & \text{if } n-m \text{ is not a multiple of } 3 \\ 3d & \text{if } n-m \text{ is a multiple of } 3 \end{cases} \quad (1-7)$$

Therefore, the definition of different structure of carbon nanotube can be simplified by diameter d_t and height of T and expressed by followings:

$$\text{Zigzag: } |C_h| = na, \quad T = \sqrt{3}a, \quad \theta = 0 \quad (1-8)$$

$$\text{Armchair: } |C_h| = \sqrt{3}na, \quad T = a, \quad \theta = 30^\circ \quad (1-9)$$

The Physical meanings of T is the unit length of the carbon nanotube along the axial direction. As shown in Figure 1-3, the unit cell of the CNT is rectangular OABB', which can be defined by C_h and T . The number N of hexagonal in per unit cell of CNT can be determined by the area of nanotube unit cell $|C_h \times T|$ and single hexagon $|a_1 \times a_2|$ as following:

$$N = \frac{|C_h \times T|}{|a_1 \times a_2|} = \frac{2(n^2+m^2+nm)}{d_R} = \frac{2L^2}{a^2 d_R} \quad (1-10)$$

As each hexagon contains 2 carbon atoms, hence for a nanotube with chirality C_h the number of carbons N_c is $N_c=2N$.

1.2.2 ELECTRICAL PROPERTY

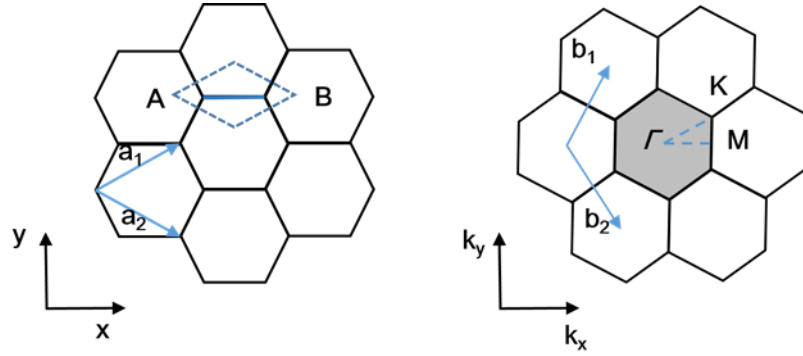


FIG. 1-4 Unit cell and Brillouin zone of graphene in real space and in momentum space. Dotted line and shaded part denote first Brillouin zone in real space and momentum space, respectively.

Another impressive feature of CNTs is that conductivity is directly related to chirality. To understand this unique electronic characteristic better, the momentum space of graphene is referenced. As shown in Figure 1-4, the unit cell of graphene can be described in real space (lattice) and momentum space (reciprocal lattice). Two parameters a_1 and a_2 as unit vectors in Cartesian x - y coordinates with the lattice constant of graphene. Accordingly, in the $k_x - k_y$ coordinates of the reciprocal space, the unit vector is defined as

$$b_1 = \left(\frac{2\pi}{\sqrt{3}a}, \frac{2\pi}{a} \right), b_2 = \left(\frac{2\pi}{\sqrt{3}a}, -\frac{2\pi}{a} \right) \quad (1-11)$$

As shown in Figure 1-4, the first Brillouin zone is selected as a gray hexagon, and Γ , K , and M represent the three high symmetry points at the center, corner, and center of the edge, respectively. Like the basic vectors in SWNT's real space, C_h and T , the basic vectors in the reciprocal space are defined as K_1 and K_2 by the following equation:

$$C_h \cdot K_1 = 2\pi; \quad T \cdot K_1 = 0 \quad (1-12)$$

$$C_h \cdot K_2 = 0; \quad T \cdot K_2 = 2\pi$$

Therefore, K_1 and K_2 can be obtained as:

$$K_1 = \frac{1}{N}(-t_2 \cdot b_1 + t_1 \cdot b_2) \quad (1-13)$$

$$K_2 = \frac{1}{N}(m \cdot b_1 - n \cdot b_2) \quad (1-14)$$

From the above equation, we can see that in real space, the size of the Brillion zone is inversely proportional to the size of the unit cell. Therefore, the Brillion area of SWNT is much smaller than that of graphene, becoming the cutting line on the reciprocal lattice of graphene. T and N wave vectors μK_l ($\mu=0,1,2,\dots, N-1$), which are related to the quantized wave vectors from periodic boundary conditions on C_h , resulting in the formation of N electron bands (one π band and one π^* band) and the dispersion relation of $6N$ phonons. N is given by equation (1-10). Along the axial direction, if the length of the carbon nanotubes is infinite, there will be continuous wave vectors. However, for carbon nanotubes of limited length, the distance between the wave vectors is $2\pi/L_l$, in which the L_l is the length of the CNTs.

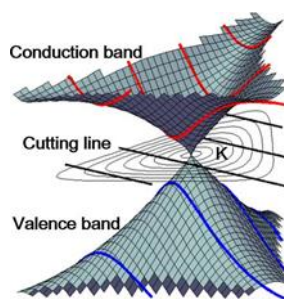


FIG. 1-5 The calculated constant energy contours for the conduction band and valence band for 2D graphene layer. The two bands touch in the K point. Solid curves are the cutting lines for (7, 5) carbon nanotube. (Figure 2-4 (c) was originally plotted by Dr.Yuhei Miyauchi, Kyoto University)

As shown in Figure 1-5, the calculated constant energy profile of the conduction band and valence band of the 2D graphene layer. The two bands touch at point K (K -point), which means zero band. Therefore, the allowable and discrete wave vectors at which the CNT can pass or fail to pass the K -point will result in metal or semiconductor CNTs, which is determined by the chirality (n, m). As the diameter increases, the band gap will decrease, and more wave vectors are allowed in the circumferential direction, which indicates that CNT is being converted from 1D to 2D. Therefore, in order to observe the one-dimensional quantum effect, the CNT must have a sufficiently small diameter.

Another method is to define a vector \vec{YK} as following:

$$\vec{YK} = \frac{2n+m}{3} K_1 \quad (1-15)$$

If the length of the \vec{YK} is a multiple of the length of K_1 , the CNTs are metallic. In particular, all armchair nanotubes represented by (n, n) are metallic, while the zigzag nanotubes represented by (n, 0) are metallic only when n can be divided by 3. Meanwhile, the density of states at the Fermi level determines the conductivity, which we will discuss later. It is worthy of mentioning that calculations show that one-third of CNTs are metallic and the others are semiconducting. As mentioned above, when $2n + m = 3q$, where q is an integer, the carbon nanotube is metallic, otherwise it is semiconducting [23]. As shown in Figure 1-6, a graph of CNTs based on electronic properties is demonstrated.

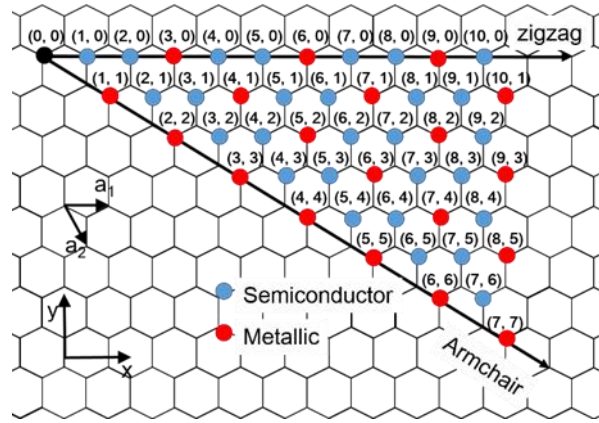


FIG. 1-6 Period table of electrical conductivity for SWNT. Blue and red dots referring to semiconductor and metallic SWNT respectively.

Another important aspect is the introduction of the concept of electronic state density (eDOS), which represents the fundamental difference between metal and semiconductor SWNT. Using the tightly bonded model, the eDOS of metal (5,5), (9,0) and semiconducting (10,5) nanotubes is shown in Figure 1-7. At the Fermi level, the eDOS of (10, 5) is zero, and the energy difference between the two vHSs near the Fermi level is the band gap. Therefore, the 2D graphene forming this SWNT is a zero-gap semiconductor. Correspondingly, the eDOS of metallic (5, 5) and (9, 0) are very small.

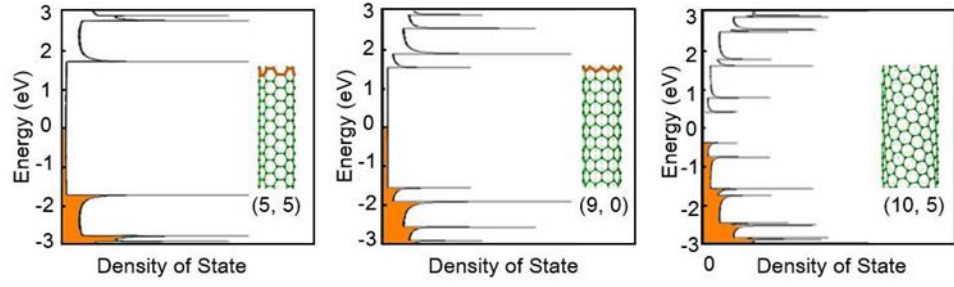


FIG. 1-7 Electron density of state for (5, 5), (9, 0) and (10, 5) carbon nanotubes. (10, 0) is semiconductor behavior and (5, 5), (9, 0) are metallic behavior.

1.2.3 PHONON MODES

The phonon dispersion relationship in CNTs can be obtained from the following equation:

$$\omega_{1D}^{m\mu}(k) = \omega_{2D}^{m\mu}(k) \left(k \frac{K_2}{|K_2|} + \mu K_1 \right), \left(\begin{array}{l} m=1,\dots,6 \\ \mu=0,\dots,N-1, \end{array} \text{ and } -\frac{\pi}{T} < k \leq \frac{\pi}{T} \right) \quad (1-16)$$

$\omega_{1D}^{m\mu}(k)$ denotes the phonon dispersion relation of 1D SWNT, $\omega_{2D}^{m\mu}(k)$ is that of 2D graphene and $\left(k \frac{K_2}{|K_2|} + \mu K_1 \right)$ standing for the quantized wave vectors in the circumferential direction resulting from periodic boundary conditions. m represents the 6 phonon modes of the two carbon nanotubes in a graphene unit cell, per one has 3D vibration. As mentioned above, there are $2N_c$ carbon atoms in per unit cell of a SWNT, the total vibration degree of this system is $6N_c$, therefore the phonon dispersion relation of SWNT consist of $6N_c$ branches of each unit cell.

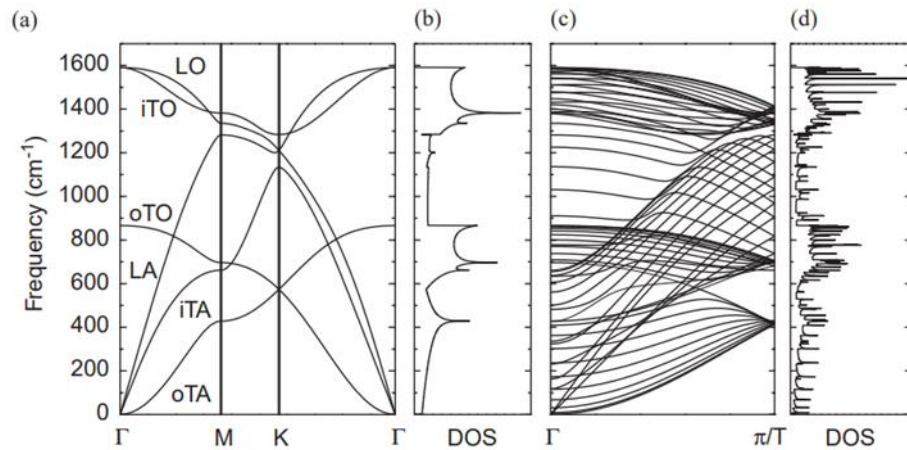


FIG. 1-8 (a) Phonon dispersion relations of graphene sheet, six phonon modes in the order of increasing

energy are out-of-plane transverse acoustic (oTA), in-plane transverse acoustic (iTA), longitudinal acoustic (LA), out-of-plane transverse optic (oTO), in-plane transverse optic (iTO) and longitudinal optic (LO), respectively. (b) The phonon density of states of graphene sheet. (c) Calculated phonon dispersion relations of (10, 10) armchair SWNT, including 120 degrees of freedom and 66 distinct phonon branches. (d) Corresponding phonon density of states for (10,10) SWNT.

In Figure 1-8 (a), the 3 branches derived from Γ are the acoustic modes, arranged in the order of increasing energy is: an out-of-plane transverse (oTA) mode, an in-plane tangential (iTA) mode and an in-plane radial (LA) mode. Figure 1-8 (b) shows the corresponding density of state. Dispersion relation of a typical (10, 10) CNT is plotted in Figure 1-8 (c). In the case of $2N_c=40$, there should be 120 vibration degrees of freedom, nonetheless only 66 phonons branched are observed due to the degeneracies of some modes. Unlike 2D graphene, all the acoustic phonon dispersion relation around the Γ show a linear relationship with k . And there is a fourth acoustic mode for carbon nanotube, relating to the rotation around the tube axis, called twisting mode (TW). But the velocity of this mode is the same with the second iTA mode. As shown in Figure 1-8 (d), the phonon density of state for (10, 10) carbon nanotube is similar with that of 2D graphene, the reason is the calculated method of zone folding method. It is notable that for SWNT, there are numbers of peaks which is not observed in 2D graphene, implies some unique effects from 1D quantum confinement.

1.3 THERMAL TRANSPORT IN CARBON NANOTUBE

1.3.1 THERMAL TRANSPORT IN CARBON NANOTUBES AND ASSEMBLES

The energy exchange is a macroscopic representation of the random movement of material particles in the system. The range of material particles is very wide, electrons, atoms and molecules in gases, liquids and solids are all included. However, the energy carrier is different in various systems. In terms of metals, free electrons and phonons are carriers. But in the case of

semiconductors, the main energy carriers are phonons, since the density of free electrons in semiconductors is much smaller than that in metals. Therefore, phonons are the main heat carrier in 1D SWNT. The heat capacity contributed by phonons is expressed as [24]:

$$C_{ph} = \int_0^\infty \frac{k_B \left(\frac{\hbar\omega}{k_B T}\right)^2 \rho(\omega) e^{\hbar\omega/k_B T} d\omega}{\left(e^{\frac{\hbar\omega}{k_B T}} - 1\right)^2} \quad (1-17)$$

Where $\rho(\omega)$ is the state phonon density. In terms of an isolated SWNT, the above four low-frequency phonons are expected to play a dominant role for heat transfer in the low temperature range. The dispersion relationship of these four acoustic phonons is linear, the relationship between C_{ph} and T at low temperature area as following:

$$C_{ph} = \text{const} \frac{k_B^2 T}{\hbar v}, T \ll \frac{\hbar v}{k_B d_t} \quad (1-18)$$

Where v and d_t are the average speed of sound and the diameter, respectively. For the circumstance of higher temperature, photons will be excited and cause the total heat capacity diverges from the original linearity. Although the weights of these four high-energy phonon modes are significant, the contribution of optical phonons cannot be completely ignored [25].

The thermal conductivity of a phonon in a 1D system is expressed as the sum of all phonon modes and polarizations:

$$\kappa_{ph} = \sum C v^2 \tau \quad (1-19)$$

Where C , v and τ are specific heat capacity, phonon group velocity in the axial direction of SWNT and the relaxation time of a given phonon mode, respectively. Thermal conductivity of free electrons can be obtained from electrical conductivity σ through the Wiedemann-Fanz law:

$$\frac{\kappa_{el}}{\sigma} \approx L_0 = 2.45 \times 10^{-8} (V/K)^2 \quad (1-20)$$

By adding κ_{ph} and κ_{el} together, the total thermal conductivity can be acquired. However, contribution to heat transfer from phonons is much larger than from electrons regardless of the temperatures in SWNT.

1.3.2 THERMAL CONDUCTION METHODOLOGY OF CARBON NANOTUBES

Thermal measurement technique in nanoscale can be divided into two groups: (1) using

external heat source to generate temperature gradient along the nanotube, and (2) applying dc current into the nanotube, or self-heating method, to estimate the thermal properties. Here, several methods will be covered to illustrate the merit and shortcomings of each method.

In terms of external heat source, some classical approaches including the suspended thermometer, T-type nano-sensor and four-probe method. In this study, four-probe method will be adopted and discuss in detail in following chapter.

In terms of self-heating, $3 - \omega$, Raman thermography, dc thermal bridge method is widely applied in experimental study. The common point of these methods is, when CNT absorbs energy, it will generate a temperature gradient along itself, so the thermal information can be obtained by analyzing the temperature curves.

1.4 VAN DER WAALS HETEROSTRUCTURE

The van der Waals (vdW) heterostructures emerging in recent years have attracted wide attention due to the several unique characteristics, which have been applicated in various fields [26, 27] such as devices, catalysis, sense, or energy storage conversion. Using graphene as a spring board, the research on two-dimensional (2D) vdW heterostructures started its blowout growth from 2004 [28]. The structural and electronic changes of vdW bonded layered materials have brought up a new way for basic scientific research and practical device design. Based on the physically assembly from initial building blocks through weak vdW interaction, without the limitation of specific dimension this bondless integration strategy can provide an alternative method of low-energy material integration to apply in. various crystal structure materials (crystallinity, lattice symmetry and constant), electronic properties (metals, semiconductors, insulators and superconductors). In addition to the typical 2D van der Waals heterojunctions synthesized by such non-bonding interactions in a variety of 2D materials, through in-depth understanding of material properties and interfaces, new preparation methods have been developed to make van der Waals heterojunctions not only limited to 2D, more and more van der Waals heterojunctions of other dimensions, such as 0D, 1D, 3D and other mix-dimension heterojunctions were also came out.(Figure 1-9) [29]. Because there is no direct chemical

bonding, vdW integration can create a series of artificial heterostructures and superlattices with atomically clean and electronically sharp interfaces between highly different materials, various vdW interfaces has been constructed in disparate systems [30-33]. The freedom provided by the vdW heterostructures can show some new functions which are not previously possible.

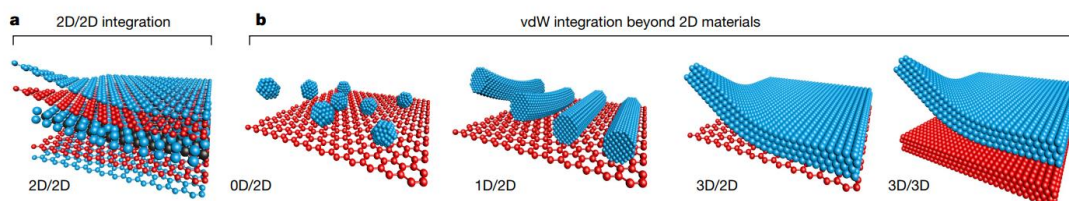


FIG. 1-9 Illustration and structural characteristics of vdW-integrated interfaces. a, b, Schematic illustrations of 2D/2D integration (a) and vdW integration beyond 2D materials (b). Blue and red spheres represent atoms of the integrated and the host material, respectively. (adapted from reference [34], Copyright 2019, with permission from Nature Publishing Group).

In the following three parts, the synthesis method of 1D and 2D van der Waals materials will be briefed, then the properties and applications of vdW heterostructures in recent years will be presented.

1.4.1 SYNTHESIS OF VAN DER WAALS HETEROSTRUCTURE

According to the long-term dichotomy of materials engineering, there are two main strategies for preparing the typical 2D vdW heterostructures: one is the top-down method the other is the bottom-up approaches. The top-down method is originate from the graphene preparation, which is obtained by micromechanical exfoliating natural graphite layer after layer [35]. Moreover, this method has been applied into other dimensional vdW heterostructures. From natural minerals to artificially materials, this kind of method is applicable. Typically, the mechanical exfoliation method is capable of fabricating materials with a high-quality, which is ideal and feasible in terms of the studies in laboratory level. However, as far as the quantity of sheets product and the maximum size of each sheet concerned, it's lack of further scalable ability

which has a limitation of the micrometer range. In order to resolve this problem, more scalable methods have been developed through separation of bulk 2D crystals [36]. However, severe intercalation or severe ultrasonic process are more likely to deteriorate the product quality, in the same time the unexpected impurities are probably introduced into the system, and numerous defects are jointly harmful to the performance and applications. Compare with the top-down method, the bottom-up approaches have higher potentials in fabricating 2D vdW heterostructures with good quality with an easier scalability. The various starting structure blocks through weak interaction and without the violent exfoliation treatment, the structure of pristine materials is more likely to be preserved without severe damage with higher uniformity. Among many methods, various CVD techniques as an outstanding representative of this kind of approach has been applied to prepare many kinds of classical vdW heterostructures.

The typical alignment transfer methods for creating 2D vdW heterostructures is shown in Figure 1-10. a microscope stage equipped with a micromanipulator is essential for correct alignment of micron-level flakes. In the case of typical top-down exfoliation and bottom-up CVD process, the first step of assembly is transferred the pristine 2D layer materials onto an existing substrate. Then, some kind of sacrificial polymer is used to transfer the second 2D layer material flake. After that, the polymer-containing flake is transferred to a transparent stamp, which is positioned using a micromanipulator to the desired position and orientation concerning the first flake, followed by a lower down process until the two flakes contact with each other to form vdW heterostructures. Although the polymer can be directly dissolved to obtain the expected structure, the residue remain on the top of the surface will definitely hamper further stacking, which is only limited to the assembly of simple two-layer structures or as the last layer of stacking. In order to acquire more complex multilayer structure with no residual polymer, more advanced such as peel-off and pick up techniques were developed [37].

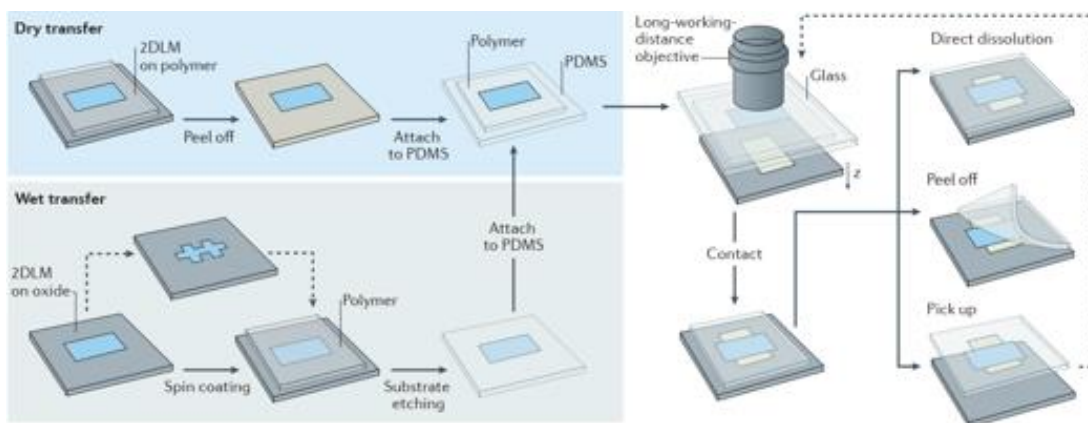


FIG. 1-10 Assembly and characterization of 2D–2D vdWHs. (adapted from reference [29], Copyright 2016, with permission from Nature Publishing Group).

The two strategies also have been applied into the preparation of 1D dimensional heterostructure. As a classic 1D material, based on the CNTs to construct 1D van der Waals heterojunctions is an intriguing issue. An ideal 1D vdW heterostructure can be a coaxial structure with different types of nanotubes. For example, a 1D vdW heterostructure is 4~5 nm in diameter contained three different coaxial layers, an inner CNT, a middle hexagonal boron nitride nanotube (BNNT) and an outer molybdenum (MoS_2), as shown in Figure 1-11. The heterostructures formed through an open-end growth mode that has rarely been observed in previous 1D nanostructure growth. On the basis of bottom-up concept, a SWCNT was selected as the starting blocks to carry out following coating, and the metallic or semiconducting of it can provide the opportunities for electrode and channel material [38]. And other materials such as single-crystalline molybdenum trioxide ($\alpha\text{-MoO}_3$) nanotubes (MONTs) can be grown on CNT surfaces to form a 1D van der Waals heterostructure via vdW epitaxy, which shows potential applications for optical and optoelectronic devices [39].

One-dimensional van der Waals heterostructures

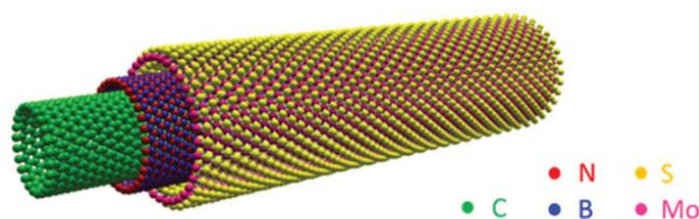


FIG. 1-11 Overview of 1D vdW heterostructures. (adapted from reference [38], Copyright 2020, with permission from AAAS).

These newly developed top-down methods provide great flexibility in creating different heterostructures. However, this method is inherently difficult to scale up from laboratory-scale preparation to mass preparation. In contrast, bottom-up strategy, such as direct CVD growth of heterostructure construction, has greater advantages at this point and has better application prospects [40]. In fact, as a representative bottom-up strategy the direct CVD growth to achieve the goal of vdW heterostructures is usually hindered by the high-sensitivity growth conditions for each layer, hence ensuring high-quality atomic crystal growth without compromise the property of the former structure is hard to reach in mixing and matching. In brief, the bottom-up approach is still not a first choice for creating complex vdW heterostructures, although it has shown many successful examples in many systems. The lattice orientation of crystal is relative stationary with a less flexibility at a certain degree, the mechanical stacking method provides more freedom to adjust the relative alignment between different layers. Therefore, the suitable preparation methods should be determined and developed according to the characteristics of different systems.

1.4.2 PROPERTIES OF VAN DER WAALS HETEROSTRUCTURE

Due to the special structure, vdW heterostructures are able to show some unique properties that the original materials do not have. Whether the layers are precisely stacked or misaligned has a great influence on the properties of vdW heterostructures.

From the perspective of several classic two-dimensional materials that constitute 2D vdW heterostructures, graphene, black phosphorus, TMDs (Transition Metal Dichalcogenides), the band structure of them are all layer-dependent. In addition, appropriate thermal annealing treatment can reduce the interlayer distance to induce the coupling between layers [41]. This kind of interaction is confirmed by both the characteristic peak shift in Raman spectra and photoluminescence shift in emission spectra, which not some individual spectra addition but a

new peak emerging stand for the bound of heterostructure with adjustable coupling. Using dielectrics to separate materials can also adjust the coupling behavior between layers. Two single-layer graphene separated by a BN film can be used to detect the metal-insulator transition occurred in graphene due to Anderson positioning at low temperatures [42]. In the case of TMD system, the interlayer coupling of vdW heterostructures can be adjusted by the separation of the BN layer. It is found that the number of BN layers is inversely proportional to the coupling effect, so the strength of interlayer coupling can be tune by the number of BN layers, as shown in Figure 1-12 [43]. In addition to the obvious influence of the interlayer distance on the coupling between layers, stack orientation also play an important role. The study found that in the twisted MoS₂ double-layer system, the change of electronic and mechanical coupling is relatively constant in the range of 0°-60°, and the strongest at the two vertices, corresponding to two typical stack mode (0°, AA stack; 60°, AB stack), as shown in Figure 1-13 [44]. Besides, the electronic properties of 1D interfaces in the 2D system is more attractive and need to be further investigated. The first principle calculation results reveal the electronic and magnetic properties of 1D interfaces of 2D GeC/BP lateral heterostructures, it shows when the ribbon width is larger than a critical value, metallicity and spin-polarization will emerge at the interfaces as shown in Fig. 1-14, as a result the 1D interfaces of heterostructure have great potential in electronic applications [45].

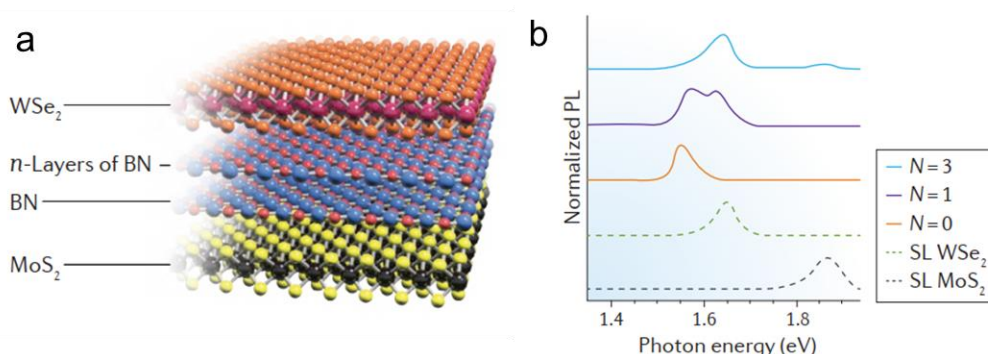


FIG. 1-12 Interlayer coupling in TMD vdWHs. Schematic illustration of a BN-separated transition metal dichalcogenide vdWH with variable interlayer coupling dependent on the number of BN layers, as shown in the coupled photoluminescence (PL) peaks in panel (adapted from reference [43], Copyright 2014, with permission from National Academy of Sciences).

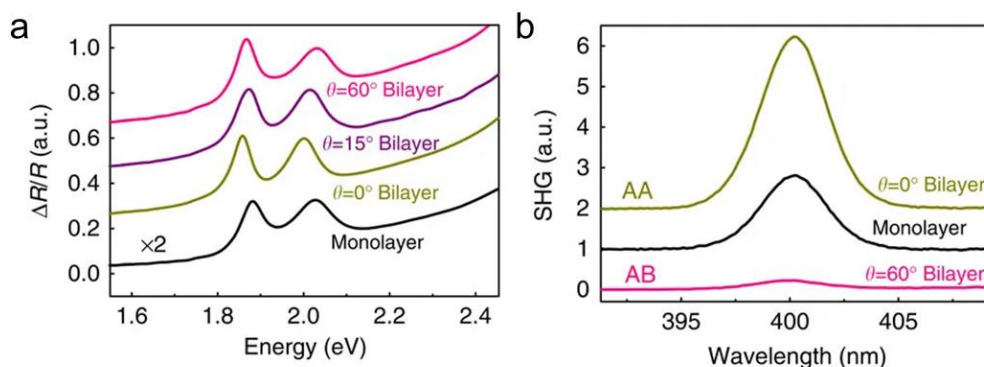


FIG. 1-13 (a) Difference reflection spectra ($\Delta R/R$) from the monolayer and bilayers. The two resonance peaks are characteristics of direct exciton transitions in MoS₂. (b) Second-harmonic generation (SHG) signal from a MoS₂ monolayer, an AA-stacked bilayer ($\theta=0^\circ$) and an AB-stacked bilayer ($\theta=60^\circ$). The traces in a, b are shifted vertically for clarification. (adapted from reference [44], Copyright 2014, with permission from Nature Publishing Group).

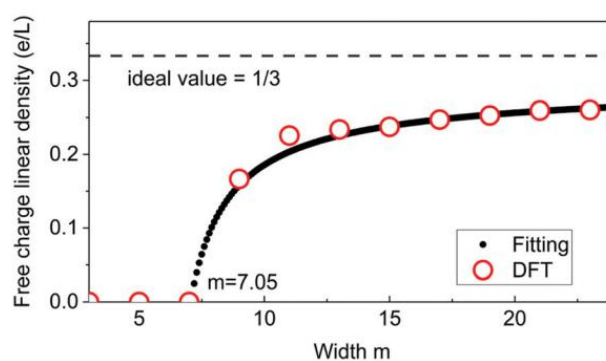


FIG. 1-14 Density of free carriers as a function of ribbon width m for the GeO₂ GeC/BP lateral heterostructure. (adapted from reference [45], Copyright 2019, with permission from RSC).

For vdW heterostructures, the superlattice structure with periodic atomic patterns can be constructed by different atomic thin crystal materials based on their relative orientation (mismatch). During this process, charge redistribution (or electronic strain) and band alignment may occur [46]. If the two single layers have similar or same lattice structures, the moiré pattern formed due to the lattice constant mismatch or twist angle between the two layers will give birth to some unusual properties. Graphene/h-BN vdW heterostructures with moiré superlattice shows extraordinary electronic structure and quantum hall effect, resulting in new Dirac point and band edge [47]. The electronic structure of MoSe₂/WSe₂ vdW heterostructures with Moiré superlattice,

circularly polarized photoluminescence and exciton lifetime can be systematically adjusted by applying electric or magnetic fields, has shown bright perspectives in broader applications [48].

Charge transfer is affected by the diffusion rate in each layer, the band shift between layers, and the built-in electric field caused by surface charge accumulation or uncompensated dopants (although there is no depletion region in thin atomic vdW heterostructures) [49]. Compared with traditional heterojunctions, the smooth and sharp atomic interface of a vdW heterostructures can facilitate charge transfer owing to less scattering centers or charge traps.

As shown in Figure 1-15, regarding the alignment of electronic energy bands, vdW heterostructures between two semiconductors can be divided into type-I (straddling gap), type-II (staggered gap) and type-III (broken gap) [50]. Compared with type-I and type-III, the type-II band is more appropriate for electron-hole separation and subsequent transfer to different material layers. The transfer rate of excited electrons (or holes), also known as exciton relaxation, is affected by the shift of the conduction (or valence) band [51]. The transfer rate becomes faster as the band shift stronger.

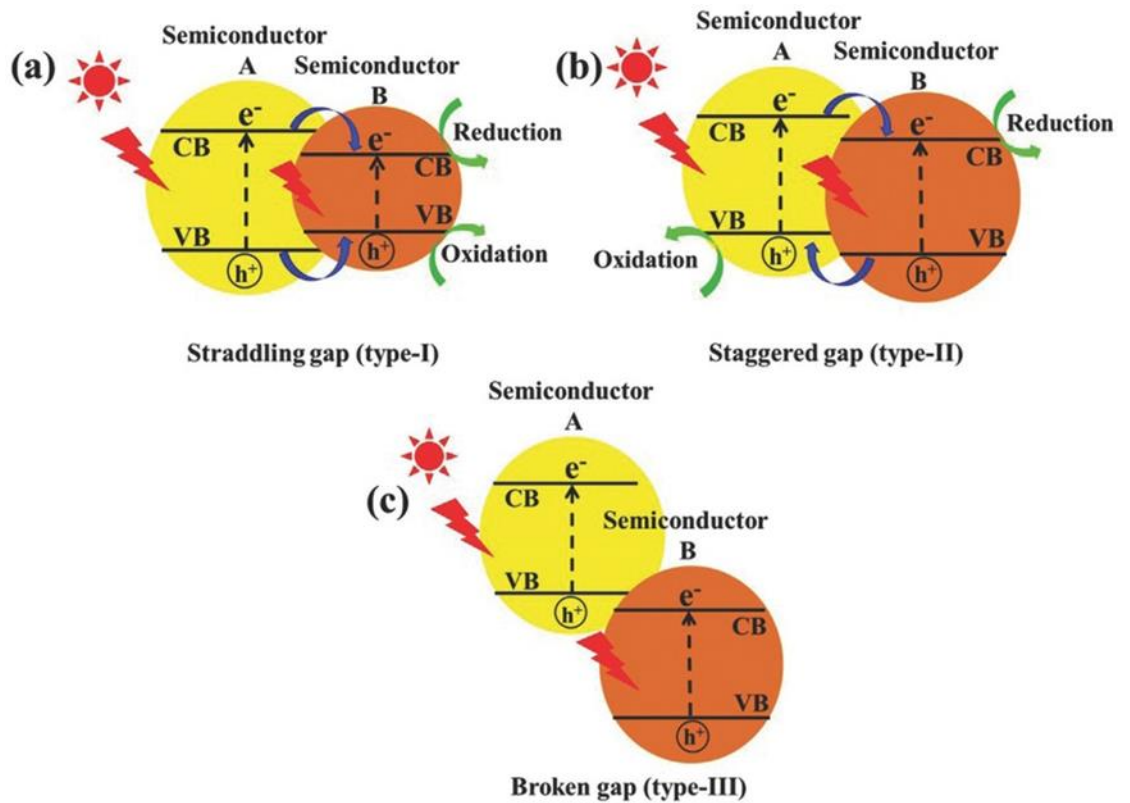


FIG. 1-15 Schematic illustration of the three different types of separation of electron–hole pairs in the case

of conventional light-responsive heterojunction photocatalysts: a) type-I, b) type-II, and c) type-III heterojunctions. (adapted from reference [50], Copyright 2017, with permission from Wiley).

Effective light absorption is a key issue which is essential for the overall performance of vdW heterostructures, especially for the applications in the field of photochemical and photoelectrochemical catalysis. Since the total effective band gap is reduced, the light absorption range of vdW heterostructures is preferably wider than that of a single semiconductor component. And the efficiency of light absorption can be reinforced by tune the layer number of semiconductor component [52].

1.4.3 APPLICATION OF VAN DER WAALS HETEROSTRUCTURE

Because of the extraordinary properties due to the unique structure, vdW heterostructures has been widely applied in many various fields, which can be mainly classified to into four categories: electronics, optoelectronics, catalysis and energy harvesting and conversion [53].

The with atomically clean, electronically clear interface of vdW heterostructure has been used to fabricate diverse electronic devices. For example, the BN/graphene/BN vdW heterostructure displays a ultrahigh carrier mobility from $14000 \text{ cm}^2 \text{ V}^{-1} \text{ S}^{-1}$ to $1000000 \text{ cm}^2 \text{ V}^{-1} \text{ S}^{-1}$ in a condition of room temperature and cryogenic temperature [54]. Similar vdW structure can also be fabricated by a 2D semiconductor channel, 2D insulating dielectric and 2D metallic contacts integrated together, realizing quantum oscillation and highest carrier mobility in various 2D semiconductors [55]. In addition to the traditional planar structures, another important progress for this kind of vdW devices is to achieve a switchable vertical transport mechanism based on tunable tunneling or thermionic barriers by sandwiching 2D insulators or semiconductor channels between graphene electrodes into vertical transistors [56]. And a graphene/BN vdW heterostructure with vertical structure enables efficient photocurrent generation, which achieves a maximum external and internal quantum efficiency of 55%, 85% respectively [57].

Optoelectronic devices based on various vdW heterostructures have attracted great attention and also show promising application perspective. Different kinds of photodetectors, photovoltaics and light-emitting devices have been developed greatly. Two typical categories of photodetectors are phototransistors and photodiodes [58]. Based on the findings of the carrier transport mechanism in vdW heterostructures and recent advances in the quantum physics of materials, phototransistors such as ultrafast photosensors and efficient memory devices, as well as transparent and flexible devices have been studied intensively. The electrically coupled vdW heterojunction can bring about greater light absorption or photoexcited carrier separation. The graphene/MoTe₂/graphene vdW heterostructures is fabricated by using the powerful Fermi level tunability of single-layer graphene and the vdWs interfaces characteristics without the Fermi level pinning effect, the phototransistors show high photo response performances with on/off ratio of ~ 105 , responsivity of 87 A/W, and detectivity of 1012 Jones and high tunability [59]. Photodiodes usually work in reverse bias mode because the electric field at the junction is large, so photo-excited carriers can be efficiently extracted. Atomically thin TMDCs are used as the n-type layer, meanwhile the amorphous silicon, small organic molecules and SWCNT film are utilized as p-type, to construct a kind of p-n vdW heterostructure. This kind of p-n vdW heterostructure as an effective photodiode displays concurrent spectral response in visible light and near infrared range, while a ultrafast response time of 15 μ s [60]. As a classic vdW heterojunction, graphene-silicon system is currently the most studied photovoltaic material so far. By etching the window in thermally-grown SiO₂ on Si and then performing graphene transfer, the power conversion efficiency can reach to $\sim 2\%$ [61]. The principle of a light-emitting device is that when a photovoltaic cell is operated under a forward bias, electrons and holes that are electrically injected can radiatively recombine in the semiconductor to emit light. N-type monolayer MoS₂ and p-type silicon can construct a vertical vdW heterostructure, realizing the light emission under the condition of forward bias owing to the injected holes recombining with electrons. This light emitting device can operate as solar cells, displays a high typical external quantum efficiency exceeding 4% [62]. A 1D vdW heterostructure SWCNT@BNNT consisted of a BN layer grown to wrap around CNT by CVD as a high power-tolerant saturable absorber, the 1D heterostructure shows no visible damage occurred even up to 175 mW and the optical

damage threshold is 5 times higher than pristine materials and with reducing the damage rate, which is a great potential for various high-power optical applications [63].

Using the unique properties of vdW heterostructure, such as tunable electronic band gap, energy band arrangement, light absorption, coupling effect and effective charge transfer and separation, effective photocatalytic and electrocatalytic processes can be effectively conducted. A variety of vdW heterostructures have been used as high-efficiency photocatalysts for H₂ evolution, O₂ evolution, and pollutant decomposition reactions [64]. Due to the high exposed active site of metal 1T-MoS₂ and low Schottky barrier provided by O-g-C₃N₄, along with the enhanced light absorption by the interaction between them, the photocatalytic HER is obviously improved to 1841.72 μmol/g/h with an external quantum efficiency of 7.11% [65]. Morphology, edges, defects, interfaces and electronic structure are all the important factors to the electrocatalytic performance of vdW heterostructures. Morphology determines the mass transfer of reactants and the accessibility of active sites. The edges and defective parts usually have catalytic activity. The redistribution and transfer of charges at the interface will affect the adsorption energy of the intermediate and the energy barrier of the reaction. A kind of vdW heterostructures consisting of N-doped MoS₂ and graphene has proven to be a trifunctional electrocatalyst, which displays a low overpotential of 243 mV and 400 mV at 10 mA cm⁻² for HER and OER, respectively. In the case of ORR, it shows an onset potential of 0.90 V [66]. At present, using the properties of vdW heterostructures to realize the combining of photocatalysis and electrocatalysis, so called photoelectrochemical catalysis is expected to exert unique potential, the related research is in progress. Recently, based on 0D graphene quantum dot and 2D pristine graphene, an innovative mix-dimensional 0D/2D vdW heterostructure has developed to achieve the process of water splitting photoelectrochemically. Compared with the pure electrochemical process, the photoelectrochemical process shows a higher current response, which is 2.39 times that of HER and 1.75 times that of OER [67].

vdW heterostructures have also shown great potential in energy harvesting and conversion in recent years. A delicate vdW heterostructures constructed by designing an effective interlayer by combining twinborn TiO₂-TiN heterostructure with graphene sheets. The enhanced performance of this kind of vdW heterostructure is achieved by the smooth diffusion realization

of polysulfides across the TiO₂/TiN interface that reinforces nucleation process and transfer into insoluble products. It displays a high capacity retention rate of 73% and 67% after 2000 cycles at 1C (the corresponding sulfur load is 3.1 and 4.3 mg cm⁻²) [68]. A 1D CNT/BNNT vdW heterostructures shows an enhanced interfacial thermal resistance, which has an order of 10⁻⁷~10⁻⁶ Km²w⁻¹, and it can be further reduced by modulating the LJ potential parameter. A largest rectification factor of ~90% is displayed due to the mismatched phonon spectrum of CNT and BNNT, which means more energies can be carried to take part in thermal transport across the interface [69].

**CHAPTER 2 MOTIVATION,
CHALLENGES AND
ORGANIZATION OF THE
THESIS**

2.1 MOTIVATION AND CHALLENGES

Since the advent of CNTs, it has been receiving extensive attention and achieved a series of important progress in recent years. The unique structural characteristics determine that it has many tempting properties. The application researches of CNT are widely conducted and potential applications have been attempted from FET, thermal interface material, sensors to drug carrier. On the other hand, with the fast development of micro synthesis and processing technology in past decades, energy density in electronics has increased rapidly and the extra heat has limited the stability and longevity of electronics. Nanostructures with high thermal conductivity can be applied in heat dissipation. CNT has been widely considered as a promising alternative given its extracting electrical and thermal property. However, thermal transport in these micro devices has become the key issue that limit the potential application of CNT. Although a comprehensive investigation combining theoretical analysis, MD simulation are conducted to reveal the mechanism behind, insufficient experimental study still makes it difficult to offer guidance for practical application. Briefing the heat transfer mechanism through experiment will also promote the realization of photonics.

One of the key factors in CNT assemblies is aggregation. The van der Waals forces can easily make an aggregation and result in bundle. The previous simulation results are also in conflicts and disagreements on the actual impact when CNT forming bundles. Therefore, precise identification of structure and corresponding investigation is of great interest. Heterostructure synthesis is an alternative way to tailor nanomaterials according to their property. Without lattice matching and chemical bond, the heterostructure material started from 2D nanomaterials and quickly spread to 1D and even integrated dimensional materials. Besides the merit in synthesizing, target property could be designed and even tuned in some range. Ever since advent, 2D heterostructure material has been studied extensively from all aspects. 1D heterostructure material, on the other hand, has not been systematically investigated because of the difficult in controlled synthesis processing and unsatisfying crystal quality.

The urgent need for clarifying the thermal transport properties dependency on

microscale SWNT bundles and need for filling up the gap in 1D heterostructure material elicit our attentions onto them in the present work, in order to provide scientific guidance for future engineering designs and manipulations through the systematic investigations.

2.2 ORGANIZATION OF THE THESIS

This work aims to (i) study the structure dependent of thermal transport of SWCNT bundles with identified bundle structure. Microelectromechanical systems (MEMS) technology is used throughout this work to synthesize micro measuring system for 1- dimensional nanoscale materials. (ii) Improve the current understanding of thermal transport property, electrical property of SWCNT-BNNT heterostructure material, using a quick and handy steady-state IR thermography method study five types of free-standing SWNT thin films before and after annealing, and the corresponding heterostructure film. (iii) Build a concise model of van der Waals heterostructure film to clarify the morphology of SWCNT template and outside BNNT. The structure model further explains the heat transfer mechanisms in the heterostructure film and agree well with the obtained experimental data.

The main components of this work are: (i) structure-dependent thermal property of SWCNT bundles and theoretical analysis, (i) thermal property of SWCNT film based heterostructure and the corresponding model. Accordingly, these studies are presented in detail in Chapter 3 and Chapter 4.

Chapter 3 examines the effect bundling on thermal transport in suspended SWCNTs. The thermal conductivity of SWCNT bundle has been transferred to a micro thermometer which enables the detailed TEM observation of the bundle structure. Three bundles with SWCNT number of a 2, 3 and 4 are successfully synthesized and their thermal conductance and thermal conductivity are calculated. These three new data point fit in well with the previous data, bundles consisting 1, 5, 8, 13 SWCNTs. Though a kinetic theory fitting analysis, phonon scattering mechanisms in a bundle is concluded to be influenced by the average interaction per tube. The lower κ that calculated for suspended SWCNT bundle with large size is attributed to an increased scattering of phonons with the neighboring SWCNT. A correction factor is adopted to have a

better description of the calculated data. The thermal conductivity decreases with number of SWCNT in a bundle at a varying speed. The phonon transport is slightly suppressed by intertube interaction for small bundle size and largely impeded with the number of SWCNT increasing. This quantitative negative correlation gives a critical design parameter for potential SWCNT application and researchers in that field.

Chapter 4 reports sheet thermal conductance measurements of heterostructure film grown by chemical vapor deposition (CVD) on five types of suspended SWCNT film. based between two suspended micro-thermometers (Transparency 95%, 90%, 80%, 70% and 60%). The structure of the samples is characterized in detail scanning electron microscope SEM and transmission electron microscopy (TEM). The sheet thermal conductance is determined by a quick and contact free IR method. Additionally, the annealing process during CVD growth of BNNT is discussed, which reveals the true state of SWCNT film in a heterostructure. The largest enhancement in sheet thermal conductance after BNNT wrapping is obtained on 90% transparency film, which is over 80%, and the lowest enhancement is observed for the heterostructure film based on the thickest SWCNT film. Furthermore, to study the intrinsic thermal transport mechanism of heterostructure film, a concise model is build based on TEM observation. Analysis based on this model could be used to explain the sheet thermal conductance change as well as locating the weakness of this structure, which has value for future material tailoring.

Finally, Chapter 5 summarizes the major findings of this work.

**CHAPTER 3 STRUCTURAL THERMAL
TRANSPORT PROPERTY OF
CARBON NANOTUBE
BUNDLES**

3.1 BACKGROUND

It is universally known that the graphite has a much-decreased thermal conductivity in comparison with that of graphene because of the weak inter-planar interactions [91]. Measured thermal conductivity of single-layer graphene could reach up to 5000 W/m K [11, 12], while increasing the layers yield thermal conductivity of about 1000W/m K [139-141]. Akin results happened for carbon nanotubes. Measured results on thermal properties of mesoscopic and bulk materials like CNT bundles, mat and films composed of CNT seems lose the outstanding performance of single CNT showed. Despite the quasi-one-dimensional physical property [4], advantage of high thermal conductance of CNT is suppressed by packing fraction, interface resistance between CNTs, boundary resistance between CNT and substrate as well as defects [13]. Single-walled carbon nanotube has rather high thermal conductivity, surpasses that of CNT mats whose thermal conductivity are only on tens of W/m K. Heo [142] reported a thermal conductivity of randomly packed CNT mat with thermal conductivity range from 0.12-0.20 W/m K, comparable low value was also observed by Prasher *et al.* [143], with measured thermal conductivity on the magnitude of 0.155-0.194 W/m K. The low thermal conductivity of CNT films was thought to stem from the large contact thermal resistance between individual CNT.

Besides all the theoretical and simulation on studies, many research works efforted to prove the influence of intertube interaction on thermal property of CNTs, as shown in Figure 3-1. [6-19]However, it is still a challenge thing to precisely identify individual SWNT while perform a reliable measurement.

μm electrode, and these electrodes will be connecting with experimental setup. Horizontally SWCNT will be transferred to cross the heating and sensing membrane. The fabrication of micro thermometer and SWCNT transfer will be introduced in detail in below.

3.2.1 MICRO THERMOMETER DEVICE FABRICATION

The fabrication of the suspended micro thermometer includes wafer-stage process and chip-stage process. At wafer stage, there will be two Electron Beam (E-Beam) Lithography (EBL) and one Reactive Ion Etching (RIE). Then the wafer will be cut into 1-inch square chip. Then each chip will go through one Photo-Lithography (PL), one RIE, one Deep Reactive Ion Etching (DRIE) and chemical etching process.

The measurement device is batch-fabricated on a 4-inch silicon wafer with 300nm less stressed silicon nitride (Si_3N_4) thin layer on both sides through micro-fabrication technology.

- a) Firstly, E-Beam lithography will be conducted to make the patterns for electrodes, leads and serpentine coils.
- b) Then, 2nm Cr and 30nm Pt are then deposited as heating and sensing components in the trenches pattern formed in last step by RF sputter.
- c) The second layer EBL is followed to make the patterns for the suspended Si_3N_4 pads and beams.
- d) Next, RIE is performed with CHF_3 gas to transfer the suspending features from the E-Beam resist to Si_3N_4 thin layer.
- e) Then the wafer is cut into 1-inch chips by a Dicing Saw. Each chip will have 5 row and 15 column of suspended thermometer, with every 3 thermometers in a row formatting a group.
- f) To final release and protect the fragile suspended structures on the front, a deep reactive ion etching (DRIE) window for the suspended micro thermometer alongside with the 3mm circle compatible to TEM characterization are patterned by photolithography from the backside of the chip.

- g) With the thick photoresist protecting other parts, the uncovered Si_3N_4 area is etched by CHF_3 in RIE to expose the below $525\mu\text{m}$ silicon substrate.
- h) Then the exposed silicon substrate is fast etched away by SF_6 and C_4F_8 until only a few tens of micrometer remained to support the front micro structures during later treatments.
- i) After removing the photoresist, the remaining silicon in the window and circle is completely etched away by 1mol/L KOH solution to ultimately suspend the Si_3N_4 pads and beams with heating and sensing serpentine Pt coils and leads. By now, the whole device is complete and the optical images of a typical micro thermometer device is shown in Figure 3-2.

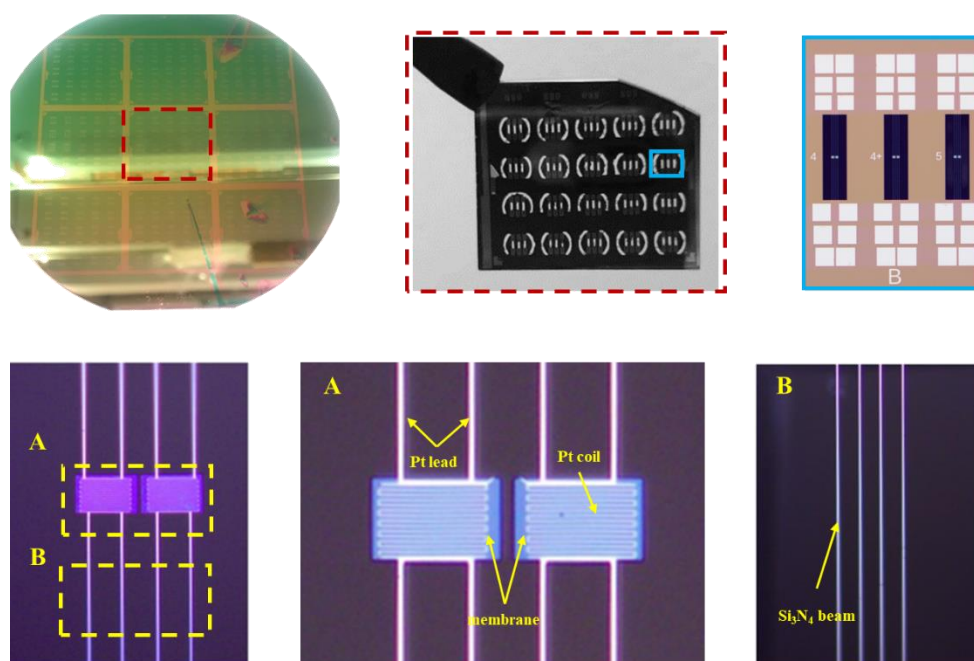


FIG 3-2. Optical images of the micro thermal measurement devices. The first picture is the batch-fabricated wafer, and the second is 1-inch square chip. The following four pictures show the devices in ever higher magnifications and the components of the device are denoted in the pictures.

3.2.2 HORIZONTALLY SWCNT SAMPLE BY CVD METHOD

We used r-cut crystal quartz substrates as substrate for the growth of horizontally aligned SWCNTs. [J. Phys. Chem. C 2013, 117, 11804–11810] The quartz substrate went through a 12h annealing at $900\text{ }^\circ\text{C}$ for 12 h to improve the crystallinity of quartz and thus enhance the degree

of alignment of SWCNTs. Then catalyst lines were patterned in parallel onto the quartz with a certain distance by photo lithography. Distance between catalyst lines could be changed by using different photo lithography pattern. Then catalyst Iron was evaporated by vacuum evaporation with thickness of ~ 0.2 nm. Following vacuum evaporation, the photoresist was removed from the surface of the substrate. Finally, the substrate was annealed in air at $500\text{--}550$ °C for 10 min to remove residual photoresists. Then a typical ACCVD process [32, 113] was conducted to grow HASWNT. Density of the as grown SWCNT could be roughly controlled by the growth time. Figure 3-3 shows a typical SEM image of the as grown horizontal SWCNT (HASWNT) on quartz substrate.

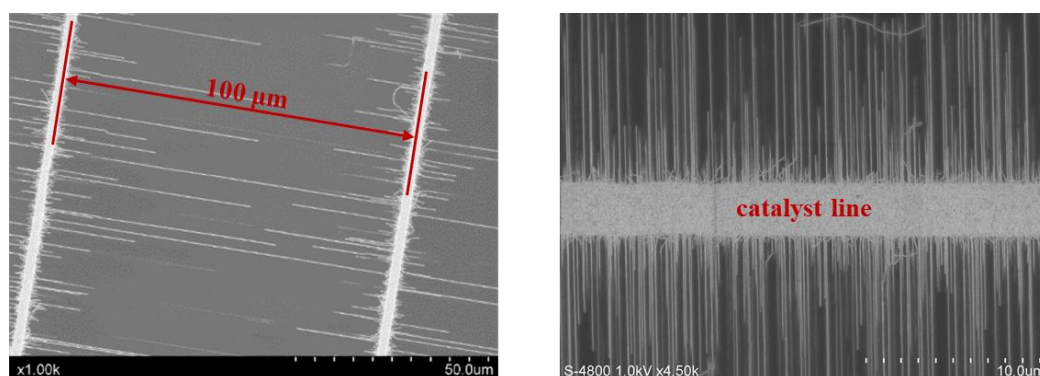


FIG 3-3. SEM of the as synthesized HASWNT with catalyst line distanced $100\ \mu\text{m}$. Image on the right was grown for 20 min with high SWCNT density.

Then PMMA (4% in anisole) was spin coated on the as synthesized HASWNT and peeled off in in 5mol/L KOH solution. The peeled-off PMMA carrying SWCNT was transferred onto the micro thermometer and annealed in clean quartz tube filled with nitrogen at 550 °C over night to decompose the PMMA. While PMMA was decomposing, it would shrink and thus forming bundles. If the density of HASWNT is low, there could be isolated SWCNT left after annealing. The transfer process is shown in Figure 3-5.

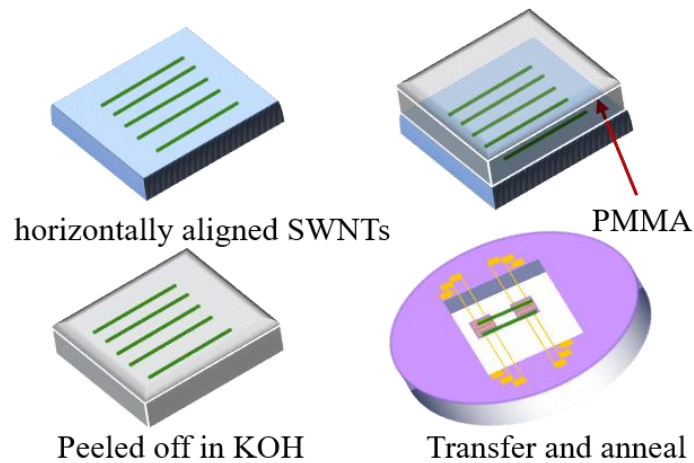


FIG 3-4. Peeled off with PMMA was transfer onto micro thermal measurement chips and annealed in vacuum to remove PMMA.

3.2.3 SAMPLE CHARACTERIZATION

Figure 3-5 shows two successfully suspended SWCNTs samples. In Figure 3-5 (a), the gap between the two membranes is $3.5\ \mu\text{m}$ and one bundle and a single SWCNT cross over the gap. In Figure 3-5 (b), the SWCNT spread long on the membrane, forming enough contact with the substrate. Because the HASWNT grown on quartz substrate are not uniform in length, some micro thermometers will be empty after transfer. These empty micro thermometers could be used as a comparison to measure the background noises.

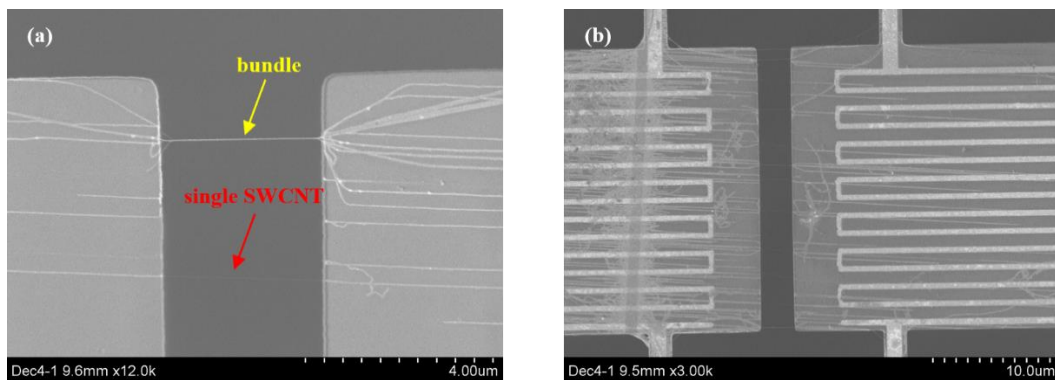


FIG 3-5. Suspended SWCNT bundles and single SWCNT across the heating and sensing membrane. In the left panel, there is one SWCNT bundle indicated by a yellow arrow and a single SWCNT indicated

by red arrow. In the red panel, the SWCNTs spread long on the membrane, increasing the contact area between SWCNT and membrane.

3.3 MEASUREMENT SETUP

The micro-fabricated device is fixed on to a plastic sample holder with electrodes connected by wire bonding, as shown in Figure 3-6 (a). Then the sampler holder is fixed on the sample stage of a high-vacuum cryostat (Janis, VPF-100), as demonstrated in Figure 3- 6 (b). The temperature on the sample is controlled by a cartridge heater and the liquid nitrogen with high accuracy, which is within a fluctuation of 20mK. Because the cryostat has two windows on its body to enable observation of the sample stage inside, a radiation shield is needed. The chamber will be pumped overnight with a turbo molecular pump (TMP) and rotary pump.

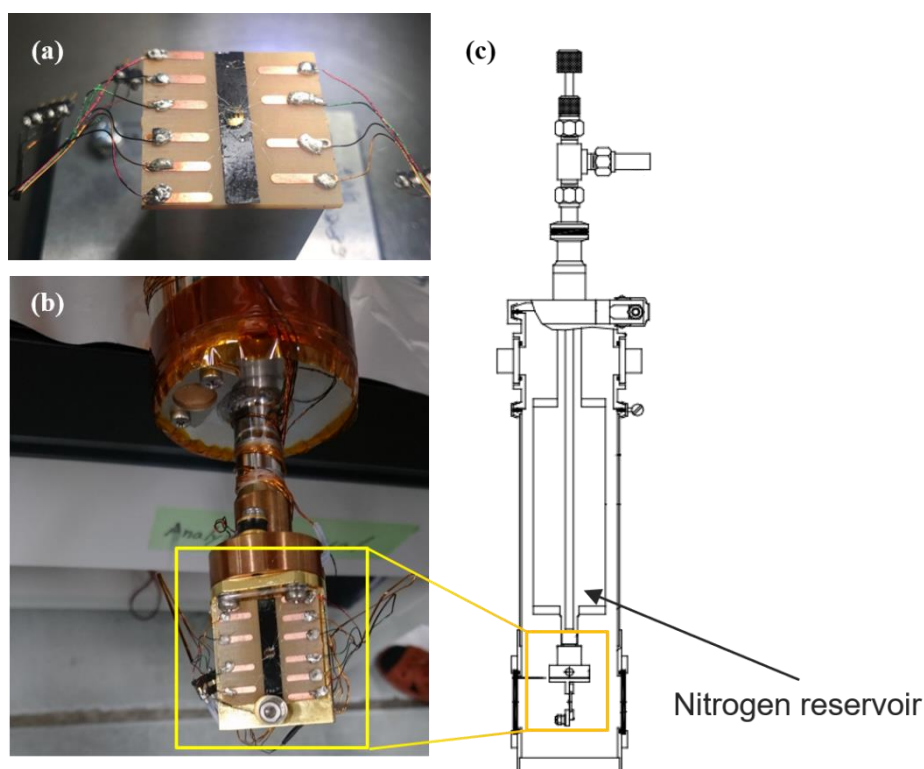


FIG. 3-6 (a) Photo of the sample holder. (b) Photo of the sample stage, and (c) is schematic of the cryostat.

A typical four-point measurement is conducted to measure the resistance of the whole

heating lines (serpentine Pt coil plus two Pt leads of the heating membrane) by Semiconductor Parameter Analyzer (Agilent, 4156C). The analyzer will also apply a DC current to the heating membrane through two leads to generate Joule heat at a stable temperature. Two lock-in amplifiers are separately connected with the heating membrane and sensing membrane to measure the resistance of the serpentine coil before and after the DC current is applied. The data from analyzer and Lock-in amplifiers are recorded automatically for further calculation.

3.3.1 THERMAL CONDUCTANCE MEASUREMENT

To distinguish the different components in the experiment, the subscript is used in the following part. The subscript h is referring to the heating membrane, while the s would be denoting sensing membrane.

After the temperature of the micro-device stables at the set value T_0 , a DC current will be supplied to the serpentine Pt coil on the heating membrane and generating Joule heat of Q_h , which will increase the temperature of the heating membrane to T_h . Part of this heat Q_1 will dissipate to the environment through the four Si_3N_4 beams, and the other part Q_2 will be conducted to the sensing membrane by the SWCNT crossing these two membranes. This will cause the temperature of sensing membrane to increase to T_s . Finally, the temperature of sensing membrane will drop back to environment temperature after the heat dissipated through the four Si_3N_4 beams. The contact resistance is ignored in this study, that is the temperature of the SWCNT on heating membrane equals to T_h and the temperature on sensing membrane is T_s .

The total heat generated is the sum of Q_h and Q_L is determined by the following equation:

$$Q_h + 2Q_L = I^2(R_h + 2R_L) \quad (3-1)$$

where $R_h + 2R_L$ is measured by four-point method.

The temperature increases on the membranes are determined by the resistance changes of the Pt coils. The thermal correlation resistance (TCR) is used. Resistance changes are recorded by the Lock-in amplifier. [70]

$$TCR \equiv (dR/dT)/R \quad (3-2)$$

$$\Delta R_s(I) \equiv R_s(I) - R_s(I = 0); \quad \Delta T_s(I) = \frac{\Delta R_s(I)}{\frac{dR_s(I=0)}{dT}} \quad (3-3)$$

The heat dissipate to the environment through two beams applied with DC current $Q_{hb,2}$, through the other two beams connected with heating membrane $Q_{h,2}$ and through the four beams connected with sensing membrane $Q_{s,4}$ are expressed by the following equations respectively:

$$Q_{hb,2} = 2(G_b(T_h - T_0) + Q_L/2) \quad (3-4)$$

$$Q_{h,2} = 2G_b(T_h - T_0) \quad (3-5)$$

$$Q_{s,4} = 4G_b(T_s - T_0) \quad (3-6)$$

where G_b is the thermal conductance of the Si_3N_4 beam. The heat transferred to the sensing membrane is equal to that conducted by the SWCNT Q_s :

$$Q_{s,4} = 4G_b(T_s - T_0) = Q_s = G_s(T_h - T_s) \quad (3-7)$$

where G_s is the thermal conductance of the SWCNT.

Through the energy conservation law

$$Q_{hb,2} + Q_{h,2} + Q_{s,4} = Q_h + 2Q_L \quad (3-8)$$

besides,

$$Q_{hb,2} + Q_{h,2} = Q_h + 2Q_L - Q_2 \quad (3-9)$$

as a result, the thermal conductance G_s can be determined through the following equations

$$G_b = \frac{Q_h + Q_L}{4(\Delta T_h + \Delta T_s)} \quad G_s = 4G_b \frac{\Delta T_s}{(\Delta T_h - \Delta T_s)} \quad (3-10)$$

here, $\Delta T_h = T_h - T_0$; $\Delta T_s = T_s - T_0$.

As the most important intermediate term in investigation of the thermal conductance of sample, G_b is a self-inspection candidate for the reliability of the measurement system.

3.3.2 UNCERTAINTY ANALYSIS

The voltage signals on heating membrane and sensing membrane are recorded by lock-in amplifier for two minutes (one minute before DC current applied and one minute after DC current applied) when the temperature in the cryostat has been steady. Input signal of the lock-in amplifier are 100 nA AC current at 747.7Hz and 199.03Hz for heating and sensing membrane,

respectively. [71] Figure 3-7 shows the voltage change before and after applying DC current on heating and sensing membrane.

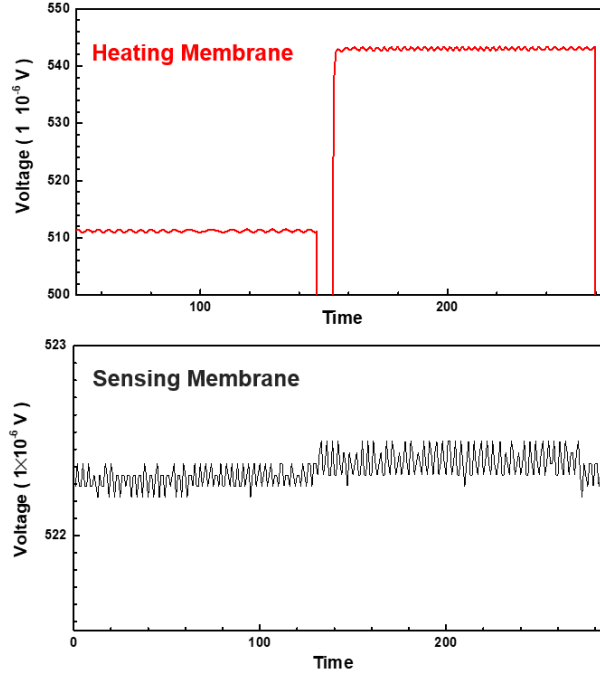


FIG. 3-8 Lock-in amplifier voltage response to DC current heating. The upper panel is the voltage response on the heating membrane when the DC current changes from 0A to 8 μ A at the base temperature T_0 of 78.33K. The below panel is the voltage feedback of the Pt coil on the sensing membrane accordingly.

The resistance is taken 100 times every minute, and the average value is taken as the resistance. Uncertainty of these 100 data point S_R is calculated by taking the standard deviation. The random resistance uncertainty before and during DC current heating S_{Rb} and S_{Rd} are transferred to the random uncertainty of the temperature change through

$$S_{\Delta T} = \frac{\sqrt{S_{Rb}^2 + S_{Rd}^2}}{\frac{dR(I=0)}{dT}} \quad (3-11)$$

According to (3-10), the random uncertainty of the measured thermal conductance can be calculated by

$$S_{G_{s,m}} = (Q_h + Q_L) \sqrt{\left(\frac{2\Delta T_h \Delta T_s S_{\Delta T_h}}{(\Delta T_h^2 - \Delta T_s^2)^2}\right)^2 + \left(\frac{S_{\Delta T_s}}{\Delta T_h^2 - \Delta T_s^2} + \frac{2\Delta T_s^2 S_{\Delta T_s}}{(\Delta T_h^2 - \Delta T_s^2)^2}\right)^2} \quad (3-12)$$

After background deduction, the thermal conductance of the sample is $G_s = G_{s,m} - G_{bg}$, and its uncertainty can be determined by

$$S_{G_s} = \sqrt{S_{G_{s,m}}^2 + S_{G_{bg}}^2} \quad (3-13)$$

3.3.3 NOISE AND SENSITIVITY

From Figure 3-8, temperature rise on the heating membrane is far larger than that of the sensing membrane, and ΔT_s might be submerged with system noises. The noise comes from the cryostat itself or the fluctuation in the measurement devices. It is necessary to calculate the possible measured noise equivalent thermal conductance. If we consider equation (3-10), and replace ΔT_s with noise $\Delta T_{s,noise}$:

$$G_{noise} = 4G_b \frac{\Delta T_{s,noise}}{(\Delta T_h - \Delta T_{s,noise})} \quad (3-14)$$

The temperature fluctuation is approximately $\Delta T_0 = 20\text{mK}$ by the temperature controller, so the equivalent thermal conductance will be:

$$G_{\Delta T_0} = 4G_b \frac{\Delta T_0}{(\Delta T_h - \Delta T_0)} \approx 4G_b \frac{\Delta T_0}{\Delta T_h} = 4G_b \left(\frac{dR_h}{dT}\right) \left(\frac{\Delta T_0}{\Delta R_h}\right) \quad (3-15)$$

which is on the order of 10^{-10}W/K at room temperature.

Another noise source is in the resistance in the voltage and current supplied by the lock-in amplifier. The voltage and current will lead to a resistance fluctuation $\Delta R_{s,electrical}$ and will result in a noise temperature rise of $\Delta T_{s,electrical}$, the noise equivalent conductance:

$$G_{electrical} = 4G_b \frac{\Delta T_{s,electrical}}{(\Delta T_h - \Delta T_{s,electrical})} = 4G_b \frac{\Delta R_{s,electrical}}{\left(\frac{dR_s/dT}{dR_h/dT}\right) \Delta R_h - \Delta R_{s,electrical}} \quad (3-16)$$

In (3-16), $\Delta R_{s,electrical}$ is related to the noises of the voltage and current supplied by the lock-in amplifier,

$$\frac{\Delta R_{s,electrical}}{R_{s,0}} = \sqrt{\left(\frac{\Delta v_{ac}}{v_{ac}}\right)^2 + \left(\frac{\Delta i_{ac}}{i_{ac}}\right)^2} \quad (3-17)$$

where $R_{s,0}$ is the resistance of Pt on the sensing membrane at a certain temperature, T_0 . The noise caused by voltage fluctuation, Δv_{ac} is dominated by Johnson noise and is expressed as $\Delta v_{ac} = (4k_B T_s R_{s,0} \Delta f)^{1/2}$, which is around 7nV. In the equation, k_B is Boltzmann's constant and Δf is the equivalent noise bandwidth of the measurement, which for the parameters used here is 0.26 Hz in the experiment[71]. Given all the parameters above, $\Delta v_{ac}/v_{ac}$ is on the order of $1 \times 10^{-5} \text{K}^{-1}$. The Poisson noise is the AC current is contributed by $\Delta i_{ac} = (2q i_{ac} \Delta f)^{1/2} \approx 10^{-12}$, where q is the electron charge, rated at the order of $1 \times 10^{-5} \text{K}^{-1}$. In addition, the change of $10 \text{M}\Omega$ resistor in lock-in amplifier would turn the sinusoidal voltage into effective AC current, therefore,

$$\left(\frac{\Delta i_{ac}}{i_{ac}}\right)^2 = \sqrt{\left(\frac{\Delta v_{out}}{v_{out}}\right)^2 + \left(\frac{\Delta R_{10\text{M}\Omega}}{R_{10\text{M}\Omega}}\right)^2} \quad (3-18)$$

here, the output voltage noise $\Delta v_{out}/v_{out}$ is about $5 \times 10^{-5} \text{K}^{-1}$, while the resistor fluctuation $\Delta R_{10\text{M}\Omega}/R_{10\text{M}\Omega}$ is $1 \times 10^{-6} \text{K}^{-1}$, so $\Delta i_{ac}/i_{ac}$ in this case is around $5 \times 10^{-5} \text{K}^{-1}$. Therefore, the measured thermal conductance due to electrical noise in the system is represented by the following equation.

$$G_{electrical} = \frac{4G_b}{\left(\frac{dR_s/dT}{dR_h/dT}\right)\left(\frac{\Delta R_h}{\Delta R_{s,electrical}}\right)^{-1}} = \frac{4G_b}{\left(\frac{dR_s/dT}{dR_h/dT}\right) R_{s,0} \sqrt{\left(\frac{\sqrt{4k_B T_s R_{s,0} \Delta f}}{v_{ac}}\right)^2 + \left(\frac{\sqrt{2q i_{ac} \Delta f}}{i_{ac}}\right)^2 + \left(\frac{\Delta v_{out}}{v_{out}}\right)^2 + \left(\frac{\Delta R_{10\text{M}\Omega}}{R_{10\text{M}\Omega}}\right)^2}}^{-1}} \quad (3-19)$$

With the measured G_b which will discuss in the next section, $G_{electrical}$ can be estimated on the order of 10^{-10}W/K .

The sum of the above two effects is the total noise equivalent thermal conductance

$$G_{noise} = G_{\Delta T_0} + G_{electrical} \quad (3-20)$$

and is plotted in Figure 3-8 (blue triangle).

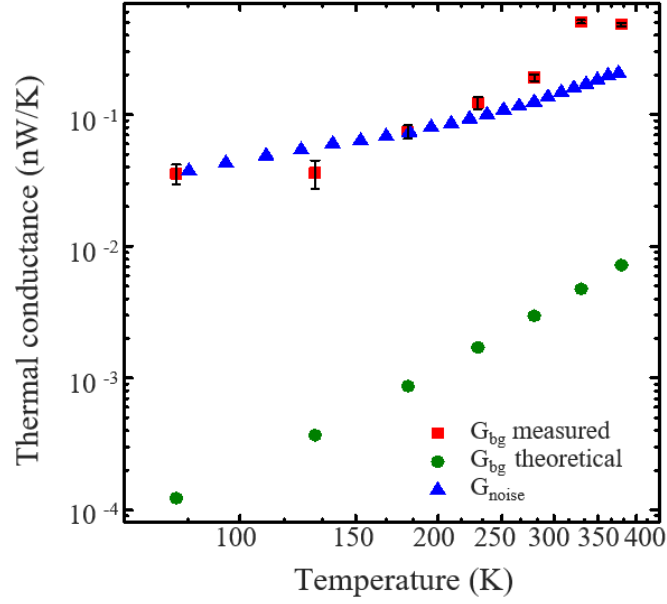


FIG 3-8 Sensitivity limit of the thermal conductance measurement with the temperature increase on the heating membrane about 10K and the base temperature fluctuation of 20mK (Blue triangle). The measured thermal conductance is denoted by red squares. The green dots are theoretically calculated noise.

Although the whole system is kept in vacuum environment, the residual gas molecules are still possible to transfer part of the heat from heating membrane to sensing membrane. Besides, the radiation needs to be considered.

The conductance of residual gas molecules from the heating membrane to the sensing membrane can be estimated as

$$G_{bg,cond} = \frac{\kappa_{air}A}{L} \quad (3-21)$$

here, κ_{air} is the pressure-dependent thermal conductivity of the air and is approximated on the order of $10^{-5} \text{ Wm}^{-1}\text{K}^{-1}$ at pressure of 10^{-2}Pa ; L is the distance in-between the membranes. The estimated value is around 10^{-11}W/K .

The radiation heat transfer between the two membranes can be approximated by

$$G_{bg,rad} = AF\sigma(T_h^2 + T_s^2)(T_h + T_s) \quad (3-22)$$

in which, A , F , σ are the cross-sectional area of the heating membrane, view factor between the heating and sensing membranes (~ 0.5) and Stefan-Boltzmann constant respectively. $G_{bg,rad}$ is in

the range of $10^{-13}\sim 10^{-11}$ from the lowest temperature to the highest temperature investigated in the present experiment.

The calculated thermal conductance of gas molecules and thermal radiation are below the sensitivity limit of this system as discussed before and plotted in Figure 3-9 with green dots. However, the measured thermal conductance ranges from $\sim 3.5\times 10^{-11}$ W/K at 79K to $\sim 6.2\times 10^{-10}$ W/K at 411K, higher than the calculated values in theory, too much to be ignored; indicating that the background measurements are necessary and compulsory to guarantee the precision of the thermal measurements.

3.4 EXPERIMENTAL RESULTS AND DISCUSSIONS

The thermal conductance measurements and sample identification were performed on the same single SWNTs or SWNT bundles across the two suspended micro-thermometer devices.

3.4.1 THERMAL CONDUCTANCE OF SUSPENDED BEAM

The thermal conductance of the suspended beam is an important self-inspection for determining the effectiveness of the measurement system. Theoretically the thermal conductance of Si_3N_4 beam can be calculated given the geometry of the suspended Si_3N_4 beam, the thermal conductivity of it, and the geometry of Pt films sputtered on Si_3N_4 beam and the room temperature thermal conductivity values of Pt [14, 72], in which $\kappa_{\text{SiN}_x}=5.5\text{Wm}^{-1}\text{K}^{-1}$ and $\kappa_{\text{Pt}}=70\text{Wm}^{-1}\text{K}^{-1}$, the thermal conductance of suspended beam can be obtained to be around 12.8nW/K.

On the other hand, the thermal conductivity of Si_3N_4 beam is calculated through equation 3-10 and plotted in Figure 3-9. The three thermometers are from different batch of chips. There's a little divergent among the thermal conductivity of the three thermometers. This is because the KOH etching of silicon may vary from chip to chip. But the thermometers on the same chip go through same fabrication process, the thermal conductance of the beams are the

same. Therefore, for each SWCNT bundle measured, another sample without SWCNT from the same chip should be used to calculate the background noise. The measured thermal conductivity of beams are in good agreement with the theoretical calculation, indicating the functionality of the measurement system.

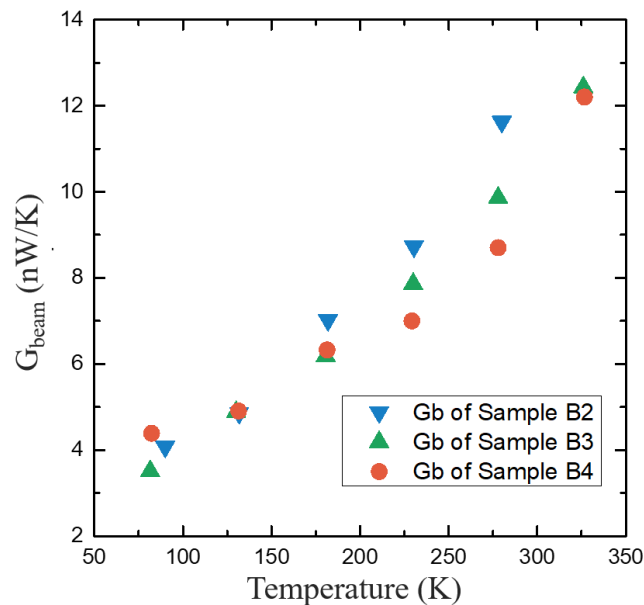


FIG. 3-9 The thermal conductance of the supporting Si₃N₄ beam increases with temperature.

3.4.2 SAMPLE IDENTIFICATION

In total there are three bundle samples investigated in this study, denoted by B2, B3 and B4 respectively. Where B means the SWCNT bundle and the number following it is the size of the bundle. The length of the three samples are 3 μm . The SEM figure of B2 is shown in Figure 3-10, which includes a bundle with 2 SWCNT across the 3 μm gap of the micro thermometer device. The end of those two SWCNT extended long on the membranes are denoted with number 1 and 2.

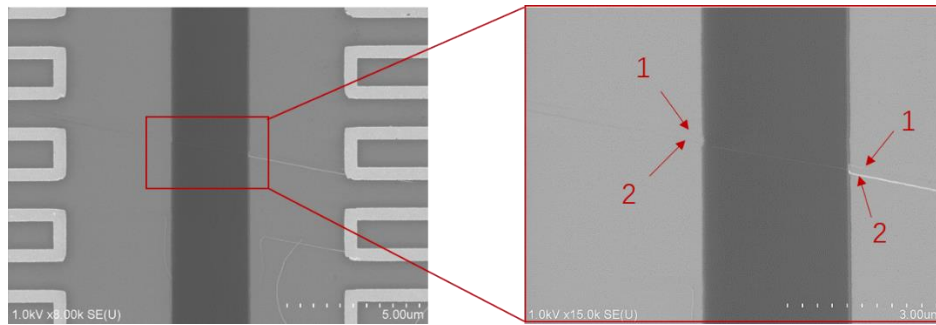


FIG. 3-10 SEM image of sample B2, with two SWCNT forming into one bundle. The gap between two thermometers is 3 μm.

The other two SWNT samples are shown in Figure 3-11 and Figure 3-12 respectively. It is worth to be noted also in those images that the transferred HASWNTs remain tens of micrometers on both membranes to keep the suspended part very straight over the gap. Besides, these long extended SWCNT form sufficient contact with the membrane which makes the contact resistance ignorable.

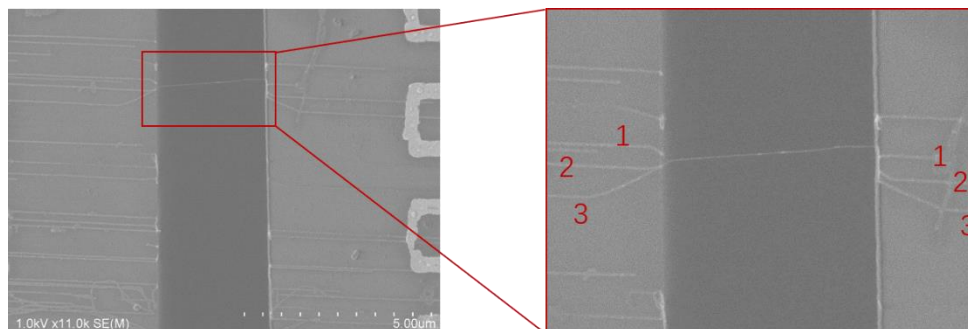


FIG.3-11 SEM image of sample B3, with three SWCNT forming into one bundle. The gap between two thermometers is 3 μm.

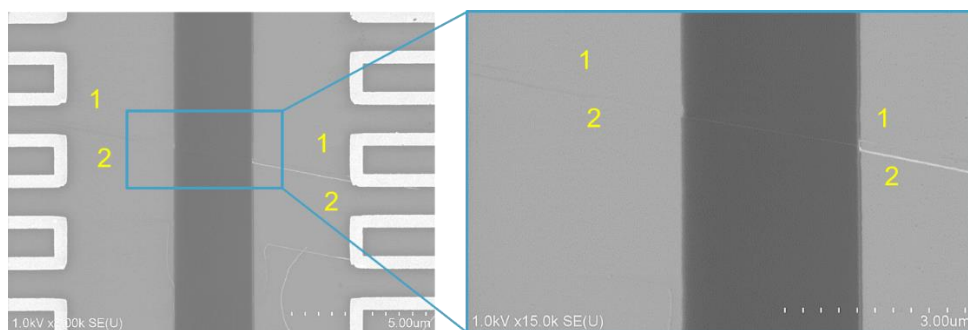


FIG.3-12 SEM image of sample B4, with four SWCNT forming into one bundle. The gap between two

thermometers is 3 μm .

3.4.3 THERMAL CONDUCTANCE OF SWNTS

As explained in Section 3.3.1, the measured thermal conductance can be obtained through Eq. (3-10), and plotted in Figure 3-13. Three different SWNT bundle samples and the background without any SWNTs across the two suspended membranes are investigated in the temperature ranges from 78K to 410K with interval of 50 K. As elaborated in section 3.3.4, theoretically calculated background noise from thermal radiation and heat conduction is far smaller compared with the sensitivity of the system. However, the measured background noise ranges from 3×10^{-11} W/mK to 5×10^{-10} W/mK, which is comparable to that of sensitivity. This suggests a more considerate evaluation on thermal radiation and residue molecular related conduction.

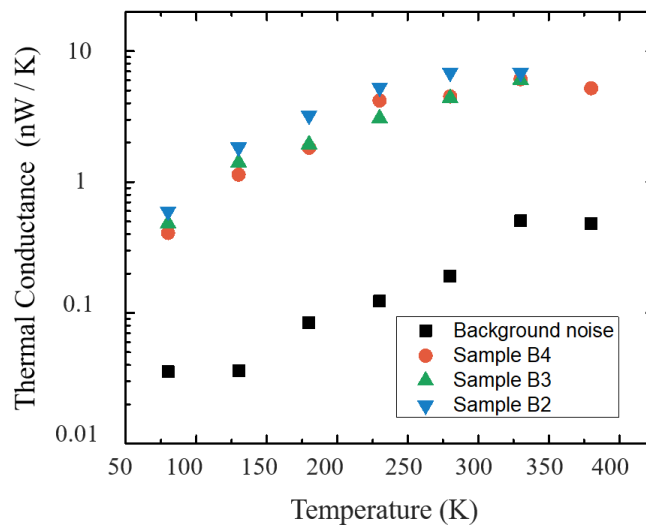


FIG. 3-13 The measured thermal conductance of three SWNT samples, denoted as B2, B3 and B4, as well as the background thermal conductance.

After background deduction, the thermal conductance of the SWNT samples is demonstrated in Figure 3-14. The thermal conductance increases with the temperature first and saturate around room temperature which is in accordance with theoretical predictions[73, 74]

and other experimental observations[75, 76]. Then the thermal conductance of B4 starts to decrease if the temperature further increases. This is because of the second order of Umklapp scattering.[76]

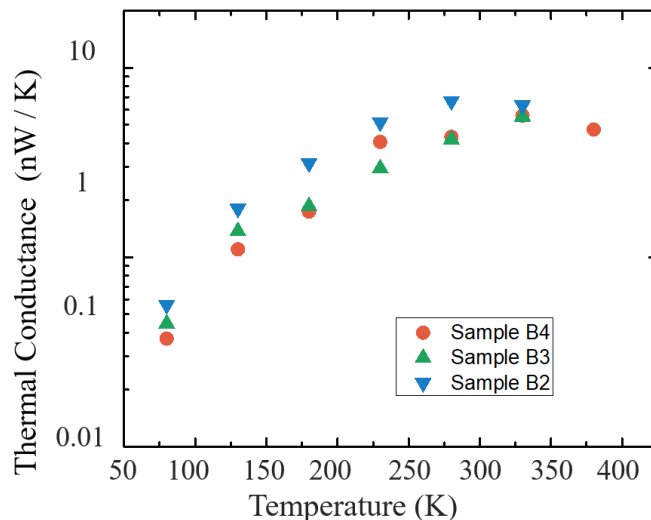


FIG. 3-14 The measured thermal conductance of three SWNT samples after background deduction, denoted as B2, B3 and B4, as well as the background thermal conductance.

3.4.4 EFFECTIVE THERMAL CONDUCTIVITY

The thermal conductivity of the three samples are calculated by $\kappa=G_sL/A$, where L and A are the suspended SWNTs length and cross-sectional area of the samples, respectively. And in this study, the diameter of the SWCNT is assumed to be 2nm [77], the cross-sectional area of a SWNT can be calculated with $\pi\delta D$, in which δ is the thickness of monolayer graphene 0.34nm[78]. Figure 3-15 shows the effective thermal conductivity obtained for SWCNT bundles (B2, B3, B4).

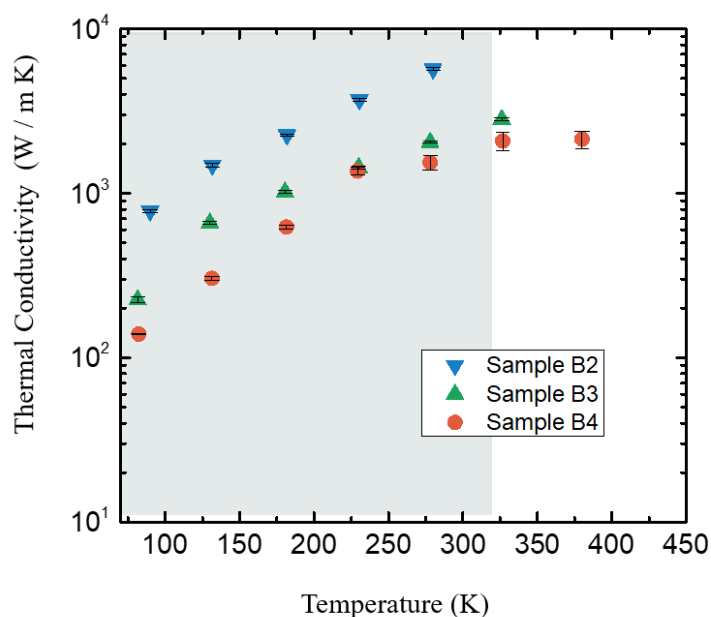


FIG. 3-15 The effective thermal conductivity of three samples versus temperature.

3.4.5 QUANTITATIVE STUDY OF STRUCTURAL DEPENDENT THERMAL CONDUCTIVITY OF SWCNT BUNDLES

To investigate the structural dependent thermal conductivity, the calculated thermal conductivity is plotted against bundle size. Besides, the data from Ref.6 is plotted together in Figure 3-16. The isolated SWNT possesses the highest thermal conductivity, around $5000 \text{ Wm}^{-1} \text{ K}^{-1}$ at room temperature (RT), whereas the thermal conductivity is much lower in SWNT bundles, and decreases with the bundles' sizes. This degeneration of thermal conductivity resulting from three-phonon Umklapp scattering caused by inter-tube interaction[79], which is consistent with other experimental observations[14, 80-83]. Moreover, the speed of degeneration is not constant, from isolated SWCNT to the largest bundle size (13 SWCNTs), the thermal conductivity decreases slowly at first, then drops dramatically at moderate bundle size, and finally become slow again. This phenomenon suggests a more considerate model to study the structural dependent thermal conductivity.

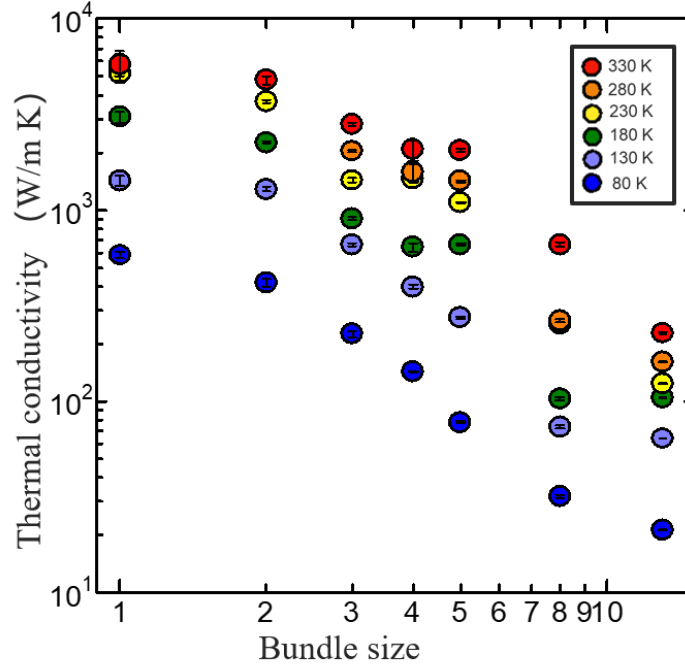


FIG. 3-16 The effective thermal conductivity of three samples versus bundle size.

Kinetic theory[84] (phonon gas) predicts the thermal conductivity in insulators or semiconductor materials as follows:

$$\kappa = \frac{1}{3} C v^2 \tau; \quad (3-23)$$

where C is the lattice volumetric specific heat, v is the average speed of corresponding phonons, and τ is the approximated relaxation time. Besides, τ is the reciprocal of collision rate (γ) between phonons. For an isolated SWNT, its average collision rate is $\gamma_{isolated}$. If expand this equation to SWCNT bundle by taking into the consideration of the inter-tube phonon collision $\gamma_{bundle}(N)$, where N is the additional SWCNT. $\gamma_{bundle}(N)$ should be proportional to the increased number of interactions per nanotube in the bundle.

$$\gamma = \gamma_{isolated} + \gamma_{bundle}(N) \quad (3-24)$$

$$\gamma_{bundle}(N) \propto \text{Number of interactions per tube} \quad (3-25)$$

Therefore, the thermal conductivity in SWNTs can be expressed as (3-26).

$$\kappa = \frac{1}{3} C v^2 \frac{1}{\gamma_{isolated} + \gamma_{bundle}(N)} = A \frac{1}{B + \gamma_{bundle}(N)} \quad (3-26)$$

The thermal conductivity is inversely proportional to the phonons collision rate; with the increase of bundle size, there are increased chances of collision with the neighboring carbon nanotubes. The experimental data is fitted with Eq. (3-26) and shown in Figure 3-17. In the equation, parameter A is related with the specific heat of carbon nanotube and increase with temperature linearly[85], so parameter A is expected to increase with temperature. However, the average group velocities of acoustic phonons that contribute the most to heat transfer depend little on temperature [86]. Parameter B represent the scattering rate in an isolated SWCNT, which is also increase with temperature. In Ref.6, the $\gamma_{bundle}(N)$ is set to inter-tube interaction per tube, that is divide the number of interactions by bundle size.

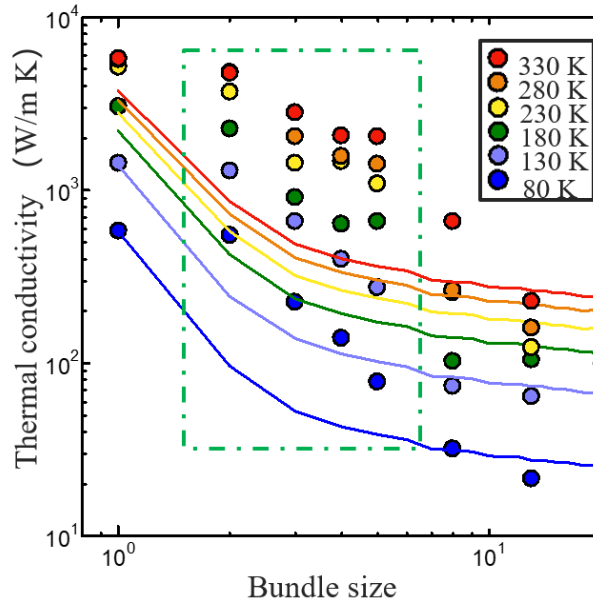


FIG. 3-17 Fitting the experimental data with scattering rate through kinetic theory.

The fitting lines fit well with experiment data for single SWCNT and bundles with size of 8 and 13. But for moderate size bundles, the fitting line fall below the experiment data, and a more considerate discussion on $\gamma_{bundle}(N)$ is needed.

Table 3-1. Bundle size and interaction per tube in the bundle.

Bundle size	1	2	3	4	5	6	7	$3n^2 - 3n + 1$	N
Number of interaction	0	1	3	5	7	9	12	$9n^2 - 15n + 6$	$3N - (12N - 3)^{0.5}$
Interaction per tube	0	0.5	1	1.25	1.4	1.5	1.7	$\frac{9n^2 - 15n + 6}{3n^2 - 3n + 1}$	$3 - \frac{(12N - 3)^{0.5}}{N}$

At the beginning, the relationship of bundle size and interaction per tube is determined. Table 3-1 list the bundle size and interaction per tube of several bundles, and a common expression $\varphi(N)$ is defined to related the bundle size and interaction per tube numerically. As plotted in Figure 3-18, $\varphi(N) = 3 - \frac{(12N-3)^{0.5}}{N}$ describe the interaction per tube precisely.

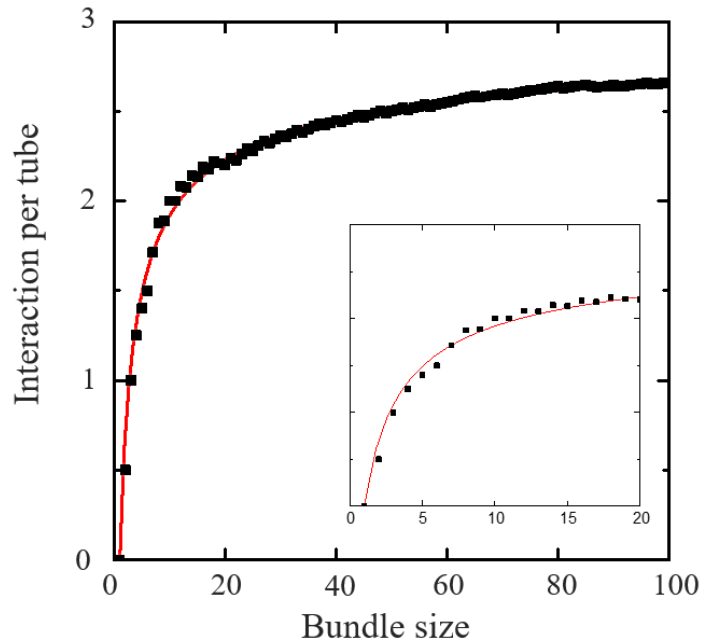


FIG. 3-18 Interaction per tube (black square) fitted by $\varphi(N)$ (red line). The inset shows small bundle size.

As is clear in Figure 3-17, the intertube interaction is over estimated by the model in which $\gamma_{bundle}(N)$ is linearly related with interaction per tube and that $\varphi(N)$ is smaller than 1

shown in Table 3-1, it is straight forward to consider to give $\varphi(N)$ a power factor to cancel make up the overestimation at moderate bundle size. The model is updated as

$$\kappa_{bu}(n) = \frac{1}{3} C v^2 \frac{1}{\gamma_{is} + \gamma_{bu}(n)} = \frac{\kappa_{is}(T)}{1 + A(T) * \varphi(n)^B} = \frac{\kappa_{is}(T)}{1 + \sigma} \quad (3-27)$$

where $\kappa_{is}(T)$ is the thermal conductivity of isolated SWCNT as a function of temperature, and $A(T)$ is a temperature related value, B is a constant power factor. σ represents the phonon scattering rate in bundle scaled by intrinsic phonon scattering in isolated SWCNT, it is not only bundle size related but also influence by temperature. Here, $A(T)$ is expressed as a temperature related function and $\varphi(n)^B$ is only bundle size determined. The combination of these two parts σ will be the function of temperature and bundle size at the same time.

σ are calculated with the thermal conductivity of isolated SWCNT and bundles in this experiment and is plotted in Figure 3-19. As shown in Table 3-1, interaction per tube for bundle 3 is 1, σ equals to $A(T)$. The fitting line of $A(T)$ of bundle 3 is plotted in Figure 3-19. $A(T)$ shows a gentle decline with temperature, indicating that with the increase of temperature, the significance of intertube phonon scattering is decreasing. This implies that the intrinsic phonon scattering increasing faster than intertube phonon interaction. Because $A(T)$ is only temperature related, the distinct difference among σ is attributed to the bundle size. For other bundle size, in order to make the trend of σ match with the experiment data, B is used as a fitting parameter for all five other bundle size and finally 4 is chosen in the following study.

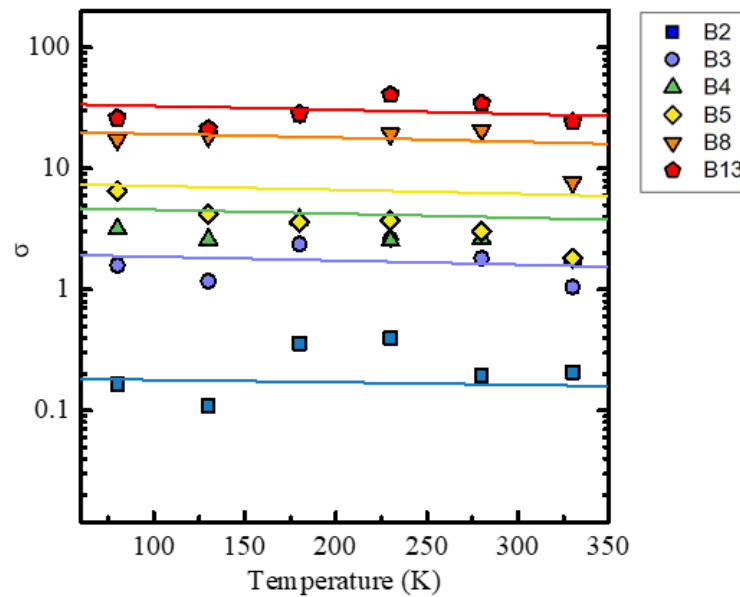


FIG. 3-19 σ at different temperature grouped by bundle size. The lines are fitting lines for $A(T)$.

With $\sigma = A(T) * \varphi(n)^B$ determined, the fitting lines in Figure 3-18 are updated and plotted in Figure 3-20. The colored dots represent measured thermal conductivity of different bundle size grouped by temperature. For all temperatures, thermal conductivity shows a mild decrease from isolated tube to bundle size of 2. Starts from size of 3, the intertube phonon scattering becomes quite effective to reduce the thermal conductivity and approaching to a stable value at infinite bundle size. The decreasing rate at low temperature is not as fast as that in high temperature, in consistence with discussion before. The experiment data falls out of the fitting line as temperature increase, despite the ambiguity in bundle size, larger background noise is another possible reason. With the bundle size keep increasing, $\kappa_{bu}(n)$ reaches a stable value, which is considered to be the thermal conductivity of bulk SWCNT rope. In earlier studies, diffusive thermal transport take place of ballistic transport and saturate in SWCNT with length about micrometer long. Consider the additional phonon scattering in bundles and the shortest bundle length in this study is $2.5\mu\text{m}$, the measured thermal conductivity in this study should be diffusive. The minimum. The limit of thermal conductivity in this study is larger than that reported in other study [], which is possibly caused by the over ten times shorter length of CNT studied.

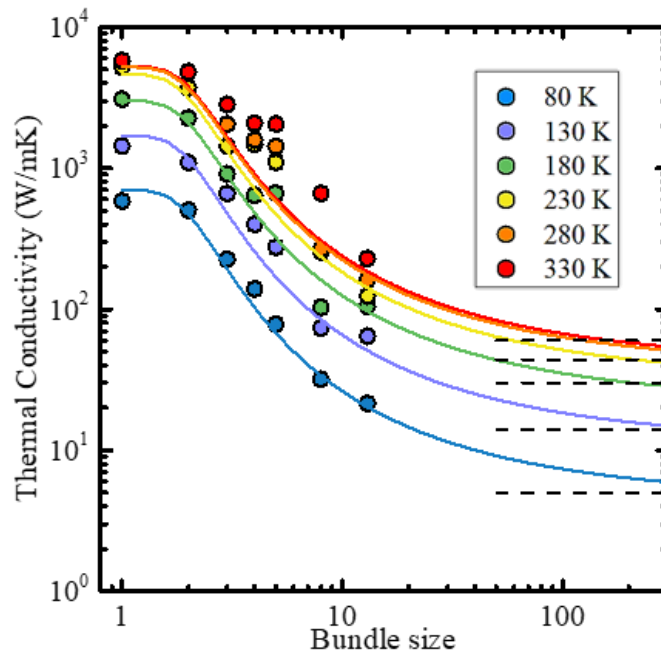


FIG. 3-20 Colored dots in the figure are thermal conductivity plotted against bundle size at different temperature. Fitted with eq. (3-27). The dashed black lines are the bulk thermal conductivity when bundle size reaches infinite.

The κ_{is} in the fitting lines are plotted against temperature with other two works in Figure 3-21 [76]. Here we adopt the equation in Ref.76 and fix the length of the tube to 3 μm in accordance with our experiment. Then the thermal conductivity κ_{is} could be rewrite as $\kappa_{is}(T) = (-5.62 \times 10^{-7}T + 23.96 \times 10^{-10}T^2 + 9.3(1 + 0.5/3)T^{-2})^{-1}$, a function of temperature. In this way, $\kappa_{bu}(n)$ could be extend to all temperature rage together with size range.

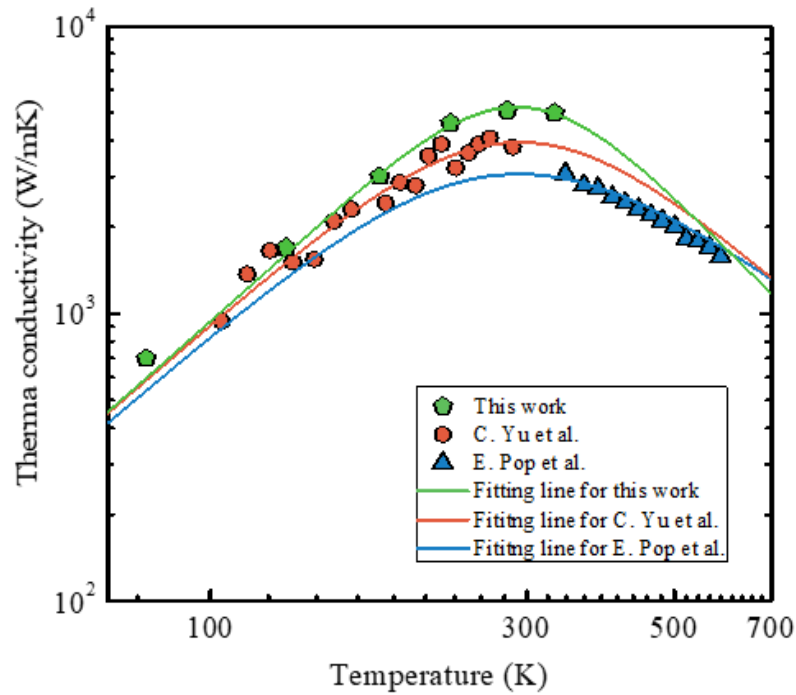


FIG. 3-21 Thermal conductivity of thermal conductivity of isolated SWCNT as a function of temperature with a fixed length. The colored lines are the estimated thermal conductivity versus temperature with fitting parameter are calculated by the dots with same color.

In this way, a common expression for $\kappa_{bu}(n)$ is determined:

$$\kappa_{bu}(n) = \frac{\kappa_{is}(T)}{1+A(T)*\varphi(n)^4} \quad (3-28)$$

where $\kappa_{is}(T) = (-5.62 \times 10^{-7}T + 23.96 \times 10^{-10}T^2 + 9.3(1 + 0.5/3)T^{-2})^{-1}$ (3-29)

$$A(T) = -0.0013T + 2 \quad (3-30)$$

and
$$\varphi(n) = 3 - \frac{(12n-3)^{0.5}}{n} \tag{3-31}$$

3.5 CONCLUSION

In summary, a general study on structure dependent thermal transport property of SWCNT bundle is discussed in this chapter. Micro thermometer compatible of micro meter long SWCNT bundle thermal transport study has been fabricated. Thermal conductance of these samples are tested in a large temperature range from 80 K to 330 K and the result demonstrating perfect agreement with four previous samples with different structure. Then the structure dependent property has been studied quantitatively and summarized to an expression which could be used to estimate thermal property based on number of SWCNTs in a bundle. Intrinsic phonon scattering and intertube phonon scattering has also been discussed with the expression. To obtain a more general expression, a previous study has been included into the expression. The method presented here may be generally applicable to extracting thermal properties of SWCNT based materials with a more flexible customize conditions.

The results show a consistent decline in thermal conductivity with the increase of number of SWCNT in one sample. Kinetic theory has been used to model the thermal transport in bundled SWCNT with a detailed consideration for intrinsic phonon scattering and intertube phonon scattering. The decreasing rate keeps varying with bundle size and this feature is achieved by constructing a nonlinear relationship between the intrinsic phonon scattering in an isolated SWCNT and the additional intertube phonon scattering when neighboring SWCNTs are considered. When the bundle is in small size, intertube interaction is not enough to inhibit too many phonons but with the increase of neighboring SWCNT, the thermal conductivity will decrease dramatically and finally reaches a limit, which is the bulk thermal conductivity of aligned CNT rope. To improve the applicability of this model, temperature and length have been introduced as parameters. This model indicates a slightly higher increasing speed of intrinsic phonon scattering rate as temperature increase, however, the phonons transport impeded by intertube interaction is the main reason for low thermal conductivity of SWCNT bundles.

Continue with previous study, a generally model has been put forward, which includes all the important parameters in thermal transport property discussion like temperature, sample length and sample structure. This model provides an easy and quick way to estimate the thermal

property of any highly aligned SWCNT ropes with a known bundle size. The thermal conductivity of large bundle at room temperature can also be estimated. This model could be extend to MWCNT bundles if the MWCNTs in the bundle could be seen as identical.

**CHAPTER 4 MEASUREMENT OF SHEET
THERMAL CONDUCTANCE
OF THIN FILMS
COMPOSED OF
COAXIALLY COMBINED
SINGLE-WALLED CARBON
NANOTUBE AND BORON
NITRIDE NANOTUBES**

4.1 BACKGROUND

In recent years, van der Waals heterostructures (vdWHs) consisting of different layers of materials weakly bounded to each other by van der Waals interactions have intrigued increasing interest. Using graphene as a basis, vdWHs started from two-dimensional (2D) heterostructures[87] (*e.g.*, graphene, hexagonal boron nitride (BN), 2D metal chalcogenides, and 2D oxides) and developed into a larger field including one-dimensional (1D) heterostructures[88] (*e.g.*, nanowires and nanoribbons) and integration of materials of different dimensions.[89] These vdWHs have been proven to feature unusual properties such as electrical, thermal, optical, and thermoelectric that are not observed previously.[38, 90-93] These properties which could be tailored enable vdWHs materials readily applicable as functional materials and create various possible applications. The construction of heterostructures can be realized mainly by two strategies. One is stacking method where prepared layers of different 2D nanomaterials are transferred on top of each other,[94, 95] and the other is direct synthesis method in which target layers are grown on a starting material.[96, 97] The layer-by-layer transfer is easily operated and the quality of the synthesized material is relatively high. However the insufficient control on the structure parameters, undesired adsorption on the interfaces, and transfer-caused mechanical damages undoubtedly worsen their properties.[98, 99] On the other hand, the synthesis method has attracted considerable attention due to its tunability and controllability. Among all the synthesis methods, chemical vapor deposition (CVD) technology has become a prevailing route to build the various heterostructures[38, 92] owing to the high sample quality and outstanding scalability.[100] Compared with the transfer approach, CVD method is capable of preparing high-purity product with larger domain size and adjustable thickness.

A recent study used single-walled carbon nanotubes (SWCNTs) as a template and synthesized co-axial heterostructures by wrapping SWCNTs with boron nitride nanotubes (BNNTs) and molybdenum disulfide (MoS_2) nanotubes on each other by CVD process.[38] The synthesized BNNT is of high crystallinity and wrapping inner SWCNT uniformly and continuously. The well-crystallized surface and the tailored electrical property of BNNT give this heterostructure material chances in fabricating functional optoelectronic devices. The BNNT

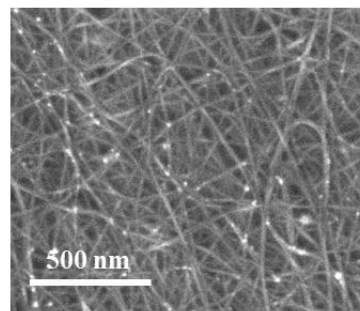
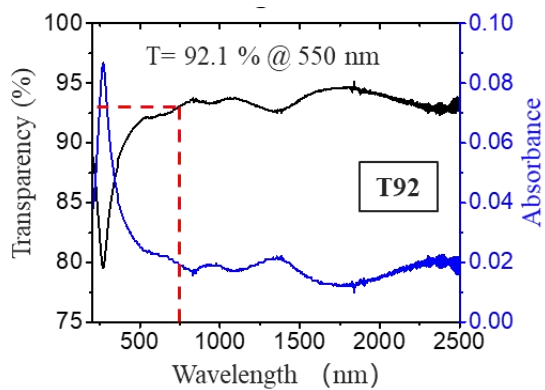
layer can also protect the inside SWCNT from oxidation. In another study, BNNT wrapped SWCNT films were used as a high power-tolerant saturable absorber and is believed to have a significantly higher optical damage threshold as well as a great potential for various high-power optical applications.[92] Constructing heterostructures from BNNTs and CNTs is a promising way to combine the attracting properties of the two materials. Molecular dynamics simulations show that SWCNT-BNNT features good thermal stability and compressive resistance.[101] Experiments on measuring the out-of-plane thermal conductance of MWCNT-BNNTs [102] array achieved a ~90 % increase in thermal conductance compared with that of bare MWCNT arrays.[103] Besides CNT arrays, SWCNTs, which possess high thermal conductivity ($\sim 1000\text{-}5000 \text{ W (m}\cdot\text{K)}^{-1}$ [6, 76, 82, 104]), can also be assembled into random-network films. The 2D film is highly transparent and electrical conductive, which makes it a key player in solar cells working as a transparent electrode.[4, 105] Therefore, it is of great interest to evaluate the thermal, electrical, and other possible properties of heterostructured films made from SWCNT-BNNTs.

In this chapter, the thermal property of the SWCNT-BNNT heterostructured films was studied experimentally, and the mechanism was discussed with a proposed model. The templates used are SWCNT films prepared by the aerosol CVD synthesis method[106] with variable transparency from 52 % to 92 %. The SWCNTs consisting the films have uniformly small diameter, and the thickness of the films is controllable by altering the deposition time.[107] With the SWCNT films as a template, the heterostructured films were prepared by CVD, which can produce conformal and highly-crystalline BNNTs.[38] Then, a contact-free steady-state infrared (IR) thermography measurement was used to investigate the in-plane sheet thermal conductance of the as-synthesized SWCNT-BNNT films. The sheet thermal conductance of the films before and after BNNT wrapping was measured and compared. An enhancement was observed for all samples measured at different degrees of transparency. A quantitative model has been proposed based on random stick network mode and reveals the thermal transport mechanism in SWCNT film. Based on this model, the heat transfer mechanism in this heterostructured material and intertube contact effects were also discussed.

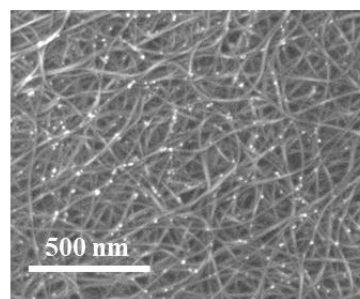
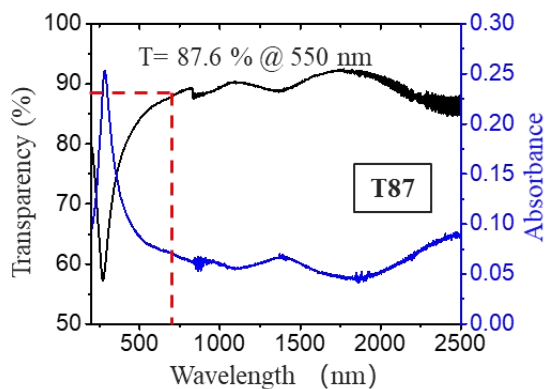
4.2 SAMPLE PREPARATION

4.2.1 ONE DIMENSIONAL HETEROSTRUCTURE SYNTHESIZED BY CVD

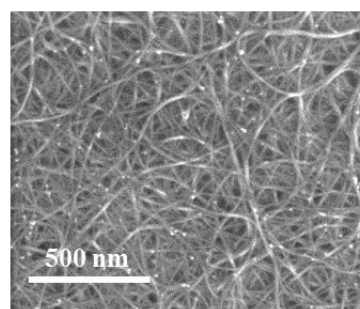
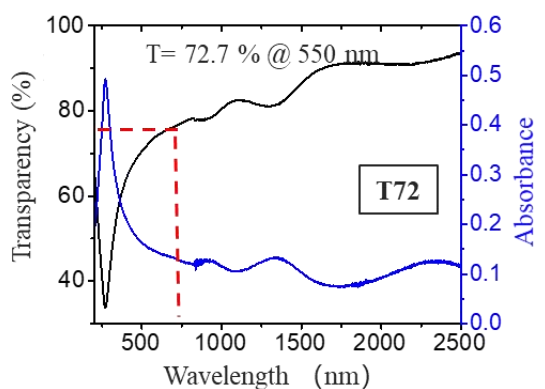
The one-dimensional heterostructure of SWCNT-BNNT is grown by a chemical vapor deposition method using SWCNT film as a template and ammonia borane as precursor [38]. The five types of SWCNT film used in this study were synthesized by aerosol CVD[106] and denoted by their transparency at 550 nm, as shown in Figure 4-1. The UV-3150, Shimadzu is used to measure the transparency and absorbance of SWCNT template films. The characteristic peaks of SWCNTs are located around ~280 nm, ~900 nm, ~1400 nm, and ~2400 nm, which correspond to π plasmon, E_{11}^M , E_{22}^S , and E_{11}^S , respectively. For simplicity, the film will be denoted by the transparency of its template. For the instance, T92 represents the film with 92.1% transparency.



SEM of T92 film



SEM of T87 film



SEM of T72 film

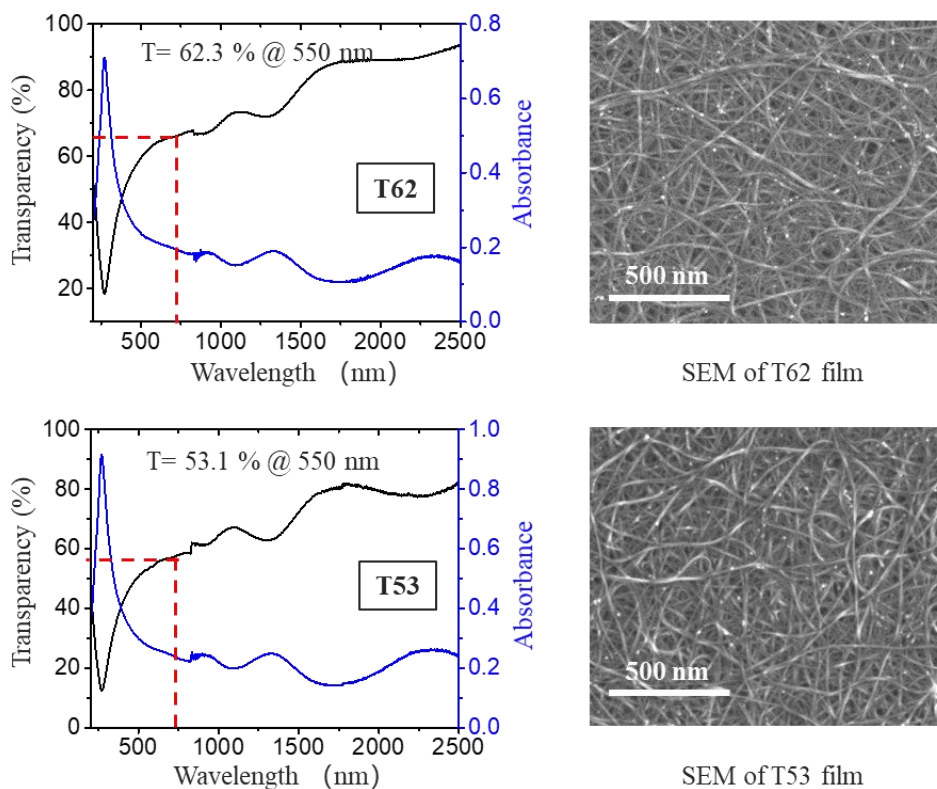


FIG 4-1. UV-vis-NIR spectra of SWCNT films with different transparency at wavelength of 550 nm. The right column is the SEM images of SWCNT films of the corresponding transparency.

Figure 4-2 is a schematic diagram of the CVD process in this study. A 10 mm × 10 mm window was cut onto a 20 mm × 20 mm squares graphite sheets with 1-mm-thick. The SWCNT film with filter paper was placed on the substrate, meanwhile the SWCNT film was downward and the filter paper was upward. Through pushing the edge part, the SWCNT film was tightly connected with the graphite substrate. The SWCNT film was released and suspended on the graphite substrate after the filter paper was removed, followed by a CVD process. Then, as the BNNT precursor, 30 mg of ammonia borane (H_3NBH_3) was placed upstream relative to the sample and heated to 70-90°C through a heating belt. The carrier gas which composed of Ar with 3 % H_2 flowed at a rate of 300 sccm. A low-pressure thermal CVD was performed, and the reaction temperature and pressure were set to 1075°C and 300 Pa, respectively. The coating time influenced the number of external BNNT walls. Underwent 3 hours of the CVD process, BNNTs were distributed along the outer surface of most SWCNTs.



FIG 4-2. Schematic of the CVD process for BNNT growth on an SWCNT template suspended on graphite window.

4.2.2 CHARACTERIZATION OF SAMPLES

Figure 4-3 (a) is an optical image of the as-synthesized heterostructured film (T87). As shown in Figure 4-3 (b), compared with the bare SWCNT film, BNNT increases significant glossiness to the heterostructured film. As shown in Figure 4-3 (c), the film still maintains its flexibility after being wrapped by BNNTs, when released it is able to recover to the original morphology immediately.[108] As shown in Figure 4-3 (d), the SWCNT film easily rolls up, however it's difficult to recovery to the original state due to the adhesion of contacting surfaces. One probable explanation for this phenomenon is the very high surface energy of the SWCNT film.

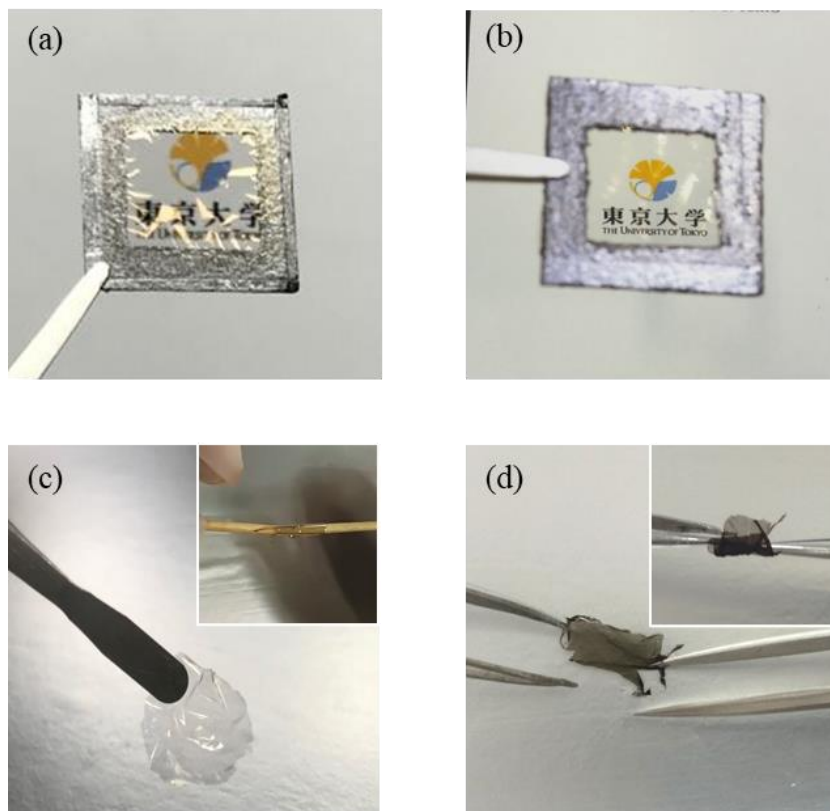


FIG. 4-3 (a) and (b) are optical image of the BN-SWCNT heterostructure film and SWCNT film (T87) suspended over a graphite window. (c) and (d) are the optical image of the SWCNT-BNNT film and SWCNT film after rolled up and released, which confirms the spontaneous shape recovery of SWCNT-BNNT film.

As shown in Figure 4-4 (a), the network morphology of the heterostructured film is displayed in the scanning electron microscopy (SEM) image. The transmission electron microscopy (TEM) images of the SWCNT film before and after the BNNT coating as shown in Figure 4-4 (b) and (c) displayed the morphology change due to the coating. No agglomeration is observed, even after coating, the walls of the tubes are clear and clean. BNNTs coated the suspended individual SWCNT or SWCNT bundles, while at the junctions, they wraps the whole junction rather than each SWCNT, as the inset shows in Figure 4-4 (c). The as-grown BNNT is characterized by multi walled, and its inner diameter is determined by the size of the SWCNT or the SWCNT bundle template, as shown in Figure 4-4 (d). The outer diameter is decided by the number of walls formed during CVD, which can be controlled roughly by the reaction time of

CVD. In this study, a 3 hours CVD process determines the wall number of BNNT is 2-10 walls. As shown in Figure 4-4 (d), an isolated SWCNT is coated by a 3-wall BNNTs. The distance between the BNNT walls is about 0.36 nm, which is comparable to that of multi walled BNNTs.[108, 109]

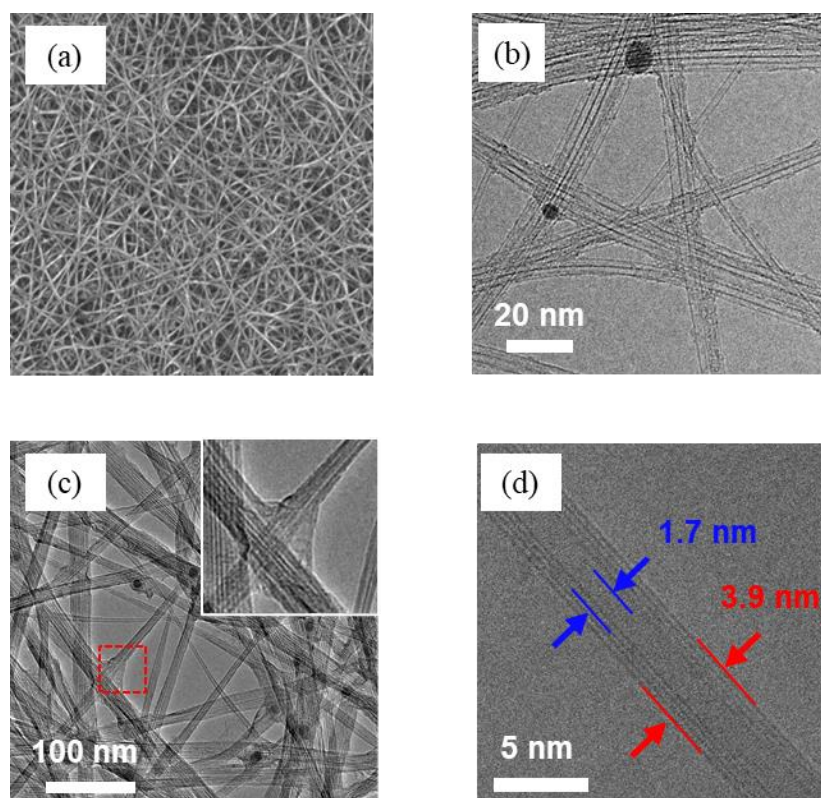


FIG. 4-4 (a) SEM of the BN-SWCNT film and (b) TEM images of a bare SWCNT film. (c) TEM image of the SWCNT film after being coated with BNNTs. (d) TEM image of an isolated SWCNT coaxially coated by a three-wall BNNT. Diameter of the inner SWCNT and the outer multiwall BNNT.

As shown in Figure 4-5, in order to further characterize, Fourier transform infrared (FT-IR) spectra, UV-vis-NIR spectra, and Raman spectra (532 nm excitation wavelength) were performed to investigate the film before and after BNNT wrapping. In Figure 4-5 (a), the signals of in-plane B-N stretching at 1370 cm^{-1} and out-of-plane B-N-B bending at 795 cm^{-1} are detected for the SWCNT-BNNT film, verified the existence of the B-N bond.[91, 103, 110] As shown in Figure 4-5 (b), a band gap of approximately 6 eV is observed, which can be assigned to transitions due to the π - π^* bands of the BNNTs, which is conformed to Rubio's prediction.[111,

112] The B-N-B bending mode at $\sim 797\text{ cm}^{-1}$ is also appeared as shown in Figure 4-5 (c), the zoomed-in spectra further verifies the successful growth of BNNTs.[113] Furthermore, there is no obvious change for the G/D ratio of the bare SWCNT film and the SWCNT-BNNT heterostructured film, which indicates that the crystal structure of the SWCNT is well preserved even after CVD coating .

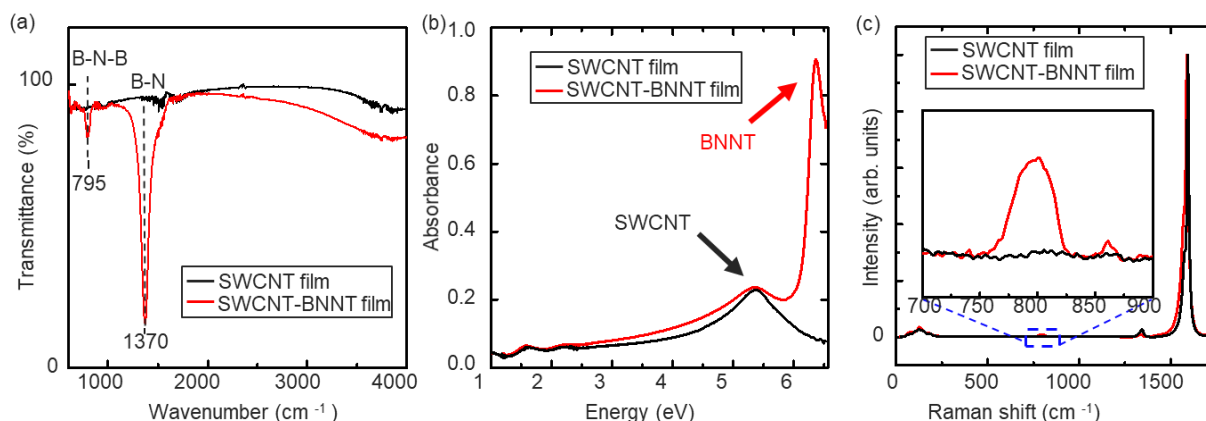


FIG. 4-5 (a) FT-IR and (b) UV-vis-NIR spectra of the T87 SWCNT film before and after the BN coating was applied. These results confirm the successful growth of BNNTs. (c) Raman spectrum of the SWCNT film and BN-SWCNT film.

4.3 EXPERIMENT DESIGN

The principle of the experiment is to utilize a fast and simple method to measure the sheet thermal conductance of the suspended thin films.

4.3.1 EXPERIMENTAL SETUP

The testing system is composed of two parts: a vacuum chamber and an IR camera. The vacuum chamber provides a vacuum environment and has a sample stage which is capable of producing a stable temperature gradient under the known heat flux. The IR camera will read thermal images via the window on the top of the chamber. The experimental setup in this study

is illustrated in Figure 4-6.

The heat source is a copper heater placed in an insulator cuboid cavity and covered with aluminum plate, which is paralleled by a copper heat sink. A pair of silicon cantilevers is composed of two painted silicon cantilevers, which are fixed on the heat source and heat sink respectively, meanwhile aligned with each other. For comparison, another pair of silicon cantilever will not be loaded with sample. The silicon cantilevers with a uniform width of 2 mm and thickness of 100 μm are cut by dicing saw. Temperature of the silicon can be read from the painted surface by IR camera, sample will be transferred to the back of one pair of silicon and cross from one free end to the other. The whole system is preserved in a vacuum aluminum chamber, which is placed on a cooler. The function of cooler is to maintain the aluminum chamber and the copper heat sink at a constant low temperature, while the copper heater in heat source can be controlled at a relative high temperature by connecting to an external temperature controller. In this way, after a period of time, a stable temperature gradient is established along the bridge between silicon and sample. Considering the uniformity of silicon cantilever and sample, the thermal transport can be regarded as a quasi-one-dimensional heat transport. The temperature gradient of silicon cantilever and sample is observed by IR camera through a ZnSe window on the top of the chamber.

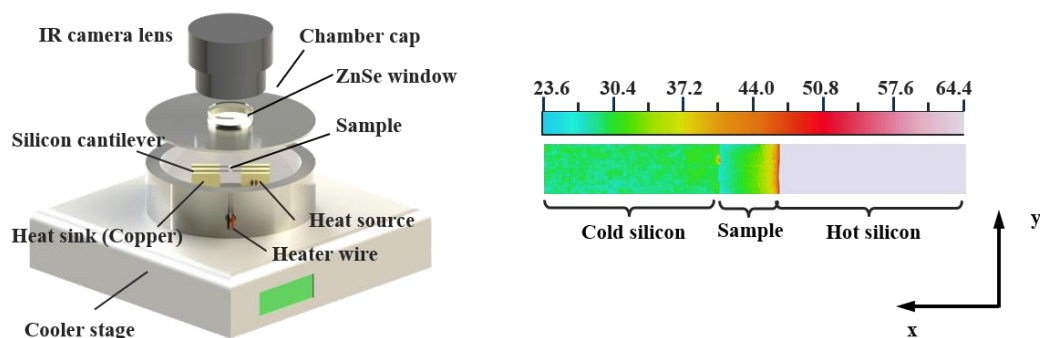


FIG. 4-6 Schematic of the experimental setup for the thermal conductance measurement. A temperature drop is generated by the heat source and heat sink. The chamber is kept under vacuum to eliminate convection. When the heat transport along the quasi-one-dimension reached a steady-state, the IR

thermal imager recorded the temperature profiles for later analyses.

4.3.2 TEMPERATURE MEASUREMENT

Emissivity is required in order to obtain the target temperature from an IR camera. According to Kirchhoff's law, when the surface of the object can be approximately a gray body, emissivity is equal to absorbance. Therefore, the total absorbance of SWCNT thin film and silicon cantilevers was measured by Fourier transform infrared (FT-IR) spectroscopy. As shown in Figure 4-7 (a), the absorbance of T87 film is displayed. Because the Absorbance (emissivity) of samples is lower than the setting limit of the used IR camera, therefore the actual temperature of the samples cannot be obtained directly from the measurement.

An object temperature is determined by the IR camera, which is a function of emissivity and transmission of the air and the observed object. If the effect of atmospheric opacity is neglected, the relation can be simplified as following equation [114, 115]:

$$T_{\text{sample}} = \left\{ \frac{1}{\varepsilon} [T_r^n - (1 - \varepsilon)T_u^n] \right\}^{1/n} \quad (3-1)$$

where ε , T_r and T_u are the emissivity of the object, radiative temperature of the object, and the environmental temperature, respectively. n is a parameter that depends on wavelength; for the HgCdTe sensor (8~14 μm) [116] in our IR camera, $n = 4.09$. T_r and T_u are unknown parameters to be determined.

As shown in Figure 4-7 (b), at different ε the corresponding T_{sample} could be obtained by the IR camera, the data were fitted according to the above equation, along with T_r and T_u for the sample under investigation were gained. Actual temperature of the measured object is the temperature at its emissivity. Temperature was calculated at all pixels along the thermal transport path, and the temperature distribution of a SWCNT-BNNT film and two silicon cantilevers are shown in Figure 4-7 (c). Curves are composed of some fitting lines, in which the fitted data are reflected on the temperature distribution through the dashed lines between Figure 4-7 (c) and (d).

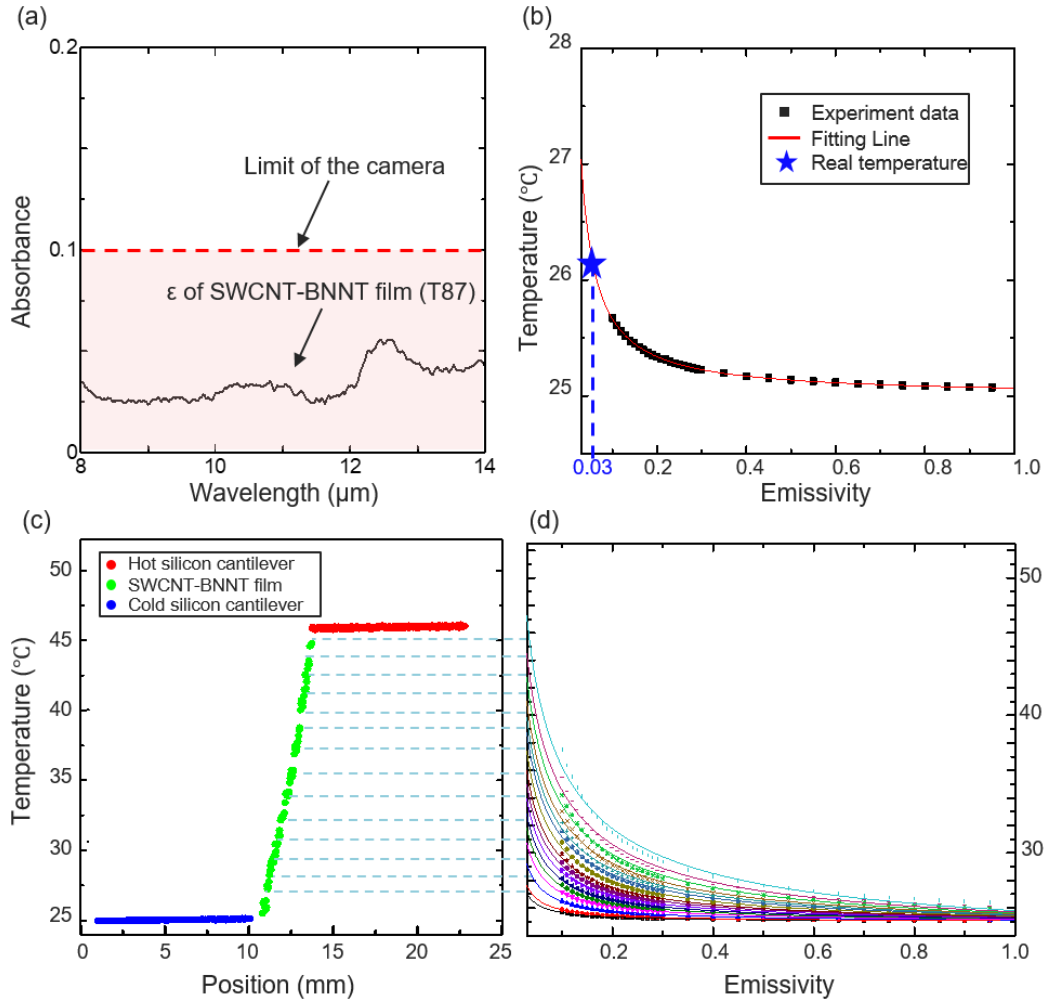


Figure 4-7. (a) Absorbance of a sample film measured by FT-IR. Red dashed line is the lower limit of the IR camera. Real emissivity of the sample is out of the range of the IR camera. (b) Measured data (black square) plotted together with a fitting line (red line). Blue dashed line and star denote the temperature of the sample under investigation at emissivity measured in (a). (c) Temperature distribution of a sample along the heat transport path decided by fitting lines in (d). (d) Fitting lines of some points chosen on a sample.

4.3.3 UNCERTAINTY ANALYSIS

According to the sheet thermal conductance of SWCNT-BNNT films determined by the equation (3-1), uncertainty of the experiment originates from the following parts: temperature profiles of silicon cantilevers with and without SWCNT-BNNT film samples, temperature

profiles of samples, and the width of SWCNT-BNNT film samples. Based on the above, Sheet thermal conductance can be simplified as the following equation:

$$\lambda_{\text{film}} \cdot t_{\text{film}} = \frac{\lambda_{\text{silicon}} \times \left[\left(\frac{dT}{dx} \right)_{\text{swi}} - \left(\frac{dT}{dx} \right)_{\text{swo}} \right] \cdot t_{\text{silicon}} \cdot W_{\text{silicon}}}{\left(\frac{\Delta T}{\Delta x} \right)_{\text{film}} \cdot W_{\text{film}}} = \frac{B \cdot \left[\left(\frac{dT}{dx} \right)_{\text{swi}} - \left(\frac{dT}{dx} \right)_{\text{swo}} \right]}{\left(\frac{\Delta T}{\Delta x} \right)_{\text{film}} \cdot W_{\text{film}}} \quad (4-1)$$

where B is a constant and $B = \lambda_{\text{silicon}} \cdot t_{\text{silicon}} \cdot W_{\text{silicon}}$.

Therefore, the uncertainty of each measured value can be converted into the total random uncertainty of the sheet thermal conductance by the following equation, where σ is uncertainty:

$$\begin{aligned} \sigma_{\text{total}} &= \left\{ \left[\frac{\partial(\lambda_{\text{film}} \cdot t_{\text{film}})}{\partial \left(\frac{dT}{dx} \right)_{\text{swi}}} \right]^2 \cdot \sigma^2 \left[\left(\frac{dT}{dx} \right)_{\text{swi}} \right] + \left[\frac{\partial(\lambda_{\text{film}} \cdot t_{\text{film}})}{\partial \left(\frac{dT}{dx} \right)_{\text{swo}}} \right]^2 \cdot \sigma^2 \left[\left(\frac{dT}{dx} \right)_{\text{swo}} \right] + \left[\frac{\partial(\lambda_{\text{film}} \cdot t_{\text{film}})}{\partial \left(\frac{\Delta T}{\Delta x} \right)_{\text{film}}} \right]^2 \cdot \sigma^2 \left[\left(\frac{\Delta T}{\Delta x} \right)_{\text{film}} \right] + \right. \\ &\quad \left. \left[\frac{\partial(\lambda_{\text{film}} \cdot t_{\text{film}})}{\partial (W_{\text{film}})} \right]^2 \cdot \sigma^2 [W_{\text{film}}] \right\}^{\frac{1}{2}} \\ &= \left\{ \frac{B^2}{\left[\left(\frac{dT}{dx} \right)_{\text{film}} \cdot W_{\text{film}} \right]^2} \cdot \left[\sigma^2 \left[\left(\frac{dT}{dx} \right)_{\text{swi}} \right] + \sigma^2 \left[\left(\frac{dT}{dx} \right)_{\text{swo}} \right] \right] + [B^2 \cdot \left[\left(\frac{dT}{dx} \right)_{\text{swi}} - \left(\frac{dT}{dx} \right)_{\text{swo}} \right]^2] \cdot \left[\frac{\sigma^2 \left[\left(\frac{dT}{dx} \right)_{\text{film}} \right]}{\left(\frac{dT}{dx} \right)_{\text{film}}^2 \cdot W_{\text{film}}} + \right. \right. \\ &\quad \left. \left. \frac{\sigma^2 [W_{\text{film}}]}{\left(\frac{dT}{dx} \right)_{\text{film}} \cdot W_{\text{film}}^2} \right] \right\}^{\frac{1}{2}} \quad (4-2) \end{aligned}$$

The four parts of the total uncertainty are composed of temperature profiles of silicon cantilevers with and without SWCNT-BNNT film samples, temperature profiles of samples, and the width of SWCNT-BNNT film samples. Table 4-1 lists the uncertainties for T87 SWCNT film, BNNT-SWCNT film and annealed film.

Table 4-1. Calculated uncertainty analysis for T87 SWCNT film, SWCNT-BNNT film and annealed SWCNT film.

T87 film	σ_{total} ($\mu\text{W} \cdot \text{K}^{-1}$)	parameter	$(dT/dx)_{\text{swi}}$ ($10^{-3} \times \text{K} \cdot \text{mm}^{-1}$)	$(dT/dx)_{\text{swo}}$ ($10^{-3} \times \text{K} \cdot \text{mm}^{-1}$)	$(\Delta T/\Delta x)_{\text{film}}$ ($\text{K} \cdot \text{mm}^{-1}$)	W_{film} (mm)
Bare	$3831.9 \pm$ 780.3	Input error	0.047 ± 0.001	0.044 ± 0.0005	15.1 ± 0.5	$2.04 \pm$ 0.12
		uncertainty	2 %	1 %	3 %	6 %

BNNT- wrapping	6410.2 ± 1064.9	Input error	0.049 ± 0.001	0.045 ± 0.0004	8.4 ± 0.07	2.86 ± 0.06
		uncertainty	2 %	1 %	1 %	2 %
Annealed	3549.9 ± 633.7	Input error	0.079 ± 0.001	0.07 ± 0.0008	51.4 ± 3.4	1.2 ± 0.08
		uncertainty	1 %	1%	6 %	6 %

From the table above, the largest part of uncertainty stems from the sample's temperature profile and the width of the sample. Although the SWCNT template used in this study is of high-quality, bundle and junctions are inevitable. This leads to a larger variation in the measured temperature point of the same x value, as shown in Figure 4-6. Thus, although the diffusive thermal transport is in existence in the sample film, the temperature profile is not completely smooth. On the other hand, the large uncertainty also stems from the geometrical dimension of the sample, the manual cut method is a major contribution to it. This problem may be settled through improving the sample preparation technique.

4.3.4 NOISES AND SENSITIVITY

The radiation heat transfer of this system is the main source of background thermal conductance, which can be approximated as:

$$G_{\text{Radiation}} = A_{\text{Heat-sink}} \cdot \sigma_B \cdot \varepsilon_{\text{Heater}} \cdot F_{12} \cdot (T_{\text{Heater}}^2 + T_{\text{Heat-sink}}^2) \cdot (T_{\text{Heater}} + T_{\text{Heat-sink}}) \quad (4-3)$$

where $A_{\text{Heat-sink}}$ is the cross-sectional area of the heat sink, σ_B is the Stefan-Boltzmann constant, $\varepsilon_{\text{Heater}}$ is the emissivity of the heater surface, which is about 0.2, and F_{12} is the view factor from the heater to the heat sink. According to the above known parameters, the calculated thermal conductance is on the order of $10^{-6} \text{ W}\cdot\text{K}^{-1}$. Considering the experimental results, this conductance cannot be ignored. Therefore, it's necessary to carry out a control experiment to eliminate it. In addition, the background thermal conductance involves the thermal radiation from the IR camera and the convection heat transfer caused by residual gas molecules. In order to measure the background thermal conductance, a pair of silicon cantilevers without

film samples and the one with a film sample as a reference were placed side by side.

4.4 EXPERIMENTAL RESULTS AND DISCUSSIONS

As illustrated in Figure 4-6, the heat transfer along the silicon-film-silicon is steady-state one-dimensional conduction, where the heat flux through the SWCNT-BNNT film and silicon cantilever satisfies the following equation:

$$Q_{\text{silicon}} = Q_{\text{film}} \quad (4-4)$$

where ‘silicon’ denotes the silicon cantilever and ‘film’ denotes the SWCNT-BNNT film.

By integrating Fourier’s law into equation (3-3), it is further simplified to:

$$\begin{aligned} \lambda_{\text{silicon}} \times \left[\left(\frac{dT}{dx} \right)_{\text{swi}} - \left(\frac{dT}{dx} \right)_{\text{swo}} \right] \cdot t_{\text{silicon}} \cdot W_{\text{silicon}} \\ = \lambda_{\text{film}} \cdot \left(\frac{\Delta T}{\Delta x} \right)_{\text{film}} \cdot t_{\text{film}} \cdot W_{\text{film}} \end{aligned} \quad (4-5)$$

In Eq. (4-5), λ , t , and W are the thermal conductivity, thickness and width of the material denoted in the subscript, respectively, while ‘swi’ and ‘swo’ indicate silicon with and without sample film, respectively. Because of the difficult in obtaining the thickness of the sample, we treat the product of thermal conductivity and film thickness as sheet thermal conductance and use this term in this research to describe the thermal transport property of different samples.

4.4.1 SHEET THERMAL CONDUCTANCE OF ANNEALED SWCNT FILM

The first step for CVD growth of BNNT is a heating step, and during this procedure, the suspended SWCNT template film first undergoes an annealing process at 1075°C for 1 h. When annealed, a common phenomenon for CNT films, arrays, fibers, and mats is that CNTs tend to approach each other and form bundles, and the number of intertube contacts increases considerably. [6, 117-119] This contact is believed to dramatically decrease thermal conductance and lead to phonon scattering. [20, 120] To check the influence of the annealing procedure on the SWCNT film, the sheet thermal conductance of bare SWCNT films and annealed films were

compared. First, the sheet thermal conductance of the bare SWCNT film was measured, and the result is plotted by black circles in Figure 4-8. Then, annealed SWCNT samples were prepared by subjecting the SWCNT film to the same CVD method without ammonia borane, followed by the thermal conductance measurement. The result is plotted together with the result of the bare SWCNT film. As shown in Figure 4-8, for bare films, the sheet thermal conductance decreases as transparency increases, which is due to the decrease in the number of heat conduction paths (the number of SWCNTs) at high transparency, and the trend is consistent with previous research. [114, 121] For all samples measured, the sheet thermal conductance shows decrease after annealing (orange triangle) compared with that of samples without treatment. The annealed sample of T92 films became too thin to perform dry transfer after annealing, so the value was not obtained. From the trend reflected by the other four samples, it is reasonable to speculate that the sheet thermal conductance of the T92 film also decreases compared with the original value. It is important to know what the changes in the templates are caused by the experimental procedure before BNNT growth, which is helpful to correctly discuss the role that BNNT plays in the heterostructured film.

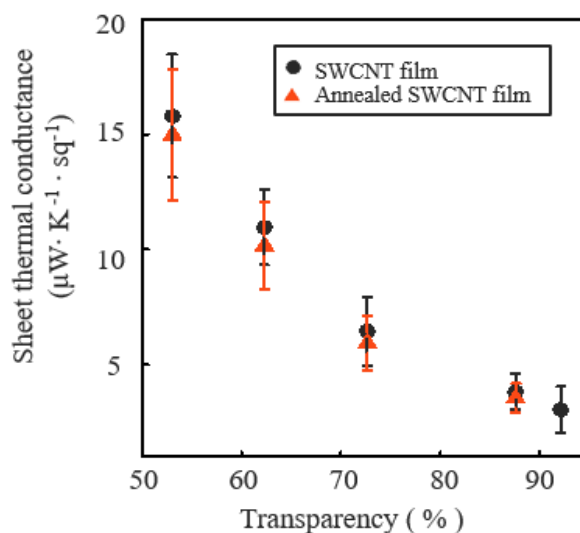


Fig 4-8. Sheet thermal conductance of bare SWCNT films (black circle) and SWCNT films after annealing (orange triangle). A decrease is observed for all four samples measured after annealing.

4.4.2 SHEET THERMAL CONDUCTANCE OF SWCNT-BNNT FILM

The sheet thermal conductance values of SWCNT-BNNT films are plotted against the transparency as shown in Figure 4-9 together with the result of the annealed SWCNT films. For all samples, the sheet thermal conductance shows a clear enhancement after BNNT wrapping. This enhancement is attributed to the thermally conductive BNNTs[122-125] that coat the SWCNT film and act as additional thermal transport channels. The degree of increase is different for the samples measured and is plotted with blue hollow rhombuses in Figure 4-9. The sample with higher transparency shows a larger increase compared with the thicker ones with lower transparency. The least amount of change was observed in the T53 film, with only ~24 % improvement. For the T87 transparent sample, an ~80 % increase is achieved. Note that, along with sheet thermal conductance, thermal conductivity of SWCNT-BNNT films is also enhanced because the film thickness is assumed to be barely unchanged by BNNT growth. The increase in the sheet thermal conductance of the T92 film after BNNT wrapping is approximately 93 % compared with that of the bare SWCNT film before annealing. As stated in the last section, it is reasonable to predict an even larger increase if the sheet thermal conductance of the annealed T92 film could be measured. These varied increases could be explained from the following two perspectives. Because the original sheet thermal conductance of the low-transparency SWCNT film is relatively high, the contribution from additional heat-conducting channels offered by BNNTs becomes less prominent than in the other samples. The other explanation is the diameter of the BNNTs. For the T92 film, the density of SWCNTs is low, so bundles are formed with small diameters and are loosely packed with each other. Therefore, the diameter of BNNTs is also relatively small. However, the bundle size in the T53 film is larger than in the other samples, and the bundles are tightly packed, leading to a larger BNNT size. For 1D structures such as CNTs, the diameter has a reverse relationship with thermal conductance; that is, the smaller the diameter is, the higher the heat transport ability.[126] Consequently, the contribution from large-diameter BNNTs has a limited improvement in the overall performance for thick SWCNT films.

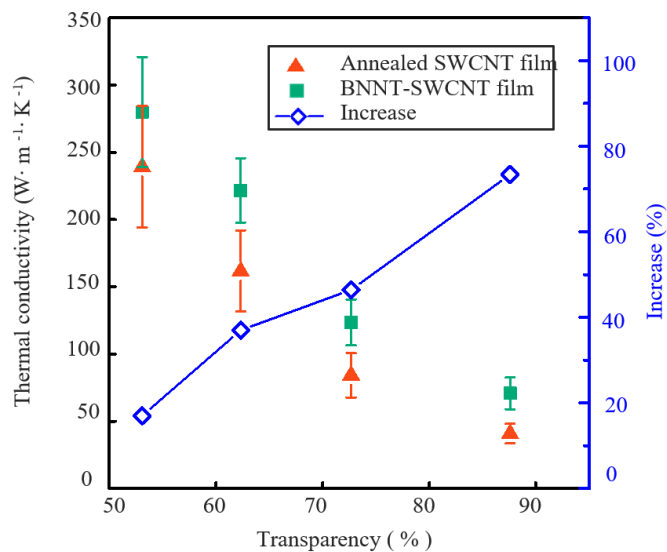


FIG 4-9. Sheet thermal conductance (left axis) of BN-SWCNT films (mint square) and annealed SWCNT films (orange triangle). The blue hollow rhombus shows the increase ratio of the sheet thermal conductance after BN wrapping (blue hollow rhombus, right axis).

Since the SWCNT-BNNT films are thin and soft, measuring their thickness is challenging. Owing to the loosely packed manner of the SWCNT film template, the BNNT wrapping SWCNT inside the film barely affects the total thickness. Increase of thickness mainly comes from two surfaces of the heterostructured films. In a previous study, thickness of SWCNT films used in this study have been measured by an optical profiler.⁷ The thermal conductivity of the SWCNT-BNNT films was estimated based on these thicknesses. The number of BNNT walls is about 2–10 in this study, and in this case, we take an average value of 5. Because the distance between walls is 0.36 nm, the additional thickness from BNNTs was determined as 3.6 nm.

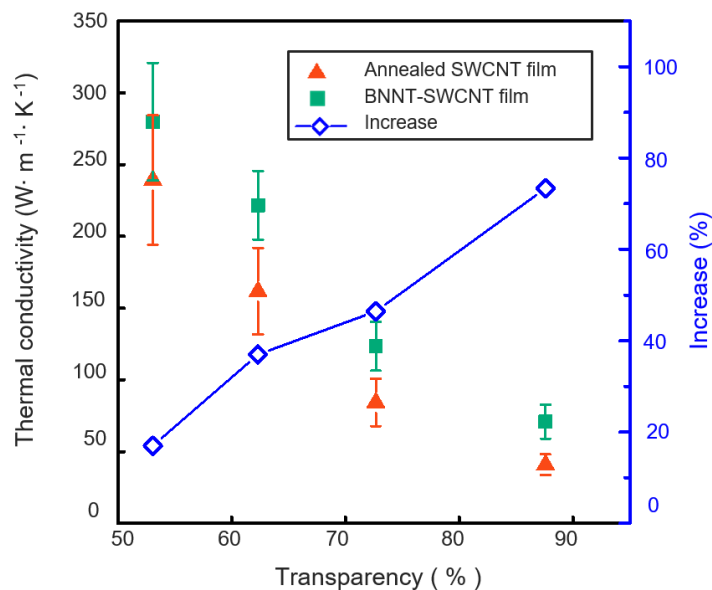


FIG 4-10. Estimated thermal conductivity of annealed SWCNT films, SWCNT-BNNT films and the increase.

4.4.3 THERMAL TRANSPORT MODEL OF SWCNT-BNNT FILM

Thermal transport in this SWCNT-BNNT system is strongly influenced by its structure. A representative structural description is proposed in Figure 4-11. Two key components of the heterostructured film are enlarged to provide detailed information. Here, (I) is the isolated SWCNT wrapped by single-layer BNNT, and (II) is a junction of the template film coated by BN. Instead of separating the SWCNTs at the junction, BN forms a shell that wraps the junction and then extends along the SWCNTs and SWCNT bundles. From the morphology illustrated here, it is clear and reasonable to treat this heterostructured film as an inner SWCNT film and an outer BNNT network connected in parallel with each other.

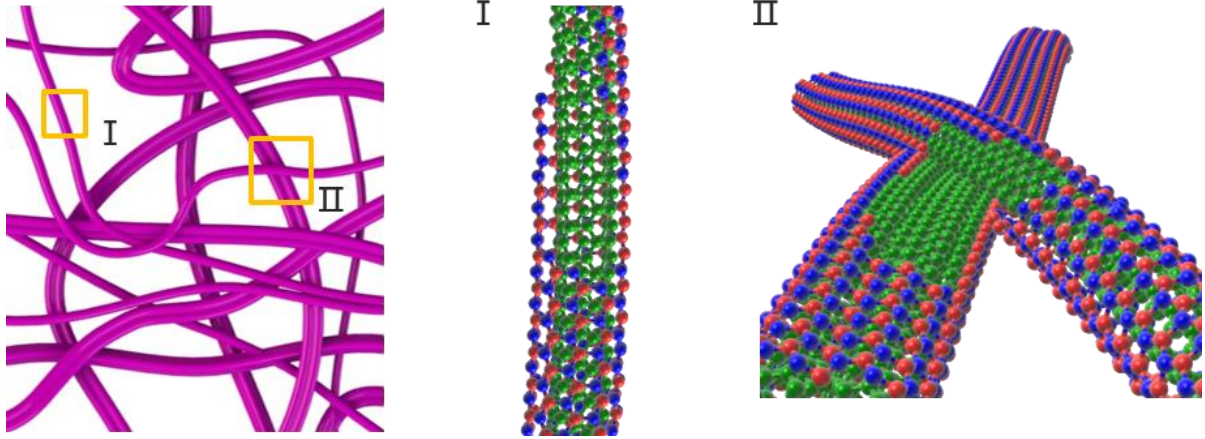


FIG 4-11. The typical network structure of the SWCNT-BNNT heterostructured film. Two representative segments of the heterostructured film indicated by I and II are enlarged for better observation of the outer and inner structure. In the enlarged images, BNNTs are partially omitted for clarity of the structure of inner SWCNTs. (I) A single-layer BNNT coating on an isolated SWCNT. (II) The BNNT formed at the SWCNT junction wraps the whole junction instead of separating the upper SWCNT from the lower SWCNT bundle.

To further discuss the thermal transport mechanism of the heterostructured film, a concise thermal resistance model was proposed, in which the interaction between the BNNT and the inner SWCNT can be ignored, as the van der Waals force is very weak.[103] Therefore, the thermal resistance of the SWCNT film and the SWCNT-BNNT film could be separated into two parts:

$$R_{\text{SWCNT film}} = R_{\text{junction}} + R_{\text{SWCNT}} \quad (4-6)$$

and
$$R_{\text{BNNT-SWCNT film}} = R_{\text{junction}} + R_{\text{SWCNT//BNNT}} \quad (4-7)$$

where R_{junction} is the thermal resistance caused by the contacts between SWCNTs in the film (Figure 4-11 (II)), R_{SWCNT} and $R_{\text{SWCNT//BNNT}}$ are the intrinsic thermal resistance of SWCNTs and the resistance of isolated SWCNTs and BNNT connected in parallel (Figure 4-11 (I)), respectively. Between these two resistances, R_{junction} is the major parameter that influences the total performance of a random network. [127] For very thin films, such as T92 and T87, the contact density is low, meaning that R_{junction} is small. Freely suspended SWCNTs

between junctions are relatively long and form bundles with small diameters. BNNTs grown on these suspended SWCNs are also long and small in diameter. With the intrinsic high thermal conductivity of SWCNTs and BNNTs, a distinct enhancement of over 80 % is observed for T87. In contrast, the high contact density of thicker template films led to larger values of R_{junction} , and the SWCNTs could only freely suspend between neighboring contacts. Additional layers of the BNNT coating reduces $R_{\text{SWCNT//BNNT}}$, but the minor proportion of this addition does not readily reduce the total thermal resistance; hence, the enhancement after BNNT wrapping is not obvious. In addition, high-temperature annealing during the CVD process creates more contacts in thicker SWCNT films than in thinner films and causes an even higher R_{junction} . This can be observed clearly from Figure 4-8, where the drop in thermal conductance in the thicker film is evidently larger than in the thin films after annealing. Based on this situation, although the BNNT coating on SWCNTs in parallel decreases $R_{\text{SWCNT//BNNT}}$, the major contribution to the thermal resistance comes from the intertube contact R_{junction} , which cannot be lowered by the BNNT coating and even increases during the high-temperature process. Therefore, the sheet thermal conductance enhancement of samples with low transparency cannot reach that of samples with high transparency.

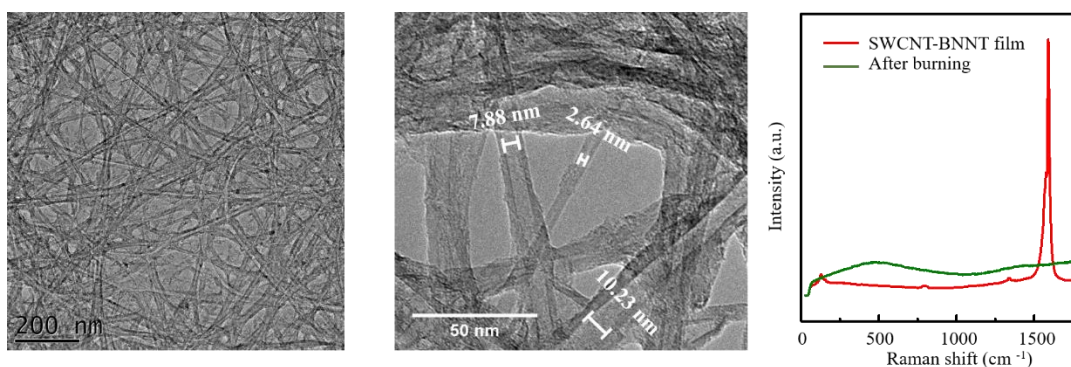


FIG 4-12. TEM of BNNT film after annealing in air for 3 hours. Raman spectra of TT53 SWCNT-BNNT film before and after annealing.

It is possible to observe the real structure of BNNT coated outside by removing inner SWCNT at high temperature in air. As shown in Figure 4-12, TEM observation is taken after annealing SWCNT-BNNT film in air at 600 °C for 3 hours. There's no G band observed, indicating a complete remove of SWCNT. However, after annealing for 1 hour, the samples fall into pieces, so there's no way to measure the BNNT film individually.

4.4.4 ELECTRICAL CONDUCTANCE OF SWCNT-BNNT FILM

In this study, the SWCNT film are highly conductive. However, the boron nitride is insulation material. The sheet electrical of SWCNT film samples and SWCNT-BNNT samples in this reaserch were measured by 4-point probe method after every experimental step. Besides, the Raman peak shift can also reflect the change of elctron in samples. Therefore, the electrical property of the samples are discussed on basis of sheet electrical conductance and Raman spectra.

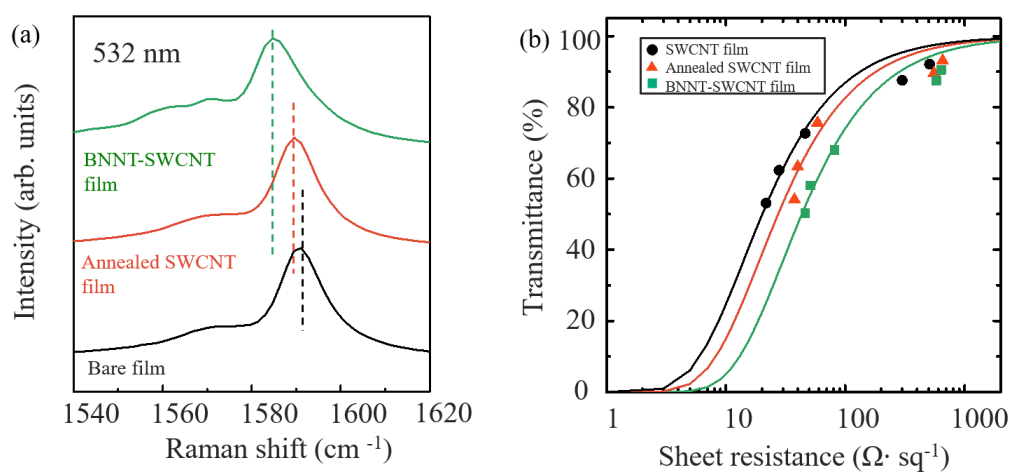


FIG 4-13. (a) Raman spectra of bare SWCNT film, annealed SWCNT film, and SWCNT-BNNT film. The dashed lines show the positions of G-band. All Raman spectra were normalized by the G-band intensity. (b) Sheet resistance versus optical transparency (at 550 nm) of bare SWCNT films, annealed SWCNT films, and SWCNT-BNNT films. Solid lines shown are the approximated fitting curves.

SWCNT films are naturally *p*-doped by oxygen or other molecules adsorbed on the

film.[128, 129] During the vacuum annealing process, the adsorbed molecules are removed, and the film is purified. Consequently, the film is de-doped after annealing. This de-doping denotes an obvious change in electron density, as shown in the Raman spectra in Figure 4-13 (a). The peak positions of the G-band were slightly downshifted for the annealed SWCNT film and the SWCNT-BNNT film. SWCNT film in air is naturally *p*-doped, and the downshift indicates the removal of molecules adsorbed on the SWCNT film surface due to annealing in vacuum. This change is consistent with a previous study.[130] The further downshift of G-band for the SWCNT-BNNT film was attributed to thermal strain of SWCNTs induced by BNNTs [38] in addition to de-doping. The de-doping leads to an obvious change in electrical conductivity of the film. Additionally, partial etching of SWCNTs is expected during BNNT growth because of high temperature and the presence of hydrogen and residual molecules in the reaction environment. Both the de-doping and partial etching of SWCNTs can cause the change in electrical conductivity.

According to an earlier study,[130] the transmittance of thin films and their sheet resistance have the relationship as follows:

$$R_s = \frac{\varepsilon\rho}{en\mu \ln(T(\lambda))} \quad (4-8)$$

where R_s is sheet resistance, ε is a wavelength-dependent extinction coefficient, ρ is density, e is the elementary charge, n is the charge-carrier concentration, μ is the mobility, and $T(\lambda)$ is the wavelength-dependent transmittance. The measured sheet resistance of the bare SWCNT films, the annealed SWCNT films, and the SWCNT-BNNT films were plotted in Figure 4-13 (b) with fitting lines based on the equation above.

4.4.5 SEEBECK COEFFICIENT OF SWCNT-BNNT FILM

As discussed in last part, the electron density in the samples are changed by the high temperature annealing during CVD process. The Seebeck coefficient of the samples are room temperature is measured for more information of SWCNT-BNNT film. Seebeck coefficient is an important parameter for evaluating SWCNT-BNNT heterostructure material and its future application as thermal or thermoelectrical material.

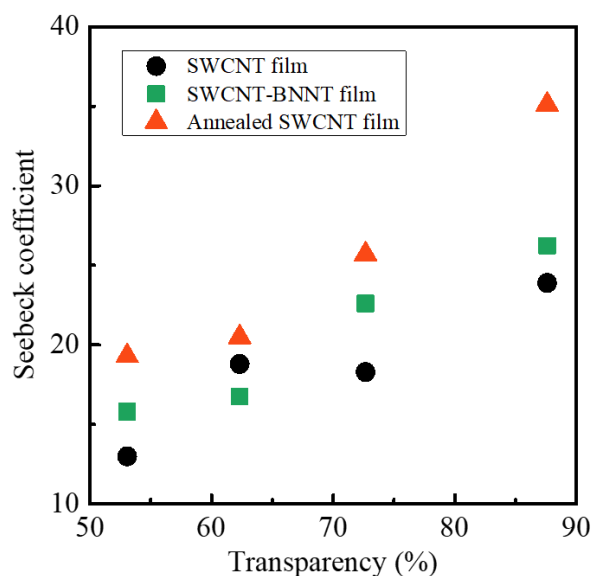


FIG 4-14. Seebeck coefficient of SWCNT film, annealed SWCNT film and SWCNT-BNNT film at room temperature.

In Figure 4-14, for all types of samples, after annealing, the Seebeck coefficient became larger, indicating a decrease in charge carrier density, which is consistent with previous discussion on sheet electrical conductance.

4.5 MODELING STUDY OF FILM THERMAL PROPERTY

Numerous experiments analysis has been conducted by several groups to study the electrical and thermal transport mechanism in CNT assemblies. They have found that the properties are highly structure sensitive. To further reveal the transport mechanism in such materials, theoretical studies have been put forward and some models have been brought about. Among these models, some focused on single parameter like intertube contact density, pressure, and angle, while others attempted to offer a more general description of the CNT assemble as a whole system. Models that combine the thermal property of individual nanotube and volume fraction are relatively simple but it is difficult for them to take full consideration of morphology effect like entanglement and CNT-CNT contact. This is the reason that the experiment results

often fall far behind of that predicted by the model. Mesoscopic or hierarchical models overcome the problems mentioned above and provide a more accurate description. However, the calculation is kind of heavy given all the factors needed.

In this part, a quick and manageable model is put forward to give a quick estimation of thermal transport property of SWCNT film. This model is also extensible to take heterostructure into account.

4.5.1 RANDOM STICK NETWORK OF SWCNT FILM

In Chapter 3, a bundle model containing important factors like length, temperature and size have been given, which is also quite useful in this part. The film could be seen as a random network consisted by bundles. Therefore, we use a random stick network (RSN) model, where bundles are simplified to straight sticks to investigate the thermal transport property of SWCNT film. The transport of phonons in bundles is not influenced by whether it is straight or curved.

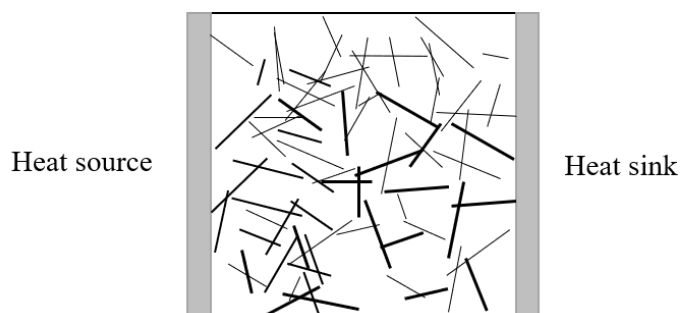


FIG 4-15. A schematic illustration of a SWCNT thin film showing the RSN model. Different width of the stick represents different bundle size.

The model is shown in Figure 4-15. The two gray blocks are heat source and heat sink, and in between is the SWCNT film. The black sticks are bundles with different lengths and sizes. As the film is synthesized by floating catalyst CVD (FCCVD) in our study, the bundles are not aligned therefore the angles between the bundles are random. Some assumptions should be made to simplify the RSN model. The first is that for each bundle, only the two contacts at the two ends are considered. This assumption is reasonable because phonon mean free path could be

micrometer long and they can easily travel from one end to the other without bifurcation. These transport paths with least number of junctions are the most important channels for thermal transport. On the other hand, the neighboring junctions have negligible influence on each other, hence ignoring the contact at intervals is acceptable for this model.

The basic component of this film is bundle and junction. Instead of treating the network as a system, we focus on each thermal transport paths in this system. As shown in Figure 4-16, four bundles are connecting in series and forming a channel from left to right. The four bundles are denoted by a number follow capitalized B, where B means bundle and number is the size. In real samples, it is difficult to tell the exact value of bundle size, instead we use bundle diameter, d , to estimate the bundle size. The junctions are symbolized by letter C and the number following it is used to distinguish the different junctions. Length of the bundle between two junctions is l . The contact resistance is determined by the contact conductance and the contact area. Definition of contact area is a complicated question and here we will use the overlapped area at the junction of two bundles. To determine the contact area, the angle formed by two bundles at the junction is necessary, we'll talk about this in next part.

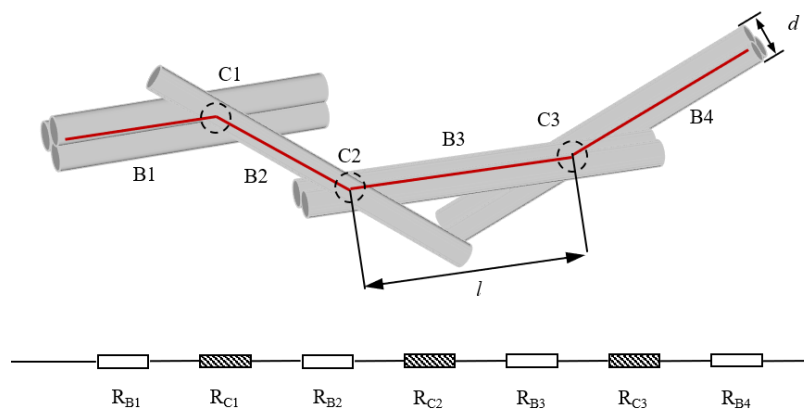


FIG 4-16. A schematic illustration of a conducting path along which heat current can flow from B1 to B4 through B2 and B3. The contact parts between bundles are marked by C1,C2 and C3. Diameter of bundle is defined as d . Lower part of the figure is the equivalent circuit model for this path, including R_B as bundle thermal resistance and R_C as contact resistance.

4.5.2 KEY PARAMETERS ANALYSIS

As shown in last part, every path in the network is consisted by bundles and junctions. To get the thermal resistance of a bundle, we use the model in Chapter 3, and the temperature is set to room temperature. Instead of number of SWCNT in a bundle, diameter is used to give a rough estimation of the bundle size and each bundle is assumed to be fully packed (cross section is hexagonal). In this way, a bundle with diameter d will have $(3/16 * d^2 + 0.25)$ SWCNTs. Thermal resistance of bundle with diameter d and length l is written as:

$$\kappa_{bu}(d, l) = \frac{\kappa_{is}(300, l)}{1 + A(300) * \varphi(3/16 * d^2 + 0.25)^4} \quad (4-9)$$

SWCNT bundles in the film is long and varying in bundle size, and it is important to have get some information about the length and diameter distribution about films with different transparencies. Take T87 as an example, diameter of 100 bundles are measured and the histogram is shown in Figure 4-17 fitted by lognormal distribution. $D \sim L(2.29, 0.29^2)$, which means the diameter's expected value is 9.87 nm.

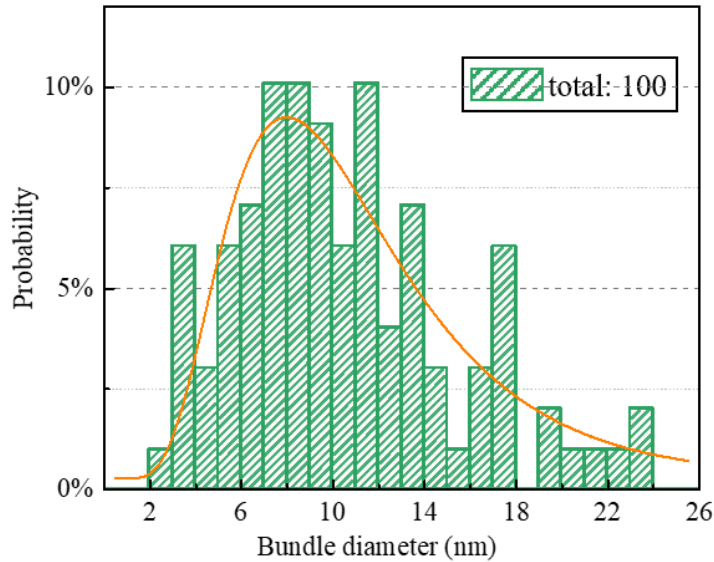


FIG 4-17. Histogram of measured diameters of 100 bundles in T87 film. The orange line is a lognormal probability density function. The mean of lognormal distribution is 2.29 nm, therefore the mean diameter of bundle in T87 is around 9.78 nm.

As shown in Figure 4-4, the bundles in the film is very long and no free ends could be

observed by TEM. The statistics in papers from Prof. Kauppinen's group give some information about the length distribution of the bundle length synthesized by FCCVD method [106, 131].

Another factor in RSN model is the angle formed by two connecting bundles. Same as bundle size, we measured 100 angles in T87 film and the histogram of the angles are plotted in Figure 4-18. Distribution of the angle is a normal distribution which is centered at around 90 degree. Despite the symmetry distribution, small angles is more popular than large angles. That is because two bundles forming an angle are not always straight at the junction, so the angle is gauged by the two tangent lines of the bundles.

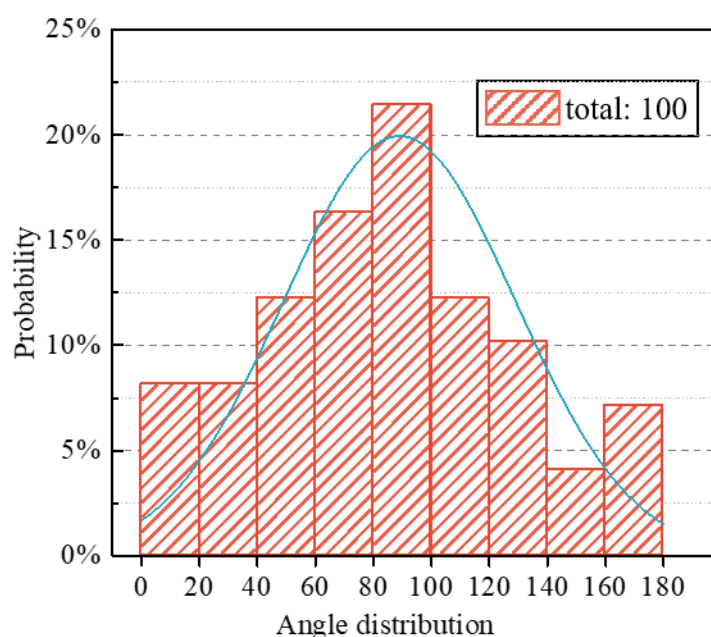


FIG 4-18. Histogram of measured 100 crossing angle formed by bundles in T87 film. The blue line is a normal distribution. The mean of lognormal distribution is 89 degree.

4.5.3 QUANTITATIVE STUDY OF DIAMETER AND LENGTH DEPENDENT THERMAL CONDUCTIVITY OF SWCNT FILM

According to the reported works from Prof. Kauppinen's group [106, 131], average length of bundle is chosen as 10 μm and the sample size is assumed to be 100 $\mu\text{m} \times 100 \mu\text{m}$. Thermal paths in this system conduct heat from one side to the other of the sample and the bundles in each path contact end to end in series. Surely there are contacts between two ends of the bundle, but compared with the highway, which is the bundle itself, the paths formed by very

short segments offer minor contribution to the total thermal conductance. Here, some constraints are listed in our model:

- (1) Each bundle is straight and contact with each other end to end;
- (2) Angle formed by adjacent bundles obey the distribution mentioned earlier;
- (3) Diameter of the bundles obey the distribution mentioned earlier;
- (4) The first bundle has a random angle relative to the horizontal direction.

One important parameter in CNT assemble is the contact conductance. theoretical analysis, MD simulation together with experiment study haven been conducted to uncover this. Despite the different conditions and carbon nanotube chirality, one very tricky parameter is the contact area [132]. The difference definition of contact area is ignored, and the contact conductance as a function of contact area is plotted in Figure 4-19[20, 120, 132-138]. It should be mentioned that in Ref, they use thermal boundary resistance but not conductance per area. The contact area is calculated by consuming the contact area is the production of length and tube diameter, which is the same as in this study. The MD simulation result for S. Maruyama et al and Zhigilei et al. have larger contact area compared with others, because the way of area calculation. The CNT in the two MD simulation are (5,5) and (10,10), diameter are comparable to that in other papers. So despite for the large difference in contact area, the contact conductance are similar to others.

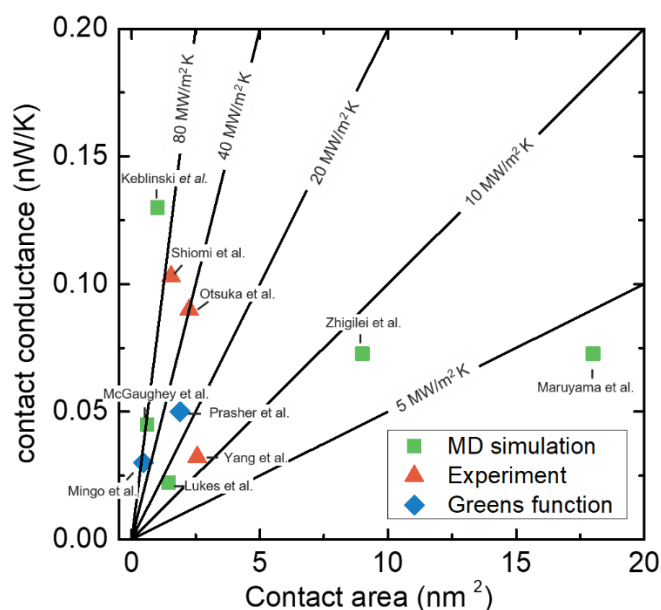


FIG 4-19. Summary of the contact conductance from previous studies. The five lines are contact conductance per area equals to 5, 10, 20, 40, and 80 MW/ m²K.

With the four constrains and contact conductance of 40 MW/ m²K, 1000 paths have been generated randomly and the number of junctions in each path N_j , distribution of bundle conductance consisting the bundle G_s and junction conductance G_j are counted and plotted in Figure 4-20. The distributions are $N_j \sim N(12.5, 1.8^2)$, $G_s \sim N(0.7, 0.04^2)$ and $G_j \sim N(0.78, 0.039^2)$, respectively, where N denotes normal distribution. The average path conductance could be estimated as:

$$G_p = \left((N + 1) * \frac{1}{G_b} + N * \frac{1}{G_j} \right)^{-1}$$

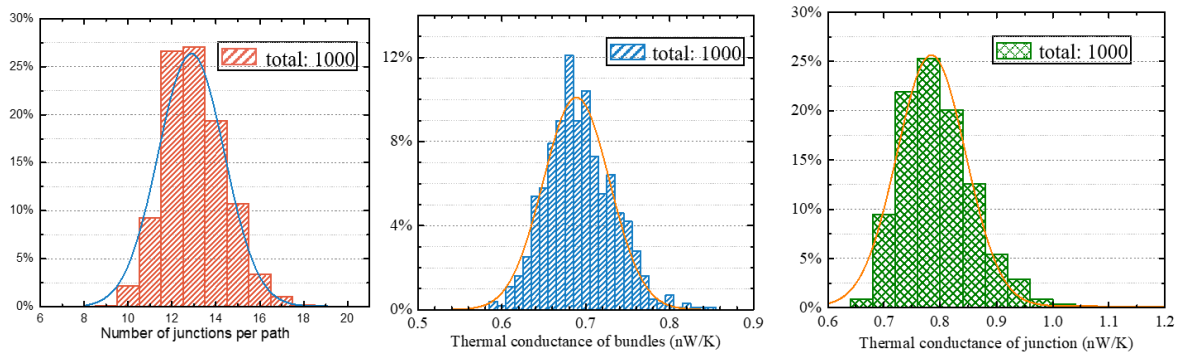


FIG 4-20. Histogram of number of junction, bundle conductance and junction conductance from 1000 randomly generated paths for 100 μm sample. The average value for number of junction, thermal conductance of bundle and thermal conductance of junction are: 12, 0.7 nW/K and 0.78 nW/K respectively.

Paths with 100 μm consisted of randomly generated bundles are simulated and the distribution of 1000 such paths are shown in Figure 4-21. The average of the thermal conductance per path is 0.027 nW/K. However, for a analytic model, distribution is not always ready to use. Therefore, the average of junction, bundle conductance and junction conductance are used to give an evaluation of the path conductance as follows:

$$G_p = \left((N + 1) \times \frac{1}{G_b} + N \times \frac{1}{G_j} \right)^{-1} \quad (4-10)$$

With the average value for $N = 13$, $G_b = 0.7 \text{ nW/K}$, $G_j = 0.78 \text{ nW/K}$, G_p is calculated to be 0.027, very close to the distribution. So in the following discussion, we're going to use the average value of bundle conductance, junction conductance and the junction number is fixed to 14 for further discussion.

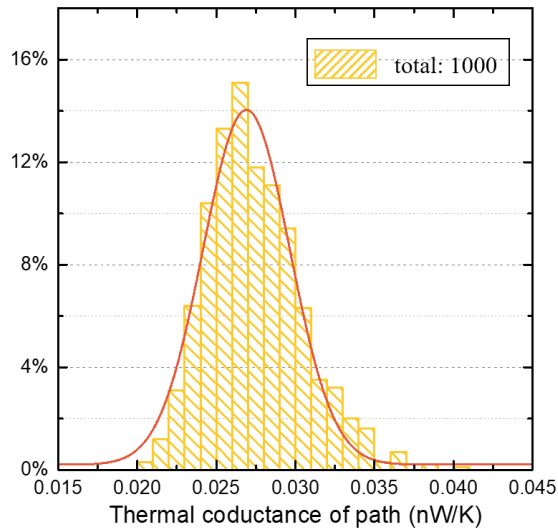


FIG 4-21. Histogram of 1000 randomly generated paths with length of 100 μm . The average value of path conductance is 0.0115nW/K.

For the length dependency, different bundle lengths with the same diameter distribution is simulated and the total thermal conductance of path is 100 μm long. The path conductance is plotted as a function of bundle length. Different contact conductance are included in Figure 4-22. From the figure, path conductance is in a positive relationship with bundle length for all four contact conductance. At larger bundle length, the difference between four lines are becoming smaller, indicating that the contact part has less and less influence on the path conductance, and the major part is the bundle consisting the path. That means contact conductance is important only for system with short bundles. For sample with certain length, longer bundle means less junctions are needed and therefore the loss comes from intertube thermal resistance is limited. The upper boundary for the path thermal conductance is when the percentage of bundle resistance reaches 100 %, which means the bundles are long enough to cover the range of the

sample and no intertube thermal transport is needed. The bundles will act as highways for heat transfer and the thermal conductance will also be the largest. Besides the paths consists of very long bundles, the ones that consisting of many small segments and intertube junction also exist in large number, but these paths are too weak to be ignored. Figure 4-22 (b) shows the percentage of bundle resistance with different bundle length. For very short bundles, most of the resistance are originated from junction. That is, system consisted by short bundles are junction-domain. Change of the contact conductance per area will not make any difference. When the bundle is longer, it starts to become major part for the entire path.

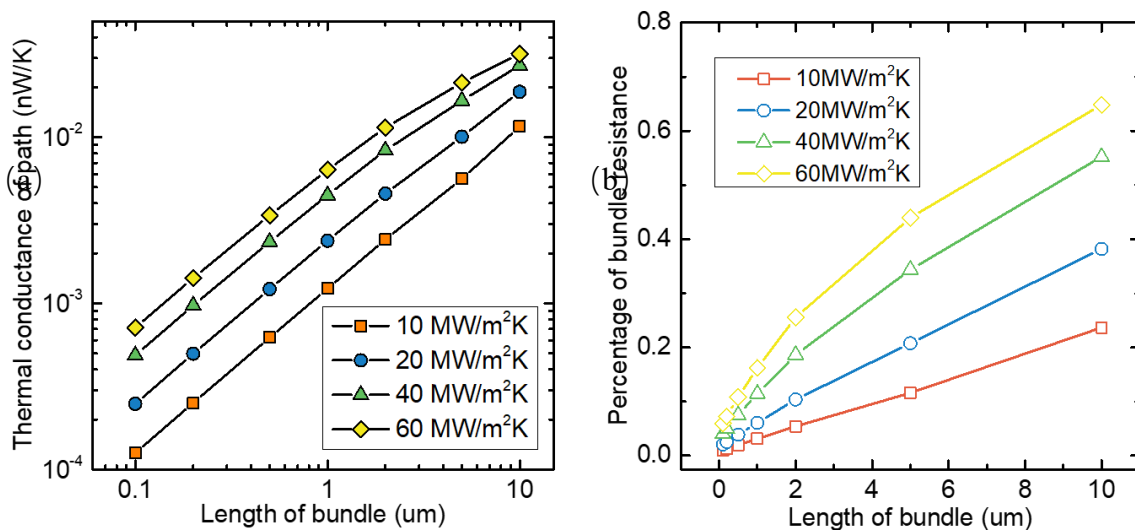


FIG 4-22. Path thermal conductance and percentage of bundle resistance plotted against length of bundle.

The orange histogram is the thermal conductance per 10 μm path, and the blue triangle is the percentage of bundle resistance in the path.

Next is the diameter dependent of the path thermal conductance is studied. Before go into the path conductance, bundle conductance with vary diameter or bundle size should be clarified. For a common sense, large bundle has more CNT and therefore has larger thermal conductance. With the bundle model defined in last chapter, thermal conductance of bundle is plotted as a function of bundle size and plotted in Figure 4-23 (a). Different from the common understanding, bundle conductance is not monotonously increasing with bundle size. It has a minimum value at around bundle size of 11, after which the bundle thermal conductance will keep increasing with bundle size. This new finding is very important for explaining experimental

studies conducted on CNT films. Then the thermal conductance for path consisted by 10 μm and 5 μm bundles with area contact conductance from 10 $\text{MW}/\text{m}^2\text{K}$ to 100 $\text{MW}/\text{m}^2\text{K}$ has been simulated and plotted in Figure 4-23 (b). The bundle diameters are chosen to be 5 nm, 10 nm, and 20 nm. 10 nm is the average bundle diameter in T87. Consists with 4-23 (a), the largest path conductance is achieved when bundle diameter is 20 nm. Path conductance for 5 nm bundles is larger than bundle diameter of 10 nm.

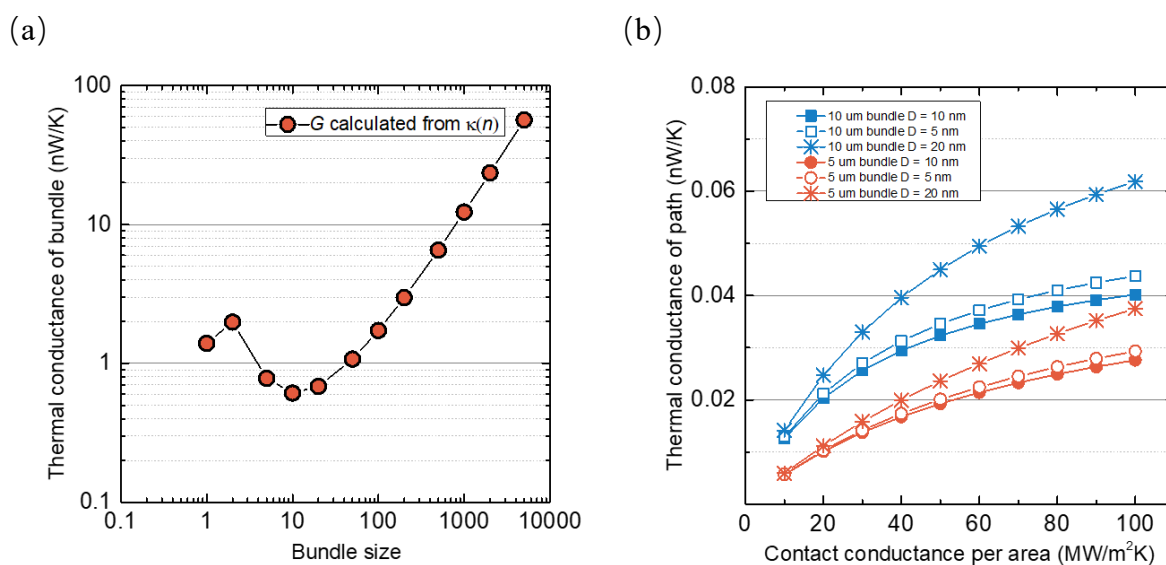


FIG 4-23. (a) is the thermal conductance of bundle with changing bundle size and (b) is the thermal conductance with different conductance per area. In (b), the bundle diameter is also changed to 5 nm and 20 nm, denoted by hollo square and snow symbol, respectively.

4.5.4 QUANTITATIVE ANALYSIS OF THERMAL TRANSPORT PROPERTY OF FILM

In this research, thermal transport property is described by sheet thermal conductance. Sheet thermal conductance is the production of thermal conductivity and film thickness. Thin film thickness is generally of the order of a wavelength of light, and consider the rough and soft surface, acquiring the accurate film thickness is quite a challenging job. For a certain thin film, the measured thickness could vary according to method. This will lead to the uncertainty of thermal conductivity. Instead of thermal conductivity, sheet thermal conductance is a good

choice for describing thermal property. This concept is analogy to the sheet electrical conductance, and the value equals to thermal conductance when the film is a perfect square, that is width equals to length. When the number of paths in a square is decided, the sheet thermal conductance could be calculated and compare with the real sample.

The samples in this study are uniform SWCNT network and the area density is $\frac{N_{tube}}{L^2}$, where L is the size of sample. With an average bundle size of \bar{n}_b , the number of bundles N_b is roughly $\frac{N_{tube}}{\bar{n}_b}$. Here a new term is defined as line density, D_L , which is the number of bundles cross one line, as the vertical black line shown in Figure 4-24. Bundle i is generated randomly in this area with length and diameter obeying the distribution shown in previous part. If bundle i falls into the grey area, it will cross the black line. Therefore, the line density could be calculated as:

$$D_L = \sum_{i=1}^{N_b} \frac{l_i \cos \theta_i}{L} = \frac{\bar{l}}{L} \sum_{i=1}^{N_b} \cos \theta_i = \frac{\bar{l} N_b}{L \pi} \int_{-\frac{\pi}{2}}^{\frac{\pi}{2}} \cos \theta d\theta = \frac{2 \bar{l} N_b}{L \pi} \quad (4-11)$$

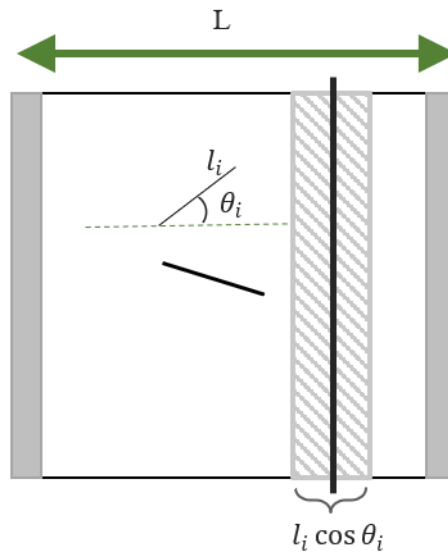


FIG 4-24. Schematic figure of the sample, bundle i and line. The grey square with size of $l_i \cos \theta_i$ is for calculate the possible of bundle i cross the black line.

The relationship between line density and tube density has been established. From TEM figure, the line density for T87 film is 38 tubes per μm . For other samples, absorbance is linearly related to the tube density and absorbance could be computed from transparency, T , through $A =$

$-\log_{10} T$. Therefore, for film with transparency T , the line density is:

$$D_L = \frac{-\log_{10} T}{-\log_{10} 0.87} \times 38L \quad (4-12)$$

where L is the sample length in micrometer. The calculated line density for T72, T62, T53 samples are 8963, 13044 and 17323 respectively.

Sheet thermal conductance is the production of number of path and path conductance. The bundles form mass junctions in the film and the number of path is beyond imagination. But only the paths with minimum junctions are considered because they contribute the most to the thermal transport. In this way, the number of path is directly related with the line density, which is the number of paths start from heat source. α is a factor that is changable.

$$G = N_P \cdot G_p = \alpha D_L G_p \quad (4-13)$$

The equation is fitted with experiment result and plotted in Figure 4-25 with blue line. The fitted $\alpha = 32$. This fitting line matches well with the experiment data, and give an accurate description of the trend.

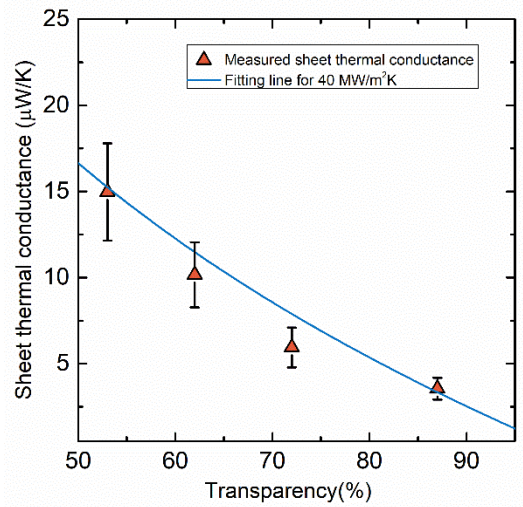


FIG 4-25. Sheet thermal conductance from experiment and fitting line of the model. red triangle are the experiment result and blue line is the fitting line with $\alpha=32$.

When adjusting the contact conductance per area, α will change accordingly. However, the fitting line will always be the same. The α fitted from contact conductance of 10, 20, 40, 60, 80 and 100 MW/m²K are plotted in Figure 4-26. For small contact conductance, α is larger to reach the measured sheet thermal conductance from experiment. But when contact

conductance is large, α is very stable, around 20. This is because when contact conductance is large enough, path conductance will be fully decided by bundle conductance, as shown in Figure 4-22 (b).

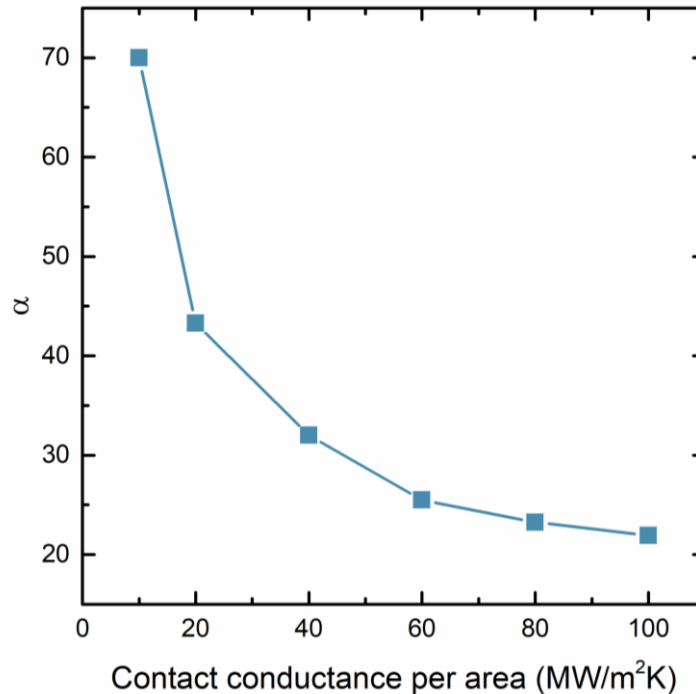


FIG 4-26. Fitted α with changing contact conductance per area.

Now an estimation of the sheet thermal conductance of SWCNT-BNNT film could be done based on the average model. Assume the contact conductance per area is 40 MW/m²K, and the BNNT has no interaction with the inner SWCNT bundle. Thermal conductance of BNNT is taken from Ref.122, where 30 - 40 nm diameter BNNT of 10 μ m long has thermal conductivity of around 200 W/m K. With the cross area defined as ring area, thermal conductance of the tube is about 0.64 nW/K. Consider the BNNT grown in CVD has two layers, path conductance is improved to 0.042 nW/K. Line density and α are same as in the average model and sheet thermal conductance is plotted in Figure 4-27 with green line①. The fitting line gives a similar value for T87, but for other samples, the fitting is not so good. The reason for this discrepancy is mainly from the BNNT conductance used here. When considering thermal transport paths, ignoring the intertube contacts at the middle of the bundle will not have very large effect. However, these junctions will split the BNNT grown outside into discrete parts, which is bad for phonon transport. That is, assume the same bundle conductance for samples with different

thickness is not proper, and will give a overestiamtion of the bundle conductane in thick film. As the diameter of BNNT in this experiment may not be so large as 30 nm, the chosen thermal conductivity of 200 W/mK maybe wrong. To give a more comprehensive description, thermal conductivity of 100 W/mK and 400 W/mK is also plotted and give a range denoted by grey lines in the figure.

To compare the inceasemet before and after BNNT growth, the fitted solid green line is is used and plotted with green dashed line. Different from the hollo blue diamond symbol, the model gives a uniform increasement for all sample. The reason is same as mentioned above, bundle conductaces for different transparency films are the same.

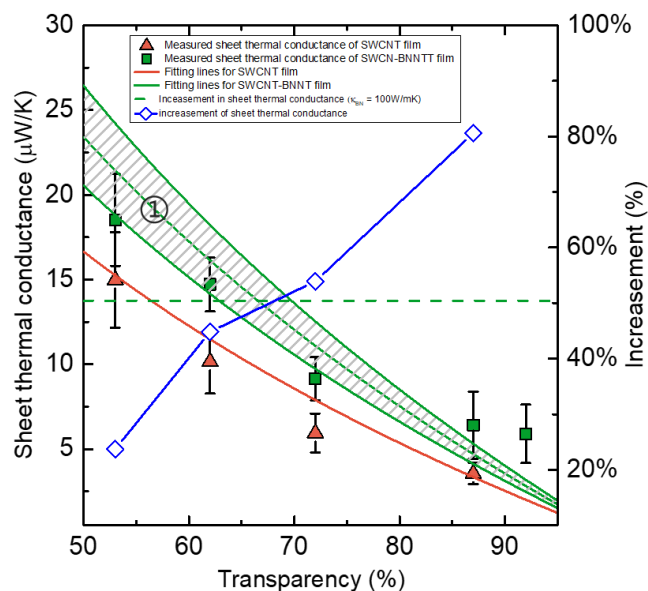


FIG 4-27. Fitting the sheet thermal conductance with experimental result and the model. The red triangle and green square represent sheet thermal conductance of annealed SWCNT film and SWCNT-BNNT film. The lines with same color are fitting lines from the model accordingly.

Similarly, if only junction parts are enhanced by additional BNNT, the sheet thermal conductance will also change. α will be the same and contact conductance will be 150% and 200 % of that in SWCNT film. The result is plotted in Figure 4-28. The green and blue lines indicate 150 % and 200 % increasement, respectively. Different from the previous discussion, increasement in contact part has limited influecne on sheet thermal conductance, as shown by the horizontal dashed lines in the figure.

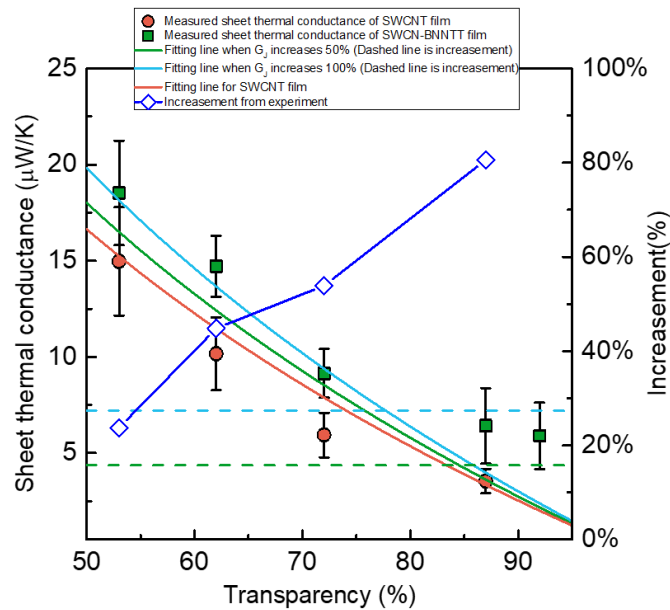


FIG 4-28. The estimation range with present model. The orange line and yellow lines represent contact conductance per area equals to 20 and 80 mW/m²K.

Based on the above discussion, the following conclusions could be drawn: (1) BNNT in this study is not perfect. If the BNNT in this study is perfect, only two layers will give a much higher sheet thermal conductance. The performance of BNNT maybe limited by the stage growth and large number of junctions in the SWCNT film. (2) Both bundle and junction could be enhanced by BNNT and give large increase in sheet thermal conductance. Even though the BNNTs are not perfect, it distributes uniformly in the film, therefore the bundles and junctions in SWCNT film both coated by BNNT and they contribute to the final sheet thermal conductance together.

4.6 CONCLUSIONS

In summary, a new 1D van der Waals heterostructure has been successfully synthesized and tested in this chapter. Five types of SWCNT films are used as template to get SWCNT-BNNT heterostructure film. These films are measured with a steady-state infrared thermography for their sheet thermal conductance. The difference between template material and heterostructure material has been clarified by discussion on Raman peak shift, electrical conductivity and Seebeck coefficient change. Besides, a concise model built based on the TEM observation of SWCNT-BNNT heterostructure film has been put forward for explaining the transport mechanism. Despite the difficulty in obtaining the thickness of measured samples, an estimation has been made on the sample thickness and thermal conductivity has been roughly evaluated.

The results indicate the sheet thermal conductance of SWCNT-BNNT heterostructure films are 18524.1140 ± 2718.7684 nW/K, 14713.5110 ± 1588.2233 nW/K, 9146.2500 ± 1265.3946 nW/K, 6410.2564 ± 1964.9838 nW/K, 5892.3395 ± 1727.4211 nW/K at room temperature synthesized on SWCNT film with transparency of 53%, 62%, 72%, 87% and 92%, respectively. Compared with annealed SWCNT film of the same transparency, the increase are 23%, 44%, 53%, 80% respectively. Because the T92 film is too thin to transfer after annealing, the enhancement of sheet thermal conductance cannot obtain. But it is reasonable to consider this increase is over 93%, which is the result by comparing the sheet thermal conductance of pure SWCNT film and SWCNT-BNNT film. The large enhancement is the result of additional BNNT serve as thermal transport channels. The difference increase degree for all the sample measured are explained from two perspectives: (a) The original sheet thermal conductance of the low-transparency SWCNT film is relatively high, the contribution from additional heat-conducting channels offered by BNNTs becomes less prominent than in the other samples. (2) Diameter of the BNNTs. For the T92 film, the density of SWCNTs is low, so bundles are formed with small diameters and are loosely packed with each other. Therefore, the diameter of BNNTs is also relatively small. However, the bundle size in the T53 film is larger than in the other samples, and the bundles are tightly packed, leading to a larger BNNT size. For 1D structures

such as CNTs, the diameter has a reverse relationship with thermal conductance; that is, the smaller the diameter is, the higher the heat transport ability.

In comparison with pure SWCNT film, electrical, mechanical and thermoelectrical properties are different for heterostructure samples. The heterostructure film shows better mechanical strength originated from BNNT and satisfying electrical conductance inherited from SWCNT. This study fills the gap in the study of 1D vdW heterostructure material up to now and may cast new light on following works in tailoring vdW heterostructure with new properties. Based on random stick network model, a quantitative model is proposed to describe the thermal transport mechanism in SWCNT film. Effective transport path and line density are defined in the model with a correction factor. The model is simplified to an average model and fit well with the experiment data. Limitation of the model has also been discussed. This model could be extended to other network materials.

CHAPTER 5 SUMMARY

The thermal conductivity of CNT assemblies with specific dimension has been investigated a lot by far. From tube diameter to length to temperature. The building block for any CNT assemble is bundle and a quantitative model is build based on experiment. In macroscale, sheet thermal conductance of SWCNT film has been model with an average model and is extended to SWCNT-BNNT heterostructure film.

To study the structural dependent thermal conductivity, micro thermometer compatible of micro meter long SWCNT bundle thermal transport study has been fabricated. Thermal conductance of these samples is tested in a large temperature range from 80 K to 330 K and the result demonstrating perfect agreement with four previous samples with different structure. Then the structure dependent property has been studied quantitatively and summarized based on kinetic theory. The thermal conductivity of bundle with increasing bundle size shows a consistent decline for all temperature measured. One step further from the previous model, phonon scattering between neighboring SWCNT is no longer linearly change with bundle size but a 4-order non-linear relationship is established. This model fits with experiment result well and gives a stable thermal conductivity when bundle size is very large. This value is believed to be the bulk thermal conductivity for macroscale SWCNT rope. To extend the model further, several important parameters are included based on previous research works. Temperature, sample length are included and thermal transport property could be estimated at different temperature. This model provides an easy and quick way to estimate the thermal property of any highly aligned SWCNT ropes with a known bundle size. This model could be extended to other bundles formed by identical tubes.

In the second part, a new 1D van der Waals heterostructure has been successfully synthesized and thermal transport property has been tested. Five types of SWCNT films are used as template to get SWCNT-BNNT heterostructure film. These films are measured with a steady-state infrared thermography for their sheet thermal conductance. The difference between template material and heterostructure material has been clarified by discussion on Raman peak shift, electrical conductivity and Seebeck coefficient change. The results indicate the sheet thermal conductance of SWCNT-BNNT heterostructure films are 18524.1140 ± 2718.7684 nW/K, 14713.5110 ± 1588.2233 nW/K, 9146.2500 ± 1265.3946 nW/K, $6410.2564 \pm$

1964.9838 nW/K, 5892.3395 ± 1727.4211 nW/K at room temperature synthesized on SWCNT film with transparency of 53%, 62%, 72%, 87% and 92%, respectively. Compared with annealed SWCNT film of the same transparency, the increase is 23%, 44%, 53%, 80% respectively. Because the T92 film is too thin to transfer after annealing, the enhancement of sheet thermal conductance cannot obtain. But it is reasonable to consider this increase is over 93%, which is the result by comparing the sheet thermal conductance of pure SWCNT film and SWCNT-BNNT film. Combine with random stick network model and the bundle model in first part, a quantitative model is proposed to describe the thermal transport mechanism in SWCNT film. Effective transport path and line density are defined in the model with a correction factor. Thermal conductance of effective is determined by statistics of the samples and the bundle model in last part. Junction thermal conductance is estimated with a defined contact area and contact conductance per area. The model is further simplified to an average model and fit well with the experiment data. Based on this model, additional BNNT function has been discussed and helps explain the experiment result. This model could be extended to estimate sheet thermal conductance of films consisted with identical tubes or heterostructure tubes with some correction.

In this thesis, two systems have been used to study the nano-scale and macroscale thermal transport mechanism in SWCNT assemblies. A nanoscale model has been established and included in the macroscale model. These models are very practical for other tube structure and cast light on the application of CNT related materials.

REFERENCE

1. Iijima, S., *Helical microtubules of graphitic carbon*. Nature, 1991. **354**(6348): p. 56-58.
2. Iijima, S. and T. Ichihashi, *Single-shell carbon nanotubes of 1-nm diameter*. Nature, 1993. **363**(6430): p. 603-605.
3. De Volder, M.F.L., et al., *Carbon Nanotubes: Present and Future Commercial Applications*. Science, 2013. **339**(6119): p. 535.
4. Cui, K., et al., *Scalable and Solid-State Redox Functionalization of Transparent Single-Walled Carbon Nanotube Films for Highly Efficient and Stable Solar Cells*. Advanced Energy Materials, 2017. **7**(18): p. 1700449.
5. Berber, S., Y.-K. Kwon, and D. Tománek, *Unusually High Thermal Conductivity of Carbon Nanotubes*. Physical Review Letters, 2000. **84**(20): p. 4613-4616.
6. Feng, Y., et al., *Quantitative study of bundle size effect on thermal conductivity of single-walled carbon nanotubes*. Applied Physics Letters, 2018. **112**(19): p. 191904.
7. Wang, Z., et al., *Length-dependent thermal conductivity of single-wall carbon nanotubes: prediction and measurements*. Nanotechnology, 2007. **18**(47): p. 475714.
8. Pettes, M.T. and L. Shi, *Thermal and Structural Characterizations of Individual Single-, Double-, and Multi-Walled Carbon Nanotubes*. Advanced Functional Materials, 2009. **19**(24): p. 3918-3925.
9. Kim, P., et al., *Thermal Transport Measurements of Individual Multiwalled Nanotubes*. Physical Review Letters, 2001. **87**(21): p. 215502.
10. Fujii, M., et al., *Measuring the Thermal Conductivity of a Single Carbon Nanotube*. Physical Review Letters, 2005. **95**(6): p. 065502.
11. Li, Q., et al., *Measuring the thermal conductivity of individual carbon nanotubes by the Raman shift method*. Nanotechnology, 2009. **20**(14): p. 145702.
12. Lin, W., et al., *Parametric study of intrinsic thermal transport in vertically aligned multi-walled carbon nanotubes using a laser flash technique*. Carbon, 2012. **50**(4): p. 1591-1603.
13. Cola, B.A., X. Xu, and T.S. Fisher, *Increased real contact in thermal interfaces: A carbon nanotube/foil material*. Applied Physics Letters, 2007. **90**(9): p. 093513.
14. Shi, L., et al., *Measuring Thermal and Thermoelectric Properties of One-Dimensional Nanostructures Using a Microfabricated Device*. Journal of Heat Transfer, 2003. **125**(5):

- p. 881-888.
15. Hsu, I.K., et al., *Direct observation of heat dissipation in individual suspended carbon nanotubes using a two-laser technique*. Journal of Applied Physics, 2011. **110**(4): p. 044328.
 16. Aliev, A.E., et al., *Thermal conductivity of multi-walled carbon nanotube sheets: radiation losses and quenching of phonon modes*. Nanotechnology, 2009. **21**(3): p. 035709.
 17. Hone, J., et al., *Electrical and thermal transport properties of magnetically aligned single wall carbon nanotube films*. Applied Physics Letters, 2000. **77**(5): p. 666-668.
 18. Fischer, J.E., et al., *Magnetically aligned single wall carbon nanotube films: Preferred orientation and anisotropic transport properties*. Journal of Applied Physics, 2003. **93**(4): p. 2157-2163.
 19. Gonnet, P., et al., *Thermal conductivity of magnetically aligned carbon nanotube buckypapers and nanocomposites*. Current Applied Physics, 2006. **6**(1): p. 119-122.
 20. Prasher, R.S., et al., *Turning Carbon Nanotubes from Exceptional Heat Conductors into Insulators*. Physical Review Letters, 2009. **102**(10): p. 105901.
 21. Sun, D.-M., et al., *A Review of Carbon Nanotube- and Graphene-Based Flexible Thin-Film Transistors*. Small, 2013. **9**(8): p. 1188-1205.
 22. Tserpes, K. and P. Papanikos, *Finite element modeling of single-walled carbon nanotubes*. Composites Part B: Engineering, 2005. **36**(5): p. 468-477.
 23. Dresselhaus, G. and S. Riichiro, *Physical properties of carbon nanotubes*. 1998: World scientific.
 24. Thomas, J.A., R.M. Iutzi, and A.J. McGaughey, *Thermal conductivity and phonon transport in empty and water-filled carbon nanotubes*. Physical Review B, 2010. **81**(4): p. 045413.
 25. Hone, J., et al., *Thermal properties of carbon nanotubes and nanotube-based materials*. Applied physics A, 2002. **74**(3): p. 339-343.
 26. Gibertini, M., et al., *Magnetic 2D materials and heterostructures*. Nature nanotechnology, 2019. **14**(5): p. 408-419.
 27. Novoselov, K., et al., *2D materials and van der Waals heterostructures*. Science, 2016. **353**(6298): p. aac9439.
 28. Jariwala, D., et al., *Emerging device applications for semiconducting two-dimensional transition metal dichalcogenides*. ACS nano, 2014. **8**(2): p. 1102-1120.

29. Liu, Y., et al., *Van der Waals heterostructures and devices*. Nature Reviews Materials, 2016. **1**(9): p. 1-17.
30. He, Q.L., et al., *Two-dimensional superconductivity at the interface of a Bi₂Te₃/FeTe heterostructure*. Nature communications, 2014. **5**(1): p. 1-8.
31. Liao, L., et al., *High- κ oxide nanoribbons as gate dielectrics for high mobility top-gated graphene transistors*. Proceedings of the national academy of sciences, 2010. **107**(15): p. 6711-6715.
32. Liu, Y., et al., *Approaching the Schottky–Mott limit in van der Waals metal–semiconductor junctions*. Nature, 2018. **557**(7707): p. 696-700.
33. Wang, C., et al., *Monolayer atomic crystal molecular superlattices*. Nature, 2018. **555**(7695): p. 231-236.
34. Liu, Y., Y. Huang, and X. Duan, *Van der Waals integration before and beyond two-dimensional materials*. Nature, 2019. **567**(7748): p. 323-333.
35. Novoselov, K.S., et al., *Electric field effect in atomically thin carbon films*. science, 2004. **306**(5696): p. 666-669.
36. Nicolosi, V., et al., *Liquid exfoliation of layered materials*. Science, 2013. **340**(6139): p. 1226419.
37. Withers, F., et al., *Light-emitting diodes by band-structure engineering in van der Waals heterostructures*. Nature materials, 2015. **14**(3): p. 301-306.
38. Xiang, R., et al., *One-dimensional van der Waals heterostructures*. Science, 2020. **367**(6477): p. 537.
39. Shen, B., et al., *Direct Chirality Recognition of Single - Crystalline and Single - Walled Transition Metal Oxide Nanotubes on Carbon Nanotube Templates*. Advanced Materials, 2018. **30**(44): p. 1803368.
40. Gong, Y., et al., *Vertical and in-plane heterostructures from WS₂/MoS₂ monolayers*. Nature materials, 2014. **13**(12): p. 1135-1142.
41. Chiu, M.-H., et al., *Spectroscopic signatures for interlayer coupling in MoS₂–WSe₂ van der Waals stacking*. ACS nano, 2014. **8**(9): p. 9649-9656.
42. Ponomarenko, L., et al., *Tunable metal–insulator transition in double-layer graphene heterostructures*. Nature Physics, 2011. **7**(12): p. 958-961.
43. Fang, H., et al., *Strong interlayer coupling in van der Waals heterostructures built from single-layer chalcogenides*. Proceedings of the National Academy of Sciences, 2014.

- 111**(17): p. 6198-6202.
44. Liu, K., et al., *Evolution of interlayer coupling in twisted molybdenum disulfide bilayers*. Nature communications, 2014. **5**(1): p. 1-6.
 45. Wang, H., et al., *Electronic and magnetic properties of the one-dimensional interfaces of two-dimensional lateral GeC/BP heterostructures*. Physical Chemistry Chemical Physics, 2019. **21**(17): p. 8856-8864.
 46. Wang, B.-J., et al., *Electronic structures and enhanced photocatalytic properties of blue phosphorene/BSe van der Waals heterostructures*. Journal of Materials Chemistry A, 2018. **6**(19): p. 8923-8929.
 47. Yankowitz, M., et al., *Emergence of superlattice Dirac points in graphene on hexagonal boron nitride*. Nature Physics, 2012. **8**(5): p. 382-386.
 48. Nayak, P.K., et al., *Probing evolution of twist-angle-dependent interlayer excitons in MoSe₂/WSe₂ van der Waals heterostructures*. Acs Nano, 2017. **11**(4): p. 4041-4050.
 49. Ceballos, F., et al., *Ultrafast charge separation and indirect exciton formation in a MoS₂-MoSe₂ van der Waals heterostructure*. ACS nano, 2014. **8**(12): p. 12717-12724.
 50. Low, J., et al., *Heterojunction photocatalysts*. Advanced materials, 2017. **29**(20): p. 1601694.
 51. Xia, W., et al., *Recent progress in van der Waals heterojunctions*. Nanoscale, 2017. **9**(13): p. 4324-4365.
 52. Jariwala, D., et al., *Near-unity absorption in van der Waals semiconductors for ultrathin optoelectronics*. Nano letters, 2016. **16**(9): p. 5482-5487.
 53. Li, C., P. Zhou, and D.W. Zhang, *Devices and applications of van der Waals heterostructures*. Journal of Semiconductors, 2017. **38**(3): p. 031005.
 54. Wang, L., et al., *One-dimensional electrical contact to a two-dimensional material*. Science, 2013. **342**(6158): p. 614-617.
 55. Lee, G.-H., et al., *Flexible and transparent MoS₂ field-effect transistors on hexagonal boron nitride-graphene heterostructures*. ACS nano, 2013. **7**(9): p. 7931-7936.
 56. Britnell, L., et al., *Field-effect tunneling transistor based on vertical graphene heterostructures*. Science, 2012. **335**(6071): p. 947-950.
 57. Yu, W.J., et al., *Highly efficient gate-tunable photocurrent generation in vertical heterostructures of layered materials*. Nature nanotechnology, 2013. **8**(12): p. 952.
 58. Zhang, W., et al., *Van der Waals stacked 2D layered materials for optoelectronics*. 2D

- Materials, 2016. **3**(2): p. 022001.
59. Wang, F., et al., *Strong electrically tunable MoTe₂/graphene van der Waals heterostructures for high-performance electronic and optoelectronic devices*. Applied Physics Letters, 2016. **109**(19): p. 193111.
 60. Jariwala, D., et al., *Gate-tunable carbon nanotube–MoS₂ heterojunction pn diode*. Proceedings of the National Academy of Sciences, 2013. **110**(45): p. 18076-18080.
 61. Li, X., et al., *Graphene on silicon Schottky junction solar cells*. Advanced materials, 2010. **22**(25): p. 2743-2748.
 62. Lopez-Sanchez, O., et al., *Light generation and harvesting in a van der Waals heterostructure*. ACS Nano, 2014. **8**(3): p. 3042-3048.
 63. Yuan, P., et al. *High Power Tolerant SWCNT-BNNT Saturable Absorber for Laser Mode-Locking*. in *2019 Conference on Lasers and Electro-Optics (CLEO)*. 2019. IEEE.
 64. Yan, Y., et al., *Van der waals heterojunctions for catalysis*. Materials Today Advances, 2020. **6**: p. 100059.
 65. Xu, H., et al., *2D heterostructure comprised of metallic 1T-MoS₂/Monolayer O_g-C₃N₄ towards efficient photocatalytic hydrogen evolution*. Applied Catalysis B: Environmental, 2018. **220**: p. 379-385.
 66. Tang, C., et al., *3D mesoporous van der Waals heterostructures for trifunctional energy electrocatalysis*. Advanced Materials, 2018. **30**(5): p. 1705110.
 67. Yan, Y., et al., *Van der Waals Heterojunction between Bottom-Up Grown Doped Graphene Quantum Dot and Graphene for Photoelectrochemical Water Splitting*. ACS nano, 2020.
 68. Zhou, T., et al., *Twinborn TiO₂–TiN heterostructures enabling smooth trapping–diffusion–conversion of polysulfides towards ultralong life lithium–sulfur batteries*. Energy & Environmental Science, 2017. **10**(7): p. 1694-1703.
 69. Li, T., et al., *Interfacial thermal resistance of 2D and 1D carbon/hexagonal boron nitride van der Waals heterostructures*. Carbon, 2016. **105**: p. 566-571.
 70. Libbrecht, K., E. Black, and C. Hirata, *A basic lock-in amplifier experiment for the undergraduate laboratory*. American Journal of Physics, 2003. **71**(11): p. 1208-1213.
 71. Pettes, M.T., *Experimental Investigations of Thermal Transport in Carbon Nanotubes, Graphene, and Nanoscale Point Contacts*. PHD dissertation.
 72. Shih, L., *Mesoscopic thermophysical measurements of microstructures and carbon*

- nanotubes*. 2001: University of California, Berkeley.
73. Osman, M.A. and D. Srivastava, *Temperature dependence of the thermal conductivity of single-wall carbon nanotubes*. Nanotechnology, 2001. **12**(1): p. 21.
74. Lukes, J.R. and H. Zhong, *Thermal Conductivity of Individual Single-Wall Carbon Nanotubes*. Journal of Heat Transfer, 2007. **129**(6): p. 705.
75. Kim, P., et al., *Thermal transport measurements of individual multiwalled nanotubes*. Physical review letters, 2001. **87**(21): p. 215502.
76. Pop, E., et al., *Thermal Conductance of an Individual Single-Wall Carbon Nanotube above Room Temperature*. Nano Letters, 2006. **6**(1): p. 96-100.
77. Inoue, T., et al., *Effect of Gas Pressure on the Density of Horizontally Aligned Single-Walled Carbon Nanotubes Grown on Quartz Substrates*. The Journal of Physical Chemistry C, 2013. **117**(22): p. 11804-11810.
78. Lindsay, L., D. Broido, and N. Mingo, *Lattice thermal conductivity of single-walled carbon nanotubes: Beyond the relaxation time approximation and phonon-phonon scattering selection rules*. Physical Review B, 2009. **80**(12): p. 125407.
79. Cao, J., et al., *Thermal conductivity of zigzag single-walled carbon nanotubes: Role of the umklapp process*. Physical Review B, 2004. **69**(7): p. 073407.
80. Hsu, I.-K., et al., *Optical absorption and thermal transport of individual suspended carbon nanotube bundles*. Nano letters, 2009. **9**(2): p. 590-594.
81. Hsu, I.-K., et al., *Optical measurement of thermal transport in suspended carbon nanotubes*. Applied Physics Letters, 2008. **92**(6): p. 63119-63119.
82. Yu, C., et al., *Thermal Conductance and Thermopower of an Individual Single-Wall Carbon Nanotube*. Nano Letters, 2005. **5**(9): p. 1842-1846.
83. Kodama, T., et al., *Modulation of thermal and thermoelectric transport in individual carbon nanotubes by fullerene encapsulation*. Nature materials, 2017.
84. Zhang, Z.M.Z.M., *Nano/microscale heat transfer*. 2007.
85. Yi, W., et al., *Linear specific heat of carbon nanotubes*. Physical Review B, 1999. **59**(14): p. R9015-R9018.
86. Zhang, Z.M., *Nano/microscale heat transfer*. 2007.
87. Novoselov, K.S., et al., *2D materials and van der Waals heterostructures*. Science, 2016. **353**(6298): p. aac9439.
88. Shen, B., et al., *Direct Chirality Recognition of Single-Crystalline and Single-Walled*

- Transition Metal Oxide Nanotubes on Carbon Nanotube Templates*. *Advanced Materials*, 2018. **30**(44): p. 1803368.
89. Liu, Y., et al., *Van der Waals heterostructures and devices*. *Nature Reviews Materials*, 2016. **1**(9): p. 16042.
90. Alexeev, E.M., et al., *Resonantly hybridized excitons in moiré superlattices in van der Waals heterostructures*. *Nature*, 2019. **567**(7746): p. 81-86.
91. Jing, L., et al., *Coaxial carbon@boron nitride nanotube arrays with enhanced thermal stability and compressive mechanical properties*. *Nanoscale*, 2016. **8**(21): p. 11114-11122.
92. Yuan, P., et al. *High Power Tolerant SWCNT-BNNT Saturable Absorber for Laser Mode-Locking*. in *Conference on Lasers and Electro-Optics*. 2019. San Jose, California: Optical Society of America.
93. Chen, C.-C., et al., *Thermoelectric transport across graphene/hexagonal boron nitride/graphene heterostructures*. *Nano Research*, 2015. **8**(2): p. 666-672.
94. Georgiou, T., et al., *Vertical field-effect transistor based on graphene-WS₂ heterostructures for flexible and transparent electronics*. *Nature Nanotechnology*, 2013. **8**(2): p. 100-103.
95. Kang, K., et al., *Layer-by-layer assembly of two-dimensional materials into wafer-scale heterostructures*. *Nature*, 2017. **550**(7675): p. 229-233.
96. Wu, C.-R., et al., *Establishment of 2D Crystal Heterostructures by Sulfurization of Sequential Transition Metal Depositions: Preparation, Characterization, and Selective Growth*. *Nano Letters*, 2016. **16**(11): p. 7093-7097.
97. Yang, W., et al., *Epitaxial growth of single-domain graphene on hexagonal boron nitride*. *Nature Materials*, 2013. **12**(9): p. 792-797.
98. Robinson, J.A., *Growing Vertical in the Flatland*. *ACS Nano*, 2016. **10**(1): p. 42-45.
99. Zhang, H., *Ultrathin Two-Dimensional Nanomaterials*. *ACS Nano*, 2015. **9**(10): p. 9451-9469.
100. Song, X., et al., *Graphene/h-BN Heterostructures: Recent Advances in Controllable Preparation and Functional Applications*. *Advanced Energy Materials*, 2016. **6**(17): p. 1600541.
101. He, T., et al., *Mechanical and thermal properties of the coaxial carbon nanotube@boron nitride nanotube composite*. *Physica E: Low-dimensional Systems and Nanostructures*, 2019. **107**: p. 182-186.
102. Tay, R.Y., et al., *Facile Synthesis of Millimeter-Scale Vertically Aligned Boron Nitride*

- Nanotube Forests by Template-Assisted Chemical Vapor Deposition*. Chemistry of Materials, 2015. **27**(20): p. 7156-7163.
103. Jing, L., et al., *Thermal Conductivity Enhancement of Coaxial Carbon@Boron Nitride Nanotube Arrays*. ACS Applied Materials & Interfaces, 2017. **9**(17): p. 14555-14560.
104. Yoshino, K., et al., *Temperature Distribution and Thermal Conductivity Measurements of Chirality-Assigned Single-Walled Carbon Nanotubes by Photoluminescence Imaging Spectroscopy*. ACS Omega, 2018. **3**(4): p. 4352-4356.
105. Qian, Y., et al., *Multifunctional Effect of p-Doping, Antireflection, and Encapsulation by Polymeric Acid for High Efficiency and Stable Carbon Nanotube-Based Silicon Solar Cells*. Advanced Energy Materials, 2020. **10**(1): p. 1902389.
106. Nasibulin, A.G., et al., *Multifunctional Free-Standing Single-Walled Carbon Nanotube Films*. ACS Nano, 2011. **5**(4): p. 3214-3221.
107. Moore, A.L. and L. Shi, *Emerging challenges and materials for thermal management of electronics*. Materials Today, 2014. **17**(4): p. 163-174.
108. Golberg, D., et al., *Boron Nitride Nanotubes*. Advanced Materials, 2007. **19**(18): p. 2413-2432.
109. Golberg, D., et al., *Boron Nitride Nanotubes and Nanosheets*. ACS Nano, 2010. **4**(6): p. 2979-2993.
110. Borowiak-Palen, E., et al., *Infrared response of multiwalled boron nitride nanotubes*. Chemical Communications, 2003(1): p. 82-83.
111. Rubio, A., J.L. Corkill, and M.L. Cohen, *Theory of graphitic boron nitride nanotubes*. Physical Review B, 1994. **49**(7): p. 5081-5084.
112. Xiang, H.J., et al., *First-principles study of small-radius single-walled BN nanotubes*. Physical Review B, 2003. **68**(3): p. 035427.
113. Aydin, M., *Vibrational and electronic properties of single-walled and double-walled boron nitride nanotubes*. Vibrational Spectroscopy, 2013. **66**: p. 30-42.
114. Feng, Y., et al., *Measurement of in-plane sheet thermal conductance of single-walled carbon nanotube thin films by steady-state infrared thermography*. Japanese Journal of Applied Physics, 2018. **57**(7): p. 075101.
115. Usamentiaga, R., et al., *Infrared Thermography for Temperature Measurement and Non-Destructive Testing*. Sensors, 2014. **14**(7).
116. Rogalski, A., *HgCdTe infrared detector material: history, status and outlook*. Reports on Progress in Physics, 2005. **68**(10): p. 2267-2336.

117. Thess, A., et al., *Crystalline Ropes of Metallic Carbon Nanotubes*. Science, 1996. **273**(5274): p. 483.
118. Hennrich, F., et al., *Preparation, characterization and applications of free-standing single walled carbon nanotube thin films*. Physical Chemistry Chemical Physics, 2002. **4**(11): p. 2273-2277.
119. Ma, W., et al., *Directly Synthesized Strong, Highly Conducting, Transparent Single-Walled Carbon Nanotube Films*. Nano Letters, 2007. **7**(8): p. 2307-2311.
120. Hu, L. and A.J.H. McGaughey, *Thermal conductance of the junction between single-walled carbon nanotubes*. Applied Physics Letters, 2014. **105**(19): p. 193104.
121. Yoshida, S., et al., *Morphology dependence of the thermal transport properties of single-walled carbon nanotube thin films*. Nanotechnology, 2017. **28**(18): p. 185701.
122. Chang, C.W., et al., *Isotope Effect on the Thermal Conductivity of Boron Nitride Nanotubes*. Physical Review Letters, 2006. **97**(8): p. 085901.
123. Zhi, C., et al., *Boron nitride nanotubes*. Materials Science and Engineering: R: Reports, 2010. **70**(3): p. 92-111.
124. Xiao, Y., et al., *Specific heat and quantized thermal conductance of single-walled boron nitride nanotubes*. Physical Review B, 2004. **69**(20): p. 205415.
125. Zhi, C., et al., *Towards Thermoconductive, Electrically Insulating Polymeric Composites with Boron Nitride Nanotubes as Fillers*. Advanced Functional Materials, 2009. **19**(12): p. 1857-1862.
126. Wang, P., R. Xiang, and S. Maruyama, *Chapter Two - Thermal Conductivity of Carbon Nanotubes and Assemblies*, in *Advances in Heat Transfer*, E.M. Sparrow, J.P. Abraham, and J.M. Gorman, Editors. 2018, Elsevier. p. 43-122.
127. Volkov, A.N. and L.V. Zhigilei, *Scaling Laws and Mesoscopic Modeling of Thermal Conductivity in Carbon Nanotube Materials*. Physical Review Letters, 2010. **104**(21): p. 215902.
128. Collins, P.G., et al., *Extreme Oxygen Sensitivity of Electronic Properties of Carbon Nanotubes*. Science, 2000. **287**(5459): p. 1801.
129. Kang, D., et al., *Oxygen-induced p-type doping of a long individual single-walled carbon nanotube*. Nanotechnology, 2005. **16**(8): p. 1048-1052.
130. Kaskela, A., et al., *Aerosol-Synthesized SWCNT Networks with Tunable Conductivity and Transparency by a Dry Transfer Technique*. Nano Letters, 2010. **10**(11): p. 4349-4355.
131. Hussain, A., et al., *Floating catalyst CVD synthesis of single walled carbon nanotubes*

- from ethylene for high performance transparent electrodes*. *Nanoscale*, 2018. **10**(20): p. 9752-9759.
132. Zhong, H. and J.R. Lukes, *Interfacial thermal resistance between carbon nanotubes: Molecular dynamics simulations and analytical thermal modeling*. *Physical Review B*, 2006. **74**(12): p. 125403.
133. Maruyama, S., et al., *Anisotropic Heat Transfer of Single-Walled Carbon Nanotubes*. *Journal of Thermal Science and Technology*, 2006. **1**(2): p. 138-148.
134. Otsuka, K., et al., *Water-assisted self-sustained burning of metallic single-walled carbon nanotubes for scalable transistor fabrication*. *Nano Research*, 2017. **10**(9): p. 3248-3260.
135. Chalopin, Y., S. Volz, and N. Mingo, *Upper bound to the thermal conductivity of carbon nanotube pellets*. *Journal of Applied Physics*, 2009. **105**(8): p. 084301.
136. Evans, W.J., M. Shen, and P. Keblinski, *Inter-tube thermal conductance in carbon nanotubes arrays and bundles: Effects of contact area and pressure*. *Applied Physics Letters*, 2012. **100**(26): p. 261908.
137. Yamaguchi, S., et al., *One-directional thermal transport in densely aligned single-wall carbon nanotube films*. *Applied Physics Letters*, 2019. **115**(22): p. 223104.
138. Yang, J., et al., *Contact thermal resistance between individual multiwall carbon nanotubes*. *Applied Physics Letters*, 2010. **96**(2): p. 023109.

LIST OF FIGURES

FIG. 1-1	Carbon nanotube related 1 D carbon materials that have been extensively studied during the recent years.....	8
FIG. 1-2	Carbon nanotubes with different chirality. (5, 5) is featured by the red line shown at end of the tube. (9, 0) is named by the zigzag structure at the tube end shown by red line. Other four chiral structures are popular carbon nanotube and being widely studied.	11
FIG. 1-3	Lattice structure of graphene. OA, OB denotes chiral vector and translational vector respectively.	12
FIG. 1-4	Unit cell and Brillouin zone of graphene in real space and in momentum space. Dotted line and shaded part denote first Brillouin zone in real space and momentum space, respectively.	14
FIG. 1-5	The calculated constant energy contours for the conduction band and valence band for 2D graphene layer. The two bands touch in the K point. Solid curves are the cutting lines for (7, 5) carbon nanotube. (Figure 2-4 (c) was originally plotted by Dr.Yuhei Miyauchi, Kyoto University)	15
FIG. 1-6	Period table of electrical conductivity for SWNT. Blue and red dots referring to semiconductor and metallic SWNT respectively.	16
FIG. 1-7	Electron density of state for (5, 5), (9, 0) and (10, 5) carbon nanotubes. (10, 0) is semiconductor behavior and (5, 5), (9, 0) are metallic behavior.	17
FIG. 1-8	(a) Phonon dispersion relations of graphene sheet, six phonon modes in the order of increasing energy are out-of-plane transverse acoustic (oTA), in-plane transverse acoustic (iTA), longitudinal acoustic (LA), out-of-plane transverse optic (oTO), in-plane transverse optic (iTO) and longitudinal optic (LO), respectively. (b) The phonon density of states of graphene sheet. (c) Calculated phonon dispersion relations of (10, 10) armchair SWNT, including 120 degrees of freedom and 66 distinct phonon branches. (d) Corresponding phonon density of states for (10,10) SWNT.	17
FIG 1-9	Illustration and structural characteristics of vdW-integrated interfaces. a, b, Schematic illustrations of 2D/2D integration (a) and vdW integration beyond 2D materials (b). Blue and red spheres represent atoms of the integrated and the host material, respectively. (adapted from	

	reference [34], Copyright 2019, with permission from Nature Publishing Group).....	21
FIG. 1-10	Assembly and characterization of 2D–2D vdWHs. (adapted from reference [29], Copyright 2016, with permission from Nature Publishing Group).	23
FIG 1-11	Overview of 1D vdW heterostructures. (adapted from reference [38], Copyright 2020, with permission from AAAS)..	23
FIG 1-12	Interlayer coupling in TMD vdWHs. Schematic illustration of a BN-separated transition metal dichalcogenide vdWH with variable interlayer coupling dependent on the number of BN layers, as shown in the coupled photoluminescence (PL) peaks in panel (adapted from reference [43], Copyright 2014, with permission from National Academy of Sciences).....	25
FIG 1-13	(a) Difference reflection spectra ($\Delta R/R$) from the monolayer and bilayers. The two resonance peaks are characteristics of direct exciton transitions in MoS ₂ . (b) Second-harmonic generation (SHG) signal from a MoS ₂ monolayer, an AA-stacked bilayer ($\theta=0^\circ$) and an AB-stacked bilayer ($\theta=60^\circ$). The traces in a, b are shifted vertically for clarification. (adapted from reference [44], Copyright 2014, with permission from Nature Publishing Group)..	26
FIG 1-14	Density of free carriers as a function of ribbon width m for the Ge ₂ GeC/BP lateral heterostructure. (adapted from reference [45], Copyright 2019, with permission from RSC).. .	26
FIG 1-15	Schematic illustration of the three different types of separation of electron–hole pairs in the case of conventional light-responsive heterojunction photocatalysts: a) type-I, b) type-II, and c) type-III heterojunctions. (adapted from reference [50], Copyright 2017, with permission from Wiley).	28
FIG. 3-1	Thermal conductivity as a function of numbers of CNT in a bundle. The measured thermal conductivity of isolated SWCNT and MWCNT are listed for comparison.	39
FIG. 3-2	Optical images of the micro thermal measurement devices. The first picture is the batch-fabricated wafer, and the second is 1-inch square chip. The following four pictures show the devices in ever higher magnifications and the components of the device are denoted in the pictures.	41
FIG. 3-3	SEM of the as synthesized HASWNT with catalyst line distanced 100 μm . Image on the right was grown for 20 min with high SWCNT density.....	42
FIG. 3-4	Peeled off with PMMA was transfer onto micro thermal measurement chips and annealed in	

vacuum to remove PMMA. 43

FIG. 3-5 Suspended SWCNT bundles and single SWCNT across the heating and sensing membrane. In the left panel, there is one SWCNT bundle indicated by a yellow arrow and a single SWCNT indicated by red arrow. In the red panel, the SWCNTs spread long on the membrane, increasing the contact area between SWCNT and membrane. 43

FIG. 3-6 (a) Photo of the sample holder. (b) Photo of the sample stage, and (c) is schematic of the cryostat. 44

FIG. 3-7 The thermal conductance of the supporting Si₃N₄ beam increases with temperature. 47

FIG. 3-8 SEM image of sample B2, with two SWCNT forming into one bundle. The gap between two thermometers is 3 μm. 50

FIG. 3-9 SEM image of sample B3, with three SWCNT forming into one bundle. The gap between two thermometers is 3 μm. 52

FIG. 3-10 SEM image of sample B4, with four SWCNT forming into one bundle. The gap between two thermometers is 3 μm. 53

FIG. 3-11 The measured thermal conductance of three SWNT samples, denoted as B2, B3 and B4, as well as the background thermal conductance. 53

FIG. 3-12 The measured thermal conductance of three SWNT samples after background deduction, denoted as B2, B3 and B4, as well as the background thermal conductance. 53

FIG. 3-13 The effective thermal conductivity of three samples versus temperature. 54

FIG. 3-14 The effective thermal conductivity of three samples versus bundle size. 55

FIG. 3-15 Fitting the experimental data with scattering rate through kinetic theory. 56

FIG. 3-16 The effective thermal conductivity of three samples versus bundle size. 57

FIG. 3-17 Fitting the experimental data with scattering rate through kinetic theory. 58

FIG. 3-18 Interaction per tube (black square) fitted by $\varphi(N)$ (red line). The inset shows small bundle size. 59

FIG. 3-19 σ at different temperature grouped by bundle size. The lines are fitting lines for $A(T)$ 60

FIG. 3-20 Colored dots in the figure are thermal conductivity plotted against bundle size at different temperature. Fitted with eq. (3-27). The dashed black lines are the bulk thermal conductivity when bundle size reaches infinite. 61

- FIG. 3-21** Thermal conductivity of thermal conductivity of isolated SWCNT as a function of temperature with a fixed length. The colored lines are the estimated thermal conductivity versus temperature with fitting parameter are calculated by the dots with same color. 62
- FIG. 4-1** UV-vis-NIR spectra of SWCNT films with different transparency at wavelength of 550 nm. The right column is the SEM images of SWCNT films of the corresponding transparency..... 72
- FIG. 4-2** Schematic of the CVD process for BNNT growth on an SWCNT template suspended on graphite window. 73
- FIG. 4-3** (a) and (b) are optical image of the BN-SWCNT heterostructure film and SWCNT film (T87) suspended over a graphite window. (c) and (d) are the optical image of the SWCNT-BNNT film and SWCNT film after rolled up and released, which confirms the spontaneous shape recovery of SWCNT-BNNT film..... 74
- FIG. 4-4** (a) SEM of the BN-SWCNT film and (b) TEM images of a bare SWCNT film. (c) TEM image of the SWCNT film after being coated with BNNTs. (d) TEM image of an isolated SWCNT coaxially coated by a three-wall BNNT. Diameter of the inner SWCNT and the outer multiwall BNNT. . 75
- FIG. 4-5** (a) FT-IR and (b) UV-vis-NIR spectra of the T87 SWCNT film before and after the BN coating was applied. These results confirm the successful growth of BNNTs. (c) Raman spectrum of the SWCNT film and BN-SWCNT film. 76
- FIG. 4-6** Schematic of the experimental setup for the thermal conductance measurement. A temperature drop is generated by the heat source and heat sink. The chamber is kept under vacuum to eliminate convection. When the heat transport along the quasi-one-dimension reached a steady-state, the IR thermal imager recorded the temperature profiles for later analyses. 77
- FIG. 4-7** (a) Absorbance of a sample film measured by FT-IR. Red dashed line is the lower limit of the IR camera. Real emissivity of the sample is out of the range of the IR camera. (b) Measured data (black square) plotted together with a fitting line (red line). Blue dashed line and star denote the temperature of the sample under investigation at emissivity measured in (a). (c) Temperature distribution of a sample along the heat transport path decided by fitting lines in (d). (d) Fitting lines of some points chosen on a sample..... 79
- FIG. 4-8** Sheet thermal conductance of bare SWCNT films (black circle) and SWCNT films after annealing (orange triangle). A decrease is observed for all four samples measured after annealing. 83

FIG. 4-9 Sheet thermal conductance (left axis) of BN-SWCNT films (mint square) and annealed SWCNT films (orange triangle). The blue hollow rhombus shows the increase ratio of the sheet thermal conductance after BN wrapping (blue hollow rhombus, right axis)..... 85

FIG. 4-10 Estimated thermal conductivity of annealed SWCNT films, SWCNT-BNNT films and the increase. 86

FIG. 4-11 The typical network structure of the SWCNT-BNNT heterostructured film. Two representative segments of the heterostructured film indicated by I and II are enlarged for better observation of the outer and inner structure. In the enlarged images, BNNTs are partially omitted for clarity of the structure of inner SWCNTs. (I) A single-layer BNNT coating on an isolated SWCNT. (II) The BNNT formed at the SWCNT junction wraps the whole junction instead of separating the upper SWCNT from the lower SWCNT bundle..... 87

FIG. 4-12 TEM of BNNT film after annealing in air for 3 hours. Raman spectra of TT53 SWCNT-BNNT film before and after annealing..... 88

FIG 4-13 (a) Raman spectra of bare SWCNT film, annealed SWCNT film, and SWCNT-BNNT film. The dashed lines show the positions of G-band. All Raman spectra were normalized by the G-band intensity. (b) Sheet resistance versus optical transparency (at 550 nm) of bare SWCNT films, annealed SWCNT films, and SWCNT-BNNT films. Solid lines shown are the approximated fitting curves. 89

FIG 4-14 Seebeck coefficient of SWCNT film, annealed SWCNT film and SWCNT-BNNT film at room temperature. 91

FIG 4-15. A schematic illustration of a SWCNT thin film showing the RSN model. Different width of the stick represents different bundle size. 92

FIG 4-16. A schematic illustration of a conducting path along which heat current can flow from B1 to B4 through B2 and B3. The contact parts between bundles are marked by C1,C2 and C3. Diameter of bundle is defined as d . Lower part of the figure is the equivalent circuit model for this path, including R_B as bundle thermal resistance and R_C as contact resistance. 93

FIG 4-17. Histogram of measured diameters of 100 bundles in T87 film. The orange line is a lognormal probability density function. The mean of lognormal distribution is 2.29 nm, therefore the mean diameter of bundle in T87 is around 9.78 nm. 94

FIG 4-18. Histogram of measured 100 crossing angle formed by bundles in T87 film. The blue line is a normal distribution. The mean of lognormal distribution is 89 degree. 95

FIG 4-19. Summary of the contact conductance from previous studies. The five lines are contact conductance per area equals to 5, 10, 20, 40, and 80 MW/ m²K. 96

FIG 4-20. Histogram of number of junction, bundle conductance and junction conductance from 1000 randomly generated paths for 100 μm sample. The average value for number of junction, thermal conductance of bundle and thermal conductance of junction are: 12, 0.5 nW/K and 1.12nW/K respectively. 97

FIG 4-21. Histogram of 1000 randomly generated paths with length of 100 μm. The average value of path conductance is 0.0115nW/K. 98

FIG 4-22. Path thermal conductance and percentage of bundle resistance plotted against length of bundle. The orange histogram is the thermal conductance per 10 μm path, and the blue triangle is the percentage of bundle resistance in the path. 99

FIG 4-23. (a) is the thermal conductance of bundle with changing bundle size and (b) is the thermal conductance with different conductance per area. In (b), the bundle diameter is also changed to 5 nm and 20 nm, denoted by hollo square and snow symbol, respectively. 100

FIG 4-24. Schematic figure of the sample, bundle i and line. The grey square with size of $l_i \cos \theta_i$ is for calculate the possible of bundle i cross the black line. 101

FIG 4-25. Sheet thermal conductance from experiment and fitting line of the model. red triangle are the experiment result and blue line is the fitting line with $\alpha=32$ 102

FIG 4-26. Fitted α with changing contact conductance per area. 103

FIG 4-27. Fitting the sheet thermal conductance with experimental result and the model. The red triangle and green square represent sheet thermal conductance of annealed SWCNT film and SWCNT-BNNT film. The lines with same color are fitting lines from the model accordingly. 104

FIG 4-28. The estimation rage with present model. The orange line and yellow lines represent contact conductance per area equals to 20 and 80 mW/m²K. 105

LIST OF TABLES

Table 1-1. Reported thermal conductivities for SWNTs, MWNTs and CNT films or mats by experiments...	10
Table 3-1. Bundle size and interaction per tube in the bundle.	59
Table 4-1. Calculated uncertainty analysis for T87 SWCNT film, SWCNT-BNNT film and annealed SWCNT film.	80

NOMENCLATURE

CNT	carbon nanotube
SWNT	single walled carbon nanotube
BNNT	boron nitride nanotube
vdW	van der Waals
TCR	temperature coefficient of resistance
RIE	reactive ion etching
DRIE	deep reactive ion etching
EBL	electron beam lithography
PL	photolithography
DOS	density of states
IR	infrared
ACCVD	alcohol catalyst chemical vapor deposition
NEG	noise equivalent thermal conductance
HASWNT	horizontally aligned single walled carbon nanotube
TEM	transmission electron microscope
TBR	thermal boundary resistance
SEM	scanning electron microscope
RT	room temperature

PUBLICATION LIST

1. Wang, P.; Xiang, R.; Maruyama, S., Thermal Conductivity of Carbon Nanotubes and Assemblies. In *Advances in Heat Transfer*; Sparrow, E. M., Abraham, J. P., Gorman, J. M., Eds.; Elsevier: New York, 2018; pp 43-122.
2. P. Wang, Y. Zheng, T. Inoue*, R. Xiang, A. Shawky, M. Watanabe, A. Anisimov, E. I. Kauppinen, S. Chiashi, S. Maruyama*, 'Enhanced In-Plane Thermal Conductance of Thin Films Composed of Coaxially Combined Single-Walled Carbon Nanotubes and Boron Nitride Nanotubes', ACS Nano, (2020).

ACKNOWLEDGEMENTS

Undertaking this PhD has been a truly life-changing experience for me and it would not have been possible to do without the support and guidance that I received from many people. Firstly, I would like to express my sincere gratitude to my supervisor, Maruyama-Sensei, who encourages me all the way to finally fulfill the doctorate degree. Your advice on both research as well as on my career have been priceless.

I am very fortunate to meet and discuss with all the previous and current members in Maruyama-Chiashi Lab. Chiashi-Sensei helps me a lot in experiments and provide useful suggestions; Xiang Rong-Sensei is the master of TEM and also gives me good suggestions on research and scientific writing; Inoue-Sensei helps me everything possible about experiments and also helped in almost everything student confront with. I also appreciate the support from Technician Watanabe-San, Secretaries Terao-san and Shimada-san.

I would like to thank our collaborators, Prof. Esko Kauppinen from Aalto University for providing SWNT thin film samples; Takeda Technical Assistant Eric Lebrasseur, who taught me about MEMS fabrication, and Takeda Technical Assistants Fujiwara-San and Okamoto-San to solve my puzzles in Takeda Clean Room.

A special thanks to my family. Words cannot express how grateful I am to my mother, father, grandfather, brother, my boyfriend Hu-san and my best friend Dai-san for all the sacrifices that they've made on my behalf. I would also like to thank all my friends Zheng-san, Lin-san, Xiao-san, Liu-san, Qin-san, and Ma-san, who have supported, and incited me to strive towards my goal.

CURRICULUM VITAE

Education Background

October 2017-present

Ph. D. candidate, Department of Mechanical Engineering, The University of Tokyo, Japan

Supervisor: Prof. Shigeo Maruyama

September 2014 – March 2017

Master of Engineering, School of Mechatronical Engineering, Beijing Institute of Technology,
China

Supervisor: Prof. Li Sui

September 2010 – July 2014

Bachelor of Engineering, School of Mechatronical Engineering, Beijing Institute of Technology,
China

Personal Information

E-mails : wangpyk@g.ecc.u-tokyo.ac.jp; wpykbeijing@163.com

Current Address: Department of Mechanical Engineering, School of Engineering, The
University of Tokyo Room 63C2, Engineering Bldg. 2, 7-3-1 Hongo, Bunkyo-ku, Tokyo 113-
8656, Japan